

UNIMORE

UNIVERSITÀ DEGLI STUDI DI
MODENA E REGGIO EMILIA

Università degli Studi di Modena e Reggio Emilia

Dipartimento di Ingegneria "Enzo Ferrari"

Master's Degree in Vehicle Engineering

Assessment of a New Dynamic RANS Approach for the Study of Parachute-Capsule Aerodynamics

---

Supervisor:
Prof. Andrea Cimarelli

Author:
Andrea Bettelli

Adjunct Supervisor:
Yves Tessier Urrecha

October 2026

A mio padre,

"And I'm floating in a most peculiar way,
and the stars look very different today"

David Bowie, Space Oddity

Contents

1 Introduction **1**

2 RANS Model **4**
2.1 Theoretical Framework 4
2.1.1 Introduction to Navier-Stokes equations 4
2.1.2 Direct Numerical Solution (DNS) 4
2.1.3 Reynolds Averaged Navier-Stokes (RANS) 6
2.1.4 Large Eddy Simulation (LES) 7
2.2 Dynamic RANS 8
2.2.1 Introduction to Dynamic RANS 8
2.2.2 Modeling of the Reynolds Stresses 9
2.2.3 Modeling of Eddy Viscosity Using the k-ε Model 9
2.2.4 Modeling of Eddy Viscosity Using the k-ω Model 10
2.3 Specific Settings 12
2.3.1 Test Filter 12
2.3.2 Clipping Procedure 12

3 Computational Framework **13**
3.1 Physical Model 13
3.2 Physical Properties 14
3.3 Mesh 15
3.4 Initial Conditions 17
3.5 Boundary Conditions 18
3.5.1 Inlet 18
3.5.2 Outlet 19
3.5.3 Atmosphere 19
3.5.4 Capsule and Canopy 20
3.6 Computational Setup 21
3.6.1 Numerical Schemes 21
3.6.1.1 Time Integration Scheme 22
3.6.1.2 Gradient Discretization Scheme 23
3.6.1.3 Divergence Discretization Scheme 24
3.6.1.4 Interpolation Scheme 25
3.6.1.5 Surface Normal Gradient Scheme 25
3.6.1.6 Laplacian Discretization Scheme 26
3.6.2 Solvers and Solution Algorithms 27
3.6.2.1 Solution Algorithm: PIMPLE 27
3.6.2.2 Relaxation Factors 29
3.6.2.3 Solvers 30

4 Results **33**
4.1 Velocity and Pressure Coefficient Distributions 33
4.1.1 Velocity 33
4.1.2 Pressure Coefficient 43
4.2 Aerodynamic Forces and Coefficients 47
4.2.1 Drag Coefficient 47
4.2.2 Transverse Coefficient 49
4.2.3 Skin Friction Coefficient 51
4.3 Canopy Aerodynamics and Frequency Spectrum Analysis 53
4.4 Turbulence Model Variables 60
4.4.1 Turbulent Kinetic Energy 60
4.4.2 Dynamic Coefficient and Eddy Viscosity 63

5 Conclusions **66**

List of Figures

2.1 Energy cascade of the turbulent spectrum [4]. 5

3.1 Illustration of the capsule and canopy assembly. 13
3.2 Illustration of the canopy components. 14
3.3 Main dimensions of the capsule and canopy assembly. 14
3.4 2D mesh before the rotational extrusion. 15
3.5 3D mesh generated by the rotational extrusion. 15
3.6 Close-up view of the x-r plane at $\theta = 0°$ highlighting the mesh structure around the capsule and canopy geometries. 16
3.7 Close-up view of the capsule and canopy boundary layer mesh before the rotational extrusion. 16
3.8 PIMPLE algorithm flowchart. 28
3.9 Progression of error modes in a one-dimensional grid [9]. 31

4.1 Instantaneous normalized velocity magnitude (u/U_∞) field around the capsule in the x-r plane at $\theta = 0°$. 34
4.2 Instantaneous normalized velocity magnitude (u/U_∞) field around the capsule visualized using LIC in the x-r plane at $\theta = 0°$. 34
4.3 Cavity, wake, and vent jet regions around the canopy, superimposed on the mean normalized velocity magnitude (U/U_∞) field. 35
4.4 Instantaneous normalized velocity magnitude (u/U_∞) field around the canopy in the x-r plane at $\theta = 0°$. 36
4.5 Instantaneous normalized velocity magnitude (u/U_∞) field around the canopy visualized using LIC in the x-r plane at $\theta = 0°$. 36
4.6 Instantaneous normalized velocity magnitude (u/U_∞) field around the canopy from the LES simulation in the x-r plane at $\theta = 0°$. 36
4.7 Locations of the selected extraction lines at $x/D = 1.20, 2.00, 2.25$, and 2.50, superimposed on the mean normalized velocity magnitude (U/U_∞) field. 37
4.8 Comparison of the mean normalized velocity fields between the dynamic RANS (left) and LES (right) models around the canopy: velocity magnitude U/U_∞ (top), axial velocity U_x/U_∞ (middle), and radial velocity U_r/U_∞ (bottom). 38
4.9 Comparison of the mean normalized axial velocity (U_x/U_∞) profiles between the dynamic RANS and the LES models along the radial coordinate r/D at $x/D = 1.20, 2.00, 2.25$, and 2.50. 39
4.10 Comparison of the mean normalized radial velocity (U_r/U_∞) profiles between the dynamic RANS and the LES models along the radial coordinate r/D at $x/D = 1.20, 2.00, 2.25$, and 2.50. 39

4.11 Comparison of the normalized root-mean-square (RMS) velocity fluctuations fields between the dynamic RANS (left) and LES (right) models around the canopy: axial component $u'_{x,\mathrm{rms}}/U_\infty$ (top), radial component $u'_{r,\mathrm{rms}}/U_\infty$ (center), and azimuthal component $u'_{\theta,\mathrm{rms}}/U_\infty$ (bottom). 41
4.12 Comparison of the normalized axial root-mean-square velocity fluctuations ($u'_{x,\mathrm{rms}}/U_\infty$) profiles between the dynamic RANS and LES models along the radial coordinate r/D at $x/D = 1.20, 2.00, 2.25$, and 2.50. 42
4.13 Comparison of the normalized radial root-mean-square velocity fluctuations ($u'_{r,\mathrm{rms}}/U_\infty$) profiles between the dynamic RANS and LES models along the radial coordinate r/D at $x/D = 1.20, 2.00, 2.25$, and 2.50. 42
4.14 Comparison of the normalized azimuthal root-mean-square velocity fluctuations ($u'_{\theta,\mathrm{rms}}/U_\infty$) profiles between the dynamic RANS and LES models along the radial coordinate r/D at $x/D = 1.20, 2.00, 2.25$, and 2.50. 43
4.15 Mean pressure coefficient (C_p) field around the capsule in the x-r plane at $\theta = 0°$. 44
4.16 Istantaneous pressure coefficient (c_p) field around the canopy in the x-r plane at $\theta = 0°$. 44
4.17 Istantaneous pressure coefficient (c_p) field around the canopy from the LES simulation in the x-r plane at $\theta = 0°$. 45
4.18 Comparison of the mean pressure coefficient (C_p) fields around the canopy between the dynamic RANS (left) and LES (right) models. 45
4.19 Comparison of the mean pressure coefficient (C_p) profiles between the dynamic RANS and the LES models along the radial coordinate r/D at $x/D = 1.20, 2.00, 2.25$, and 2.50. 46
4.20 Root-mean-square of the pressure coefficient fluctuations ($c'_{p,\mathrm{rms}}$) field around the canopy in the x-r plane at $\theta = 0°$. 46
4.21 Time history of the instantaneous drag coefficient of the canopy ($c_{D,\mathrm{canopy}}$) along with its time-averaged value ($C_{D,\mathrm{canopy}}$), computed from dynamic RANS (top) and LES (bottom) simulations. 48
4.22 Time history of the instantaneous transverse coefficient of the canopy ($c_{T,\mathrm{canopy}}$) along with its time-averaged value ($C_{T,\mathrm{canopy}}$), computed from dynamic RANS (top) and LES (bottom) simulations. 50
4.23 Mean skin friction coefficient magnitude ($|C_f|$) profile around the capsule in the x-r plane at $\theta = 0°$. 52
4.24 Three-dimensional distribution of the mean skin friction coefficient magnitude (C_f) on the canopy surface. 52
4.25 Mean normalized velocity magnitude (U/U_∞) field around the canopy visualized using LIC in the x-r plane at $\theta = 0°$. 53
4.26 Comparison of the pre-multiplied power spectral densities ($St \cdot \mathrm{PSD}$) of the canopy drag coefficient ($c_{d,\mathrm{canopy}}$) as a function of the Strouhal number (St) in log-log scale between the dynamic RANS model and the LES benchmark. 54
4.27 Comparison of the power spectral densities (PSD) of the canopy drag coefficient ($c_{d,\mathrm{canopy}}$) as a function of the Strouhal number (St) between the dynamic RANS model (top) and the LES benchmark (bottom). 56
4.28 Instantaneous vorticity magnitude ($|\boldsymbol{\omega}| \in [0, 200]\ \mathrm{s}^{-1}$) field around the canopy in the x-r plane at $\theta = 0°$, highlighting vortex detachment at the skirt. 56

4.29 Instantaneous normalized velocity magnitude (u/U_∞) field around the canopy in the x-r plane at $\theta = 0°$ across five consecutive time instances, illustrating the bubble pumping dynamics. 57
4.30 Comparison of the unwrapped θ profiles in number of revolutions versus normalized time between the dynamic RANS (top) and the LES benchmark (bottom). 59
4.31 Instantaneous vortex structures identified by Q-criterion isosurfaces ($Q = 15\ \mathrm{s}^{-2}$), colored by the instantaneous velocity magnitude field. 60
4.32 Instantaneous normalized turbulent kinetic energy (k/U_∞^2) field around the canopy in the x-r plane at $\theta = 0°$. 61
4.33 Mean normalized turbulent kinetic energy (K/U_∞^2) field around the canopy in the x-r plane at $\theta = 0°$. 61
4.34 Comparison of the mean normalized total turbulent kinetic energy ($\mathrm{TKE}_{\mathrm{tot}}/U_\infty^2$) fields around the canopy between dynamic RANS (left) and LES (right) in the x-r plane at $\theta = 0°$. 62
4.35 Comparison of the mean normalized total turbulent kinetic energy ($\mathrm{TKE}_{\mathrm{tot}}/U_\infty^2$) profiles between the dynamic RANS and the LES models along the radial coordinate r/D at $x/D = 1.20, 2.00, 2.25$, and 2.50. 63
4.36 Istantaneous dynamic coefficient (c_μ) field around the canopy in the x-r plane at $\theta = 0°$. 63
4.37 Mean dynamic coefficient (C_μ) field around the canopy in the x-r plane at $\theta = 0°$. 64
4.38 Mean eddy viscosity ($\bar{\nu}_t/\nu$) field around the canopy in the x-r plane at $\theta = 0°$. 65

List of Tables

3.1 Air properties at nominal simulation conditions. 14
3.2 Summary of mesh statistics and quality metrics. 17
3.3 Simulation initial conditions. 17
3.4 Simulation governing variables. 18
3.5 Relaxation factors for fields and equations. 29

4.1 Comparison of the canopy drag coefficient aerodynamic parameters between the dynamic RANS model and the LES benchmark. 49
4.2 Comparison of the canopy transverse force coefficient aerodynamic parameters between the dynamic RANS model and the LES benchmark. 51

Nomenclature

Symbol	Description	Unit
Latin Symbols		
c_D	Instantaneous drag coefficient	[-]
$c_{D,\max}$	Instantaneous maximum drag coefficient	[-]
$c'_{D,\mathrm{rms}}$	Root mean square of drag coefficient fluctuations	[-]
c_f	Instantaneous skin friction coefficient	[-]
c_p	Instantaneous pressure coefficient	[-]
c_T	Instantaneous transverse force coefficient	[-]
c'_T	Fluctuating transverse force coefficient	[-]
$c_{T,\max}$	Instantaneous maximum transverse force coefficient	[-]
$c'_{T,\mathrm{rms}}$	Root mean square of transverse force coefficient fluctuations	[-]
c_μ	Instantaneous dynamic coefficient	[-]
C_D	Mean drag coefficient	[-]
C_f	Mean skin friction coefficient	[-]
C_p	Mean pressure coefficient	[-]
C_T	Mean transverse force coefficient	[-]
C_μ	Mean dynamic coefficient	[-]
C_Δ	Delta coefficient	[1/m]
C_Δ^{corr}	Corrected delta coefficient	[1/m]
C_Δ^{orth}	Orthogonal delta coefficient	[1/m]
d	Diameter of the cylindrical domain	[m]
D	Nominal diameter of the canopy	[m]
D_f	Frontal diameter of the capsule	[m]
D_p	Diameter of the inflated canopy	[m]
D_v	Diameter of the canopy's vent	[m]
e_f	Approximation error at cell face f	[-]
$E_\kappa(\kappa)$	Turbulent kinetic energy density	[$\mathrm{m}^3/\mathrm{s}^2$]
f	Frequency	[Hz]
F_D	Instantaneous drag force	[N]
$\bar{F}_D$	Mean drag force	[N]
F_r	Instantaneous force in radial direction	[N]
F_θ	Instantaneous force in azimuthal direction	[N]
F_T	Instantaneous transverse force	[N]
$\bar{F}_T$	Mean transverse force	[N]
F_x	Instantaneous force in axial direction	[N]
F_y	Instantaneous force in y-direction	[N]

Symbol	Description	Unit
F_z	Instantaneous force in z-direction	[N]
g_C	Geometric weighting factor	[-]
h	Height of the cylindrical domain	[m]
I_∞	Free-stream turbulence intensity	[-]
k	Turbulent kinetic energy	[m^2/s^2]
k_∞	Free-stream turbulent kinetic energy	[m^2/s^2]
K	Mean turbulent kinetic energy	[m^2/s^2]
K_p	Peak factor	[-]
l	Distance between the capsule nose and the start of the parachute skirt	[m]
ℓ	Spatial length scale	[m]
L	Characteristic length	[m]
L_f	Length of the capsule	[m]
N	Total number of time steps	[-]
$\mathbf{n}_f$	Outward unit normal vector to cell face f	[-]
$\mathbf{n}_f^{\text{corr}}$	Corrected surface normal vector	[-]
p	Pressure of the fluid	[Pa]
p_{air}	Ambient air pressure	[Pa]
p_C	Pressure at cell center C	[Pa]
p_∞	Free-stream static pressure	[Pa]
P	Mean pressure	[Pa]
q_∞	Free-stream dynamic pressure per unit mass	[m^2/s^2]
Q^ϕ	Volumetric source term of the generic scalar equation	[units of $\phi/(m^3 \cdot s)$]
Q_C^ϕ	Volumetric source term of scalar ϕ at cell center C	[units of $\phi/(m^3 \cdot s)$]
Q_f^ϕ	Volumetric source term of scalar ϕ at cell face f	[units of $\phi/(m^3 \cdot s)$]
Re	Reynolds number	[-]
Re_D	Reynolds number based on diameter D	[-]
S	Surface area	[m^2]
$\mathbf{S}$	Surface area vector	[m^2]
S_f	Surface area of cell face f	[m^2]
$\mathbf{S}_f$	Surface area vector of cell face f	[m^2]
S_{ij}	Rate of deformation tensor	[s^{-1}]
S_{canopy}	Nominal canopy surface area normal to the flow direction	[m^2]
St	Strouhal number	[-]
t	Time	[s]
T	Coarser characteristic timescale	[s]
T_{air}	Ambient air temperature	[K]
TKE_{tot}	Mean total turbulent kinetic energy	[m^2/s^2]
u	Instantaneous velocity of the fluid	[m/s]
u'	Fluctuating velocity of the fluid	[m/s]
u_r	Instantaneous radial component of velocity	[m/s]
$u'_{r,\text{rms}}$	Root mean square of radial velocity fluctuations	[m/s]
u_x	Instantaneous axial component of velocity	[m/s]
$u'_{x,\text{rms}}$	Root mean square of axial velocity fluctuations	[m/s]
u_θ	Instantaneous azimuthal component of velocity	[m/s]
$u'_{\theta,\text{rms}}$	Root mean square of azimuthal velocity fluctuations	[m/s]

Symbol	Description	Unit
$\mathbf{u}_f$	Instantaneous velocity vector at face center f	[m/s]
U	Mean velocity of the fluid	[m/s]
U_r	Mean radial component of velocity	[m/s]
U_x	Mean axial component of velocity	[m/s]
U_θ	Mean azimuthal component of velocity	[m/s]
U_∞	Free-stream velocity	[m/s]
V_C	Volume of cell C	[m^3]
y^+	Non-dimensional wall distance	[-]

Greek Symbols

α	Under-relaxation factor	[-]
δ_{ij}	Kronecker delta	[-]
$\boldsymbol{\Delta d}$	Cell center-to-center vector	[m]
Δt	Time step	[s]
ϵ	Turbulence dissipation rate	[m^2/s^3]
η	Kolmogorov length	[m]
Γ^ϕ	Diffusion coefficient of the generic scalar equation	[kg/(m·s)]
Γ_f^ϕ	Diffusion coefficient of scalar ϕ at cell face f	[kg/(m·s)]
κ	Spatial wavenumber	[m^{-1}]
κ_L	Spatial wavenumber associated with integral scale L	[m^{-1}]
κ_{η_κ}	Spatial wavenumber associated with Kolmogorov scale η_κ	[m^{-1}]
μ_{air}	Ambient air dynamic viscosity	[kg/(m·s)]
ν	Kinematic viscosity	[m^2/s]
ν_{eff}	Effective kinematic viscosity	[m^2/s]
ν_t	Turbulent kinematic viscosity	[m^2/s]
$\bar{\nu}_t$	Mean turbulent kinematic viscosity	[m^2/s]
ν_∞	Free-stream kinematic viscosity	[m^2/s]
$\nu_{t,\infty}$	Free-stream turbulent kinematic viscosity	[m^2/s]
ω	Specific turbulence dissipation rate	[s^{-1}]
ω_∞	Free-stream specific turbulence dissipation rate	[s^{-1}]
ϕ	Transported scalar of the generic scalar equation	[depends on ϕ]
ϕ_C	Scalar value at cell center C	[units of ϕ]
ϕ_f	Scalar value at cell face f	[units of ϕ]
ψ	Blending factor	[-]
ρ	Density	[kg/m^3]
ρ_{air}	Ambient air density	[kg/m^3]
ρ_C	Fluid density at cell center C	[kg/m^3]
ρ_f	Fluid density at cell face f	[kg/m^3]
τ	Finer characteristic timescale	[s]
τ_w	Instantaneous wall shear stress	[Pa]
$\bar{\tau}_w$	Mean wall shear stress	[Pa]

Acronyms

Acronym	Full Name
DNS	Direct Numerical Simulation
EDM	Entry, Descent and Landing Demonstrator Module
ESA	European Space Agency
GAMG	Geometric-Algebraic Multigrid
LES	Large Eddy Simulation
LIC	Line Integral Convolution
OpenFOAM	Open-source Field Operation And Manipulation
PIMPLE	PISO + SIMPLE algorithm
PISO	Pressure-Implicit with Splitting of Operators
RANS	Reynolds-Averaged Navier-Stokes
RMS	Root-Mean-Square
SIMPLE	Semi-Implicit Method for Pressure-Linked Equations
URANS	Unsteady Reynolds-Averaged Navier-Stokes

Abstract

Nowadays, the aerodynamic study of bluff bodies plays a crucial role in industrial applications. These geometries are characterized by highly unsteady flow physics, dominated by vortex structures distributed across a wide range of scales, which dictate the resulting loads and overall flow behavior. A major challenge in simulating such cases lies in achieving an optimal trade-off between computational cost and solution accuracy.

This difficulty arises because conventional solvers sit at opposite extremes: traditional Reynolds-Averaged Navier-Stokes (RANS) models offer low computational cost, but they yield poor accuracy in highly unsteady regions, since the entire turbulent spectrum is modeled rather than resolved. On the other hand, Large Eddy Simulation (LES) provides high-fidelity results, but its computational cost is often unsustainable for practical applications. In this context, the dynamic RANS model represents a promising compromise by allowing turbulence resolution to adapt to the local grid size, resolving turbulent structures up to the limit imposed by the mesh.

This thesis focuses on testing how well the dynamic RANS model performs when applied to the complex aerodynamics of a parachute-capsule system. To verify its accuracy, the numerical predictions are benchmarked against a reference LES solution obtained on a much finer grid, assessing how the method behaves when mesh refinement is restricted to the critical regions of the flow. The comparison demonstrates that the dynamic RANS model delivers good agreement with the LES results despite relying on a significantly coarser grid, offering a much more efficient alternative to resolve the aerodynamics of bluff bodies in industrial applications.

Chapter 1

Introduction

Fluids can be found everywhere on Earth, ranging from large-scale phenomena, like oceanic currents and atmospheric circulation, to the smallest ones, such as the flow of lubricants in industrial ducts. Consequently, the study of fluid dynamics has always been a fundamental field of research throughout the human history, fostering the development and refinement of a wide range of technologies, from the earliest marine vessels of ancient Egypt to modern spacecraft. But the major acceleration in the physical understanding of the discipline occurred at the beginning of the twentieth century during the two World Wars, when the continuous improvement of aircraft performance became vital to gain a strategic advantage over enemy forces, which required relentless scientific and technological progress due to the increasingly demanding conditions encountered.

The main challenge of fluid dynamics has always been that flow behavior is difficult to analyze, with complexity increasing alongside the level of detail desired. In fact, fluid flows can be categorized, depending on the Reynolds number, into three distinct regimes: laminar, transitional, and turbulent. As long as the Reynolds number remains low, the flow is considered laminar and its analysis is relatively straightforward, since many variables can be neglected, making the governing equations easier to solve. However, once the Reynolds number becomes high enough, flows transition into a new regime called turbulent, that can be described as chaotic, three-dimensional, and non-linear. In this state, the simplified formulations used for laminar flow lose their validity, and it is necessary to rely on the complete and non-linear Navier-Stokes equations as the fundamental governing system. Due to this inherent non-linearity, these equations exhibit extreme sensitivity to initial conditions and consequently, even when every possible measure is taken to replicate an experiment under identical settings, the resulting instantaneous solutions vary from one test to another as if the phenomenon were not deterministic, despite being so. This intrinsic obstacle poses a major challenge in fluid dynamics analysis, as the vast majority of practical engineering applications fall within the turbulent regime and, for this reason, the attainment of reliable results is critical.

By limiting the investigation strictly to the mathematical aspects, the main problem with the non-linearity is that the Navier-Stokes equations, as far as we currently know, lack a closed-form solution. Various numerical approaches have been developed over the years to obtain physically valid results, giving rise to a constant tug-of-war between computational cost and the level of physical detail resolved, thereby yielding a broad spectrum of techniques that is discussed in more detail in Chapter 2. However, these methodologies suffer from the limitation of trying to study the phenomenon through different formulations, some statistical and others scale-resolving, without offering a single unified theory capable of bridging both worlds. In this context, the dynamic RANS model [1] was developed,

with the ambition of constructing a reconciling framework. This approach, in particular, is able to resolve fluid scales to different degrees by adjusting the grid size, with the goal of becoming, in principle, a powerful tool for industrial purposes, where maximizing the amount of information available for the design, while keeping computational costs as low as possible, remains essential.

In this work, the model has been tested on an engineering configuration of high interest: a capsule with a parachute. Such systems are particularly important in aerospace engineering for several reasons. Firstly, their relevance lies in the fact that they are bluff bodies and, as consequence, they generate large-scale vortices in their wake, providing a challenging test case to assess the predictive capabilities of the approach. Secondly, they are crucial from a practical standpoint. In particular, vented canopies have long been employed across various applications, ranging from human transport to space exploration missions. The primary objective of these devices is to decelerate a body while it is in free fall against gravitational acceleration, preventing catastrophic impacts. Due to their critical role, these systems must operate reliably under several extreme conditions, including high altitudes, supersonic speeds, and harsh atmospheric environments on other planets. Because of this, the aerodynamics of these bodies is designed in the opposite way compared to that of aircraft or automobiles: while conventional vehicles aim to generate lift or downforce and simultaneously minimize drag as an undesirable trade-off, parachutes are specifically designed to maximize drag. Furthermore, they must consistently maintain high drag levels even under challenging operational conditions, such as strong unsteady flow fields or structural membrane deformations.

A notable example of this is the 2016 ExoMars mission by the European Space Agency (ESA). The primary objective was to deliver the Schiaparelli Entry, Descent and Landing Demonstrator Module (EDM) to the surface of Mars; however, the mission failed due to an impact during the atmospheric entry. As described by [2], the root cause of the mishap involved an unpredicted interplay between the wake of the forebody capsule and the parachute's supersonic bow shock. This interaction triggered severe shock oscillations in the system, giving rise to a phenomenon commonly known as parachute "breathing", which induced large-amplitude drag fluctuations. This eventually led to a saturation of the lander's Inertial Measurement Unit (IMU), causing the navigation system to miscalculate its altitude and release the lander prematurely during the descent phase, resulting in a fatal impact.

This real-world case clearly demonstrates the critical importance of these deceleration systems, highlighting why they represent an ideal test case for evaluating the dynamic RANS model. To assess the accuracy of the simulation, the results have been benchmarked against a LES dataset, kindly provided by the University of Padua along with the model. This comparison is particularly interesting because the LES simulation was performed on a considerably more refined mesh and consequently with a higher computational cost, allowing it to resolve a broader spectrum of turbulent scales. This is especially relevant since, as previously noted, the primary goal of real engineering simulations is to maximize data accuracy while minimizing the computational cost. Consequently, this benchmark provides an ideal scenario to evaluate how closely the model represents the physics on a coarser computational grid.

In particular, the present work is divided as follows. First of all, Chapter 2 provides a brief theoretical overview of the Navier-Stokes equations and their conventional solution methods, serving as a springboard to mathematically introduce the dynamic RANS model employed in the simulation. Secondly, Chapter 3 details the computational framework, outlining the physical model, the mesh created to discretize it, the initial and boundary

conditions adopted in the simulation, and the computational setup used in OpenFOAM. Finally, in Chapter 4, the results are presented through a detailed analysis of the physical phenomena and numerical data, alongside a comparison with the LES simulation where possible.

To ensure mathematical clarity throughout the subsequent chapters, a consistent notation is adopted for all fluid dynamic variables and aerodynamic parameters. Uppercase Latin letters denote mean quantities (e.g., U, C_D), whereas lowercase Latin letters represent instantaneous values (e.g., u, c_D). Similarly, Greek symbols employ lowercase forms for instantaneous fields, while their corresponding mean quantities are identified by an overbar (e.g., $\bar{\omega}$). The only exception to this convention occurs in Chapter 4, where aerodynamic forces are expressed using uppercase Latin letters (e.g., F); here, mean values are denoted with an overbar (e.g., $\bar{F}$) to avoid ambiguity.

Chapter 2

RANS Model

2.1 Theoretical Framework

2.1.1 Introduction to Navier-Stokes equations

One of the main challenges of classical physics has always been the determination of the velocity and pressure fields of a fluid flow in a given case study. These variables, and the overall fluid behavior, are governed by the Navier-Stokes equations [3], a system of partial differential equations representing the conservation of mass and momentum. In particular, for incompressible flows, they can be written in Einstein notation as:

$$\begin{cases} \frac{\partial u_i}{\partial x_i} = 0 \\ \frac{\partial u_i}{\partial t} + \frac{\partial (u_i u_j)}{\partial x_j} = -\frac{1}{\rho}\frac{\partial p}{\partial x_i} + \nu \frac{\partial^2 u_i}{\partial x_j \partial x_j} \end{cases} \tag{2.1}$$

where the first equation is the mass conservation, while the second one is the momentum conservation, both written in the conservative form. This system is crucial because, given appropriate boundary and initial conditions, it allows the determination of the velocity and pressure fields of any fluid flow, of any size and kind. The problem is that the momentum equation is a nonlinear second-order partial differential equation that, up to this point, does not have a closed-form solution. Therefore, it cannot currently be solved analytically except in particular cases, where some terms can be neglected. Nevertheless, since obtaining a solution is fundamental to achieve fluid-dynamic predictions, several approaches have been developed over time to resolve this issue and obtain sufficiently accurate results from an engineering point of view.

Given the current state of knowledge, the primary approach used to solve the system (2.1) is through numerical techniques. Over the years, three major approaches have emerged: Direct Numerical Simulation (DNS), Reynolds-Averaged Navier-Stokes (RANS), and Large Eddy Simulation (LES).

2.1.2 Direct Numerical Solution (DNS)

DNS [3] is a high-fidelity approach that directly solves the Navier-Stokes equations by first discretizing them and then iteratively solving the resulting algebraic system. However, it is a technique that is rarely used in real-world applications, due to the fact that the computational cost is prohibitive for the typical engineering flow conditions. Its main drawback is related to how the flow changes with the Reynolds number, which is a dimensionless parameter that is defined as:

$$\mathrm{Re} = \frac{UL}{\nu} \tag{2.2}$$

where U is the characteristic flow velocity, L is the characteristic length scale, and ν is the kinematic viscosity of the fluid.

Among the features that make turbulent flows complex, there is the fact that they are characterized by a wide range of scales, as shown in Figure 2.1. The figure represents

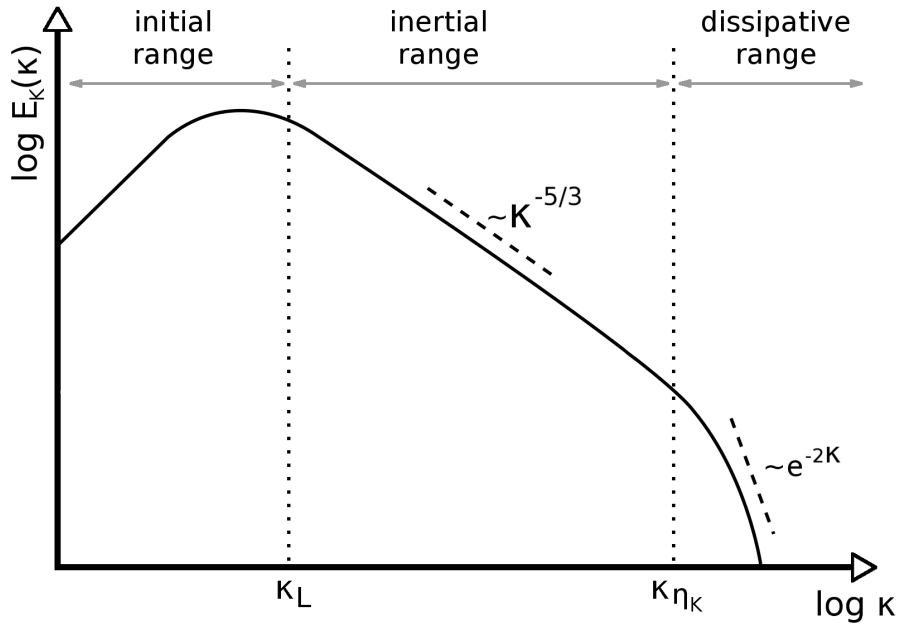


Figure 2.1: Energy cascade of the turbulent spectrum [4].

the energy cascade of the turbulent spectrum; here, the wavenumber κ is defined as $\kappa = 2\pi/\ell$, where ℓ represents the characteristic spatial length scale of the turbulent eddies. Consequently, small values of κ correspond to large, energy-containing structures, whereas large values of κ represent small-scale dissipative eddies. The energy spectrum is plotted on a log-log scale, with the wavenumber κ on the x-axis and the spectral energy density $E_\kappa(\kappa)$ on the y-axis. The largest scales are of the order of the characteristic length L, here denoted by κ_L, whereas the smallest ones are of the order of the Kolmogorov length scale η, here denoted by κ_{η_k}. As can be seen from the plot, the turbulent phenomenon is characterized by a broad spectrum of scales, ranging from the largest to the smallest. In particular, the Kolmogorov length scale η is proportional to:

$$\frac{\eta}{L} \propto Re^{-\frac{3}{4}} \tag{2.3}$$

According to the equation above, an increase of the Reynolds number results in a progressively smaller Kolmogorov scale η, thereby widening the gap with respect to the characteristic length L and consequently expanding the range of turbulent scales involved in the phenomenon. The main issue is caused by the fact that, in DNS, no turbulence modeling is employed and consequently the entire range of turbulent scales is resolved. Therefore, it is necessary to adopt a computational grid with a spacing smaller than η, thereby resolving the complete energy spectrum. As a consequence, the computational cost rapidly increases at high Reynolds, limiting the application of DNS in engineering applications.

2.1.3 Reynolds Averaged Navier-Stokes (RANS)

The idea behind RANS and LES is to reduce the computational cost by modeling the turbulent spectrum, either partially or entirely, instead of resolving it as a whole. The first approach considered here is the RANS formulation.

RANS [1,3] are an ensemble-averaged formulation of the Navier-Stokes equations. This framework is based on the key concept of Reynolds decomposition, in which the velocity field is decomposed into a mean and a fluctuating part:

$$u(\mathbf{x},t) = U(\mathbf{x}) + u'(\mathbf{x},t) \tag{2.4}$$

In particular, the RANS equations are obtained by applying the Reynolds decomposition, followed by ensemble averaging, to the Navier-Stokes equations as follows:

$$\begin{cases} \frac{\partial U_i}{\partial x_i} = 0 \\ \frac{\partial U_i}{\partial t} + \frac{\partial (U_i U_j)}{\partial x_j} = -\frac{1}{\rho}\frac{\partial P}{\partial x_i} + \nu \frac{\partial^2 U_i}{\partial x_j \partial x_j} - \frac{\partial \langle u_i' u_j' \rangle}{\partial x_j} \end{cases} \tag{2.5}$$

The main issue of the system above is the appearance of an unknown additional term, namely $\langle u_i' u_j' \rangle$, which is called the Reynolds stress tensor and can be written in explicit matrix form as:

$$\begin{bmatrix} \langle u_i' u_i' \rangle & \langle u_i' u_j' \rangle & \langle u_i' u_k' \rangle \\ \langle u_j' u_i' \rangle & \langle u_j' u_j' \rangle & \langle u_j' u_k' \rangle \\ \langle u_k' u_i' \rangle & \langle u_k' u_j' \rangle & \langle u_k' u_k' \rangle \end{bmatrix}$$

As it possible to see, $\langle u_i' u_j' \rangle$ is a symmetric second-order tensor that has six independent components and introduces six additional unknowns into the system. The appearance of this term creates a fundamental issue: the new system (2.5) is underdetermined, having 4 equations and 10 unknown variables $(4+6)$. This problem is commonly referred to as the "turbulence closure problem", and it poses a new challenge: finding a way to model the new term and make the resulting system determined. One of the most common solutions that has been developed to address this issue is the Boussinesq hypothesis, where the Reynolds stress tensor is modeled as:

$$\langle u_i' u_j' \rangle - \frac{1}{3}\langle u_k' u_k' \rangle \delta_{ij} = -2\nu_t \langle S_{ij} \rangle \tag{2.6}$$

in which ν_t is the turbulent kinematic viscosity and S_{ij} is the rate of deformation tensor, which is itself defined as:

$$S_{ij} = \frac{1}{2}\left(\frac{\partial U_i}{\partial x_j} + \frac{\partial U_j}{\partial x_i} \right) \tag{2.7}$$

The idea behind the Boussinesq hypothesis is the following. As previoulsy introduced, the main difference between the RANS equations and the Navier-Stokes equations is the presence of the Reynolds stress term. Considering that the result of RANS is a mean solution, the role of the Reynolds stress term is to smooth the field, leading to a mean flow from the unsteady physical one. As a result, the Boussinesq hypothesis assumes that turbulent motion acts as a diffusive mechanism similar to molecular viscosity and consequently models the Reynolds stresses as proportional to the rate of deformation tensor through a new physical quantity, ν_t, which still needs to be defined.

A wide variety of RANS models have been developed based directly on this principle, including the widely used k-ϵ and k-ω models, which differ in how they evaluate the turbulent kinematic viscosity. Through this closure, the system of equations becomes

mathematically solvable, yielding physically meaningful results. Nevertheless, a new fundamental issue arises: while the original RANS formulation relies on the exact ensemble average, this approach no longer solves the initial equations. Indeed, the solution obtained is not anymore the exact solution of the starting governing equations, but rather an approximation, whose accuracy heavily depends on the chosen turbulence model. As a result, RANS models no longer solve the original equations and, therefore, do not solve the exact ensemble average. This is evidenced by the fact that they are perfectly able to obtain a solution for unsteady problems with a large separation of scales when coupled with the time-derivative term, giving rise to the so-called Unsteady Reynolds-Averaged Navier-Stokes (URANS), even though the ensemble average should not be supposed to capture such unsteadiness, but rather yield a stationary solution.

In light of this, it could be concluded that such results are incorrect and consequently not suitable for accurately representing the flows. However, another way to see the discrepancy is to view the modelled equations as a new coarse-grained approach, which is different and not comparable to the one generated by the original exact RANS equations, from which it is derived. This concept will be discussed in detail later in Section 2.2.

2.1.4 Large Eddy Simulation (LES)

Another major methodology that can be used to solve fluid dynamics problems is LES [1,3]. With this approach, the strategy is different: rather than computing a mean solution that removes all the fluctuations from the velocity field, a spatial filter is applied to discard only the scales smaller than a characteristic filter scale. The symbol that is used to represent the filtering is $\langle\cdot\rangle_\delta$, which indicates that all scales smaller than δ are filtered out from the spectrum. The filtered equations take a form very similar to the one of the RANS system shown in Equation (2.5), that can be expressed as:

$$\begin{cases} \frac{\partial\langle u_i\rangle_\delta}{\partial x_i} = 0 \\ \frac{\partial\langle u_i\rangle_\delta}{\partial t} + \frac{\partial(\langle u_i\rangle_\delta\langle u_j\rangle_\delta)}{\partial x_j} = -\frac{1}{\rho}\frac{\partial\langle p\rangle_\delta}{\partial x_i} + \nu\frac{\partial^2\langle u_i\rangle_\delta}{\partial x_j\partial x_j} - \frac{\partial R_\delta(u_i,u_j)}{\partial x_j} \end{cases} \tag{2.8}$$

where $R_\delta(u_i, u_j)$ is the subgrid-scale stress tensor, which accounts for the contribution of the unresolved small-scale fluctuations to the resolved filtered field. The key concept behind LES is that the size of the smallest scales resolved depends entirely on the filter width δ; if $\delta \sim L$, nearly all the velocity fluctuations are filtered out, allowing the recovery of a RANS-like behavior. On the other hand, when $\delta \ll L$, progressively smaller scales are captured. In the limit where δ approaches the Kolmogorov scale η, all physical fluctuations are resolved and a DNS solution is recovered.

Analogously to the Reynolds stress tensor that appears in RANS, the subgrid-scale stress tensor arises in LES and requires proper modeling. However, a detailed discussion of the possible closure approaches is beyond the scope of this thesis.

Furthermore, LES can be merged with RANS, resulting in a hybrid RANS-LES formulation, where the purpose is to create a model that combines the strengths of both worlds, using RANS in the near-wall region and LES far from the wall, thus capturing large turbulent structures while reducing computational cost. However, the main problem lies in the fact that this method combines a purely statistical framework with a scale-resolving approach, without providing a unifying theoretical foundation to describe both regimes within a single formulation.

In conclusion, the overall landscape can be framed as follows: on one hand there is RANS, a formulation that in theory should be able to model the mean field but is actually

a coarse-grained approach. On the other hand, there is LES, which represent a coarse-grained approach that can be combined further with RANS to create a hybrid method, where it is difficult to link the scale-resolving nature of LES with the statistical one of RANS. The idea of dynamic RANS is to resolve this problem, or rather, to find a method that is able to reconcile all these different ways to solve the Navier-Stokes equations within the same formalism.

2.2 Dynamic RANS

2.2.1 Introduction to Dynamic RANS

As previously mentioned, the main objective of dynamic RANS [1] is to find a formalism capable of describing all the different methods discussed in the previous sections within a single framework. The heart of the approach lies in a simple concept. Classical LES formulations are obtained by applying spatial filtering to the Navier-Stokes equations, dividing the scale field into two parts: a resolved one and a modeled one. The idea of dynamic RANS is very similar, but is based on a temporal filter instead. More precisely, it models the smoothing action done by the turbulence closure with an implicit filter applied to the Navier-Stokes equations. This operator is defined as $\langle\cdot\rangle_\tau$, where τ is the temporal scale of the implicit filter. The approach therefore starts with the temporally filtered Navier-Stokes equations, that can be expressed as:

$$\begin{cases} \frac{\partial\langle u_i\rangle_\tau}{\partial x_i} = 0 \\ \frac{\partial\langle u_i\rangle_\tau}{\partial t} + \frac{\partial(\langle u_i\rangle_\tau\langle u_j\rangle_\tau)}{\partial x_j} = -\frac{1}{\rho}\frac{\partial\langle p\rangle_\tau}{\partial x_i} + \nu\frac{\partial^2\langle u_i\rangle_\tau}{\partial x_j\partial x_j} - \frac{\partial R_\tau(u_i,u_j)}{\partial x_j} \end{cases} \tag{2.9}$$

where the temporal filtering operator is assumed to commute with time differentiation, implying a time-invariant filter scale τ across the turbolence closure formulation. In addition, $R_\tau(u_i, u_j)$ is the Reynolds stress tensor, hence the physical quantity that is modeled inside RANS and hybrid RANS-LES through the turbulence closure, and can be written as:

$$R_\tau(u_i, u_j) = \langle u_i u_j\rangle_\tau \ - \langle u_i\rangle_\tau\langle u_j\rangle_\tau \tag{2.10}$$

Building on this, by adding a second filter operator with a larger characteristic time scale $T > \tau$, the turbulent stresses at a coarser level are given by:

$$R_{T_\tau}(u_i, u_j) = \langle\langle u_i u_j\rangle_\tau\rangle_T - \langle\langle u_i\rangle_\tau\rangle_T\langle\langle u_j\rangle_\tau\rangle_T \tag{2.11}$$

However, these turbulent stresses are not completely independent, and those at the coarser level can be related to the ones at the finer level by using equations (2.10) and (2.11). More specifically, $\langle u_i u_j\rangle_\tau$ can be expressed by rearranging Equation (2.10) as:

$$\langle u_i u_j\rangle_\tau = R_\tau(u_i, u_j) + \langle u_i\rangle_\tau\langle u_j\rangle_\tau \tag{2.12}$$

Substituting this expression into Equation (2.11) yields:

$$R_{T_\tau}(u_i, u_j) = \langle R_\tau(u_i, u_j)\rangle_T + \langle\langle u_i\rangle_\tau\langle u_j\rangle_\tau\rangle_T - \langle\langle u_i\rangle_\tau\rangle_T\langle\langle u_j\rangle_\tau\rangle_T \tag{2.13}$$

which, upon rearrangement, leads to the following fundamental equation:

$$R_{T_\tau}(u_i, u_j) - \langle R_\tau(u_i, u_j)\rangle_T = \langle\langle u_i\rangle_\tau\langle u_j\rangle_\tau\rangle_T - \langle\langle u_i\rangle_\tau\rangle_T\langle\langle u_j\rangle_\tau\rangle_T \tag{2.14}$$

The equation above plays a key role in the analysis, as it provides the temporal analogue to Germano's classic spatial formulation [3]:

$$R_{\Delta_\delta}(u_i, u_j) - \langle R_\delta(u_i, u_j)\rangle_\Delta = \langle\langle u_i\rangle_\delta\langle u_j\rangle_\delta\rangle_\Delta - \langle\langle u_i\rangle_\delta\rangle_\Delta\langle\langle u_j\rangle_\delta\rangle_\Delta \tag{2.15}$$

where δ is the finer spatial filter and Δ is the coarser spatial one.

2.2.2 Modeling of the Reynolds Stresses

As mentioned previously, the core of the model relies on the temporal filtering of the Navier-Stokes equations over a characteristic filter timescale τ [1]. In particular, this new physical parameter can be evaluated as follows:

$$\tau = \sqrt{\frac{\nu + \nu_\tau}{\epsilon}} \tag{2.16}$$

where ν is the kinematic viscosity of the fluid, ν_t is the eddy viscosity of the turbulence closure and ϵ is the dissipation rate of the kinetic energy. The amount of information resolved by the solution depends on the relationship between τ and the characteristic time of the large scales, tipically estimated as $\frac{L}{U}$. In the limit $\frac{\tau U}{L} \gg 1$, the implicit filter scale exceeds the characteristic flow times, smoothing out all turbulent fluctuations and recovering the statistically steady framework of standard RANS. Conversely, specifying $\frac{\tau U}{L} \ll 1$ preserves flow unsteadiness, enabling the resolution of part of the turbulent spectrum within a temporally-filtered Navier-Stokes representation. Consequently, this formulation unifies statistical and scale-resolving approaches within a single theoretical model. In this closure, the primary filtering operation at timescale τ is implicitly applied by the eddy viscosity itself, meaning that quantities within $\langle\cdot\rangle_\tau$ correspond to the resolved flow fields. Conversely, the secondary operator $\langle\cdot\rangle_T$ acts as an explicit filter over a larger timescale $T > \tau$. As a result, the behavior of the turbulence model directly depends on the relationship between these two filter scales. To evaluate the formulation in Equation (2.16), it is first necessary to model the Reynolds stresses at both resolved and test filter levels, $R_\tau(u_i, u_j)$ and $R_{T_\tau}(u_i, u_j)$. These terms are typically calculated using the Boussinesq hypothesis, previously introduced in Equation (2.6), which assumes the following form:

$$R_\tau(u_i, u_j) = -2\nu_\tau \langle S_{ij}\rangle_\tau \tag{2.17}$$

$$R_{T_\tau}(u_i, u_j) = -2\nu_{T_\tau} \langle\langle S_{ij}\rangle_\tau\rangle_T \tag{2.18}$$

where S_{ij} is the rate-of-strain tensor, defined earlier in Equation (2.7), while ν_τ and $\nu_{T\tau}$ are the eddy viscosities associated with the filter scales τ and T, respectively. This can be achieved in two ways: by using the k-ϵ model, as is discussed in Section 2.2.3, and through the k-ω model, which is detailed in Section 2.2.4.

2.2.3 Modeling of Eddy Viscosity Using the k-ε Model

One possible approach to model eddy viscosity relies on the turbulent kinetic energy and its dissipation rate [1], which is defined as follows:

$$\nu_\tau = c_\mu \frac{k_\tau^2}{\epsilon_\tau} \tag{2.19}$$

$$\nu_{T_\tau} = c_\mu \frac{k_{T_\tau}^2}{\epsilon_{T_\tau}} \tag{2.20}$$

where c_μ is a coefficient, which can be constant or dynamic, that is considered here to be the same for both filters. Furthermore, k_τ and ϵ_τ are the turbulent kinetic energy and the turbulent dissipation rate of the resolved flow solution $\langle \boldsymbol{u}\rangle_\tau$. They can be computed with

the respective transport equations as follows:

$$\begin{cases} \dfrac{\partial k_\tau}{\partial t} + \dfrac{\partial k_\tau \langle u_j \rangle_\tau}{\partial x_j} = 2\nu_\tau \langle S_{ij} \rangle_\tau \langle S_{ij} \rangle_\tau - \epsilon_\tau + \dfrac{\partial}{\partial x_j}\left[\left(\nu + \dfrac{\nu_\tau}{\sigma^k}\right)\dfrac{\partial k_\tau}{\partial x_j}\right] \\ \dfrac{\partial \epsilon_\tau}{\partial t} + \dfrac{\partial \epsilon_\tau \langle u_j \rangle_\tau}{\partial x_j} = \dfrac{\epsilon_\tau}{k_\tau}\left(2C_{\epsilon_1}\nu_\tau \langle S_{ij} \rangle_\tau \langle S_{ij} \rangle_\tau - C_{\epsilon_2}\epsilon_\tau\right) + \dfrac{\partial}{\partial x_j}\left[\left(\nu + \dfrac{\nu_\tau}{\sigma^\epsilon}\right)\dfrac{\partial \epsilon_\tau}{\partial x_j}\right] \end{cases} \tag{2.21}$$

where σ^k, σ^ϵ, C_{ϵ_1} and C_{ϵ_2} serve as model calibration parameters. Conversely, k_{T_τ} and ϵ_{T_τ} denote the turbulent kinetic energy and its dissipation rate, respectively, computed from the second-level filtered field $\langle\langle \boldsymbol{u} \rangle_\tau \rangle_T$. They can be obtained directly from k_τ and ϵ_τ with the following relation:

$$k_{T_\tau} = \langle k_\tau \rangle_T + \mathcal{L}_{ii}/2 \tag{2.22}$$

$$\epsilon_{T_\tau} = \langle \epsilon_\tau \rangle_T + \nu \mathcal{D}_{ii} \tag{2.23}$$

where L_{ij} and D_{ij} are tensors. Specifically, L_{ij} is defined from the identity Equation (2.14) as:

$$L_{ij} \equiv R_{T_\tau}(u_i, u_j) - \langle R_\tau(u_i, u_j) \rangle_T = \langle \langle u_i \rangle_\tau \langle u_j \rangle_\tau \rangle_T - \langle \langle u_i \rangle_\tau \rangle_T \langle \langle u_j \rangle_\tau \rangle_T \tag{2.24}$$

while D_{ij} is always obtained from the same equation, but by applying it to the velocity gradient instead of the velocity field:

$$\mathcal{D}_{ij} \equiv R_T\left(\frac{\partial u_i}{\partial x_j}, \frac{\partial u_i}{\partial x_j}\right) - \left\langle R_\tau\left(\frac{\partial u_i}{\partial x_j}, \frac{\partial u_i}{\partial x_j}\right)\right\rangle_T = \left\langle \frac{\partial \langle u_i \rangle_\tau}{\partial x_j}\frac{\partial \langle u_i \rangle_\tau}{\partial x_j}\right\rangle_T - \frac{\partial \langle \langle u_i \rangle_\tau \rangle_T}{\partial x_j}\frac{\partial \langle \langle u_j \rangle_\tau \rangle_T}{\partial x_j} \tag{2.25}$$

Inserting the eddy viscosity equations (2.19) and (2.20) into the Boussinesq hypothesis (2.17) and (2.18) allows identity (2.14) to be reformulated as:

$$2c_\mu \left\langle \frac{k_\tau^2}{\epsilon_\tau}\langle S_{ij} \rangle_\tau \right\rangle_T - 2c_\mu \frac{k_{T_\tau}^2}{\epsilon_{T_\tau}}\langle \langle S_{ij} \rangle_\tau \rangle_T = \langle \langle u_i \rangle_\tau \langle u_j \rangle_\tau \rangle_T - \langle \langle u_i \rangle_\tau \rangle_T \langle \langle u_j \rangle_\tau \rangle_T \tag{2.26}$$

This equation can be expressed in a more compact form by defining the tensor M_{ij} as:

$$M_{ij} = 2\left\langle \frac{k_\tau^2}{\epsilon_\tau}\langle S_{ij} \rangle_\tau \right\rangle_T - 2\frac{k_{T_\tau}^2}{\epsilon_{T_\tau}}\langle \langle S_{ij} \rangle_\tau \rangle_T \tag{2.27}$$

Using this new notation, Equation (2.26) can be simplified to:

$$c_\mu M_{ij} = L_{ij} \tag{2.28}$$

In this equation, the only unknown parameter is c_μ, which can be determined as the value that minimizes the mean-squared error of the following term:

$$c_\mu = \frac{\mathcal{M}_{ij}\mathcal{L}_{ij}}{\mathcal{M}_{ij}\mathcal{M}_{ij}} \tag{2.29}$$

2.2.4 Modeling of Eddy Viscosity Using the k-ω Model

Another way to compute the eddy viscosity, which is the approach adopted in the simulation of this work, is based on the k-ω model [5]. Compared to the k-ϵ model, which performs better in the far field, the k-ω model is more widely used in engineering applications due to its superior robustness in the near-wall region.

The k-ω formulation replaces the dissipation rate ϵ_τ with the specific dissipation rate ω_τ, defined through the relation:

$$\omega_\tau = \frac{\varepsilon_\tau}{\beta^* k_\tau} \tag{2.30}$$

where $\beta^* = 0.09$ is a constant. With this substitution, the eddy viscosity can be expressed as:

$$\nu_t = c_\mu \frac{k_\tau}{\beta^* \omega_\tau} \tag{2.31}$$

Unlike classical formulations that fix $c_\mu = \beta^* = 0.09$, this revised turbulence closure provides a mathematical basis for computing c_μ dynamically.

Now, as done for the k-ϵ model, it is possible to define the turbulent stresses at the two filter levels with this new definition of ν_t:

$$R_\tau(u_i, u_j) = -2\nu_t \langle S_{ij} \rangle_\tau = -2c_\mu \frac{k_\tau}{\beta^* \omega_\tau} \langle S_{ij} \rangle_\tau \tag{2.32}$$

$$R_{T\tau}(u_i, u_j) = -2\nu_{T\tau} \left\langle \langle S_{ij} \rangle_\tau \right\rangle_T = -2c_\mu \frac{k_{T\tau}}{\beta^* \omega_{T\tau}} \left\langle \langle S_{ij} \rangle_\tau \right\rangle_T \tag{2.33}$$

These two equations, as done in the previous section, can be substituted into identity (2.14) to obtain:

$$2c_\mu \left\langle \frac{k_\tau}{\beta^* \omega_\tau} \langle S_{ij} \rangle_\tau \right\rangle_T - 2c_\mu \frac{k_{T\tau}}{\beta^* \omega_{T\tau}} \left\langle \langle S_{ij} \rangle_\tau \right\rangle_T = \langle \langle u_i \rangle_\tau \langle u_j \rangle_\tau \rangle_T - \langle \langle u_i \rangle_\tau \rangle_T \langle \langle u_j \rangle_\tau \rangle_T \tag{2.34}$$

where the left-hand side of the equation is denoted by the tensor $\mathcal{M}_{ij}^{k-\omega}$ as follows:

$$\mathcal{M}_{ij}^{k-\omega} = 2 \left\langle \frac{k\tau}{\beta^* \omega_\tau} \langle S_{ij} \rangle_\tau \right\rangle_T - 2 \frac{k_{T_\tau}}{\beta^* \omega_{T_\tau}} \left\langle \langle S_{ij} \rangle_\tau \right\rangle_T \tag{2.35}$$

This equation is very important as it can be used to dynamically compute the coefficient c_μ. The required fields k_τ and ω_τ can be obtained by solving their corresponding transport equations:

$$\begin{cases} \dfrac{\partial k_\tau}{\partial t} + \dfrac{\partial k_\tau \langle u_j \rangle_\tau}{\partial x_j} = 2\nu_\tau \langle S_{ij} \rangle_\tau \langle S_{ij} \rangle_\tau - \beta^* k_\tau \omega_\tau + \dfrac{\partial}{\partial x_j} \left[\left(\nu + \dfrac{\nu_\tau}{\sigma^k} \right) \dfrac{\partial k_\tau}{\partial x_j} \right] \\ \dfrac{\partial \omega_\tau}{\partial t} + \dfrac{\partial \omega_\tau \langle u_j \rangle_\tau}{\partial x_j} = \dfrac{\omega_\tau}{k_\tau} \left(2\gamma\nu_\tau \langle S_{ij} \rangle_\tau \langle S_{ij} \rangle_\tau - \beta k_\tau \omega_\tau \right) + \dfrac{\partial}{\partial x_j} \left[\left(\nu + \dfrac{\nu_\tau}{\sigma^\omega} \right) \dfrac{\partial \omega_\tau}{\partial x_j} \right] \end{cases} \tag{2.36}$$

where σ^k, σ^ω, γ, and β are adjustable model coefficients. Furthermore, the turbulent quantities at the test filter level T can be obtained as:

$$k_{T_\tau} = \langle k_\tau \rangle_T + \mathcal{L}_{ii}/2 \tag{2.37}$$

$$\omega_{T_\tau} = \frac{\varepsilon_{T_\tau}}{\beta^* k_{T_\tau}} = \frac{1}{k_{T_\tau}} \left(\langle k_\tau \omega_\tau \rangle_T + \frac{\nu}{\beta^*} \mathcal{D}_{ii} \right) \tag{2.38}$$

where k_{T_τ} maintains the formulation that was already introduced in Equation (2.22) for the dynamic k-ϵ model, whereas the specific dissipation rate ω_{T_τ} is obtained from the dissipation rate ε_{T_τ}, given in Equation (2.23). Similarly to the k-ϵ model, c_μ can be computed as:

$$c_\mu = \frac{\mathcal{M}_{ij}^{k-\omega} \mathcal{L}_{ij}}{\mathcal{M}_{ij}^{k-\omega} \mathcal{M}_{ij}^{k-\omega}} \tag{2.39}$$

2.3 Specific Settings

2.3.1 Test Filter

The dynamic formulation of c_μ [1] requires the definition of a suitable kernel for the explicit test filter at the time scale T. A viable method consists in applying a backward moving average, that can be defined as:

$$\langle\phi\rangle_T(N,t) = \frac{1}{N\Delta t}\int_{t-N\Delta t}^{t}\phi(t')dt' \tag{2.40}$$

where N is the number of time steps used in the moving average, leading to $T = N\Delta t$. In this work, the test filter is chosen to span two time steps ($T = 2\Delta t$). While this choice is not mandatory, it was adopted since alternative window sizes provide quite similar results, whereas a smaller N reduces memory consumption.

2.3.2 Clipping Procedure

The mean value of c_μ tends to remain relatively low throughout the domain [5], reaching values close to the standard level ($c_{\mu,0} = 0.09$) only in active regions, such as shear layers and spatially under-resolved areas. The main numerical instabilities arise from occasional instantaneous spikes and, similarly to LES dynamic formulations, the occurrence of negative values. Taking advantage of negative values is not possible here, as it would push the numerical solution outside the stability domain of the time integration method. To ensure numerical stability, a clipping procedure is applied to constrain the dynamic coefficient within $0 \leq c_\mu \leq 0.2$. Several values were tested for the upper bound, but the results showed minimal sensitivity to this choice. Consequently, an upper limit of 0.2 was chosen so that the standard coefficient $c_{\mu,0}$ lies approximately at the center of the allowable interval.

Chapter 3

Computational Framework

3.1 Physical Model

The model simulated in this work consists of a system formed by a capsule and a parachute, kindly provided by the University of Padua for comparison purposes. As shown in Figure 3.1, the parachute is simplified to a rigid, smooth, and axisymmetric canopy without suspension lines, based on the geometry presented in [6]. Since only the canopy component is modeled, the parachute will henceforth be referred to as the canopy. The entire physical

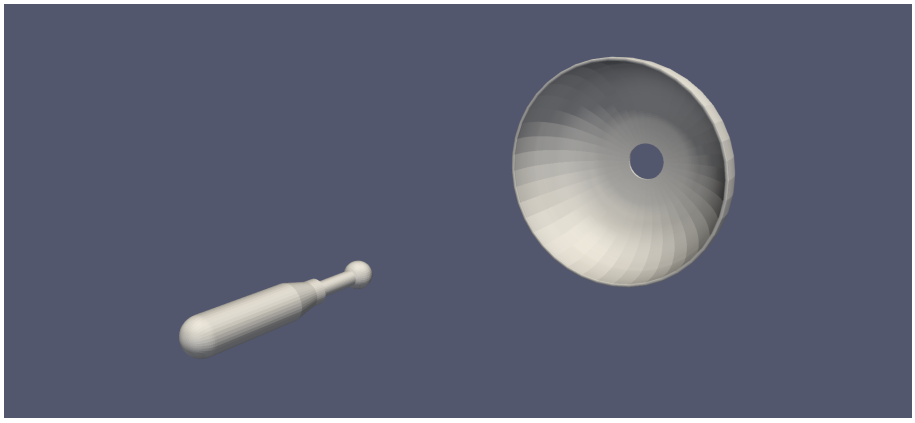


Figure 3.1: Illustration of the capsule and canopy assembly.

domain has been scaled respect to the nominal diameter of the canopy $D = 0.210$ m; this parameter is crucial in parachutes studies and represents the diameter of the fully open circular canopy, laid flat on a plane. Accordingly, from this point forward, to achieve a scale-independent representation, all spatial dimensions are expressed in terms of D.

In particular, Figure 3.2 illustrates the main components of the canopy: the skirt (the leading edge) and the vent (the rear orifice).

The geometrical dimensions of the model components are reported below:

Canopy It is a "vented hemispherical parachute" with a vent diameter of $D_v = 0.085D$. It is modeled as a rigid canopy with a fixed, unwrinkled geometry and an inflated diameter of $D_p = 0.76D$.

Capsule It is a missile-shaped capsule with a frontal diameter of $D_f = 0.067D$ and a length of $L_f = 0.40D$. The distance between the capsule nose and the leading edge of the

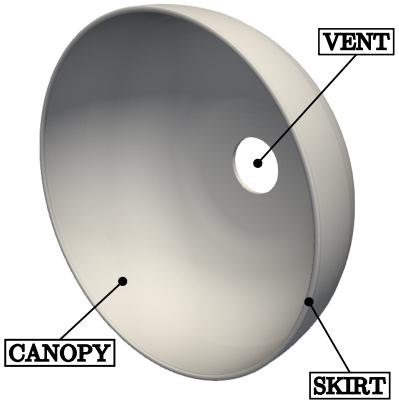


Figure 3.2: Illustration of the canopy components.

parachute skirt is $l = 1.47D$.

The main dimensions of the capsule and canopy assembly are reported in Figure 3.3.

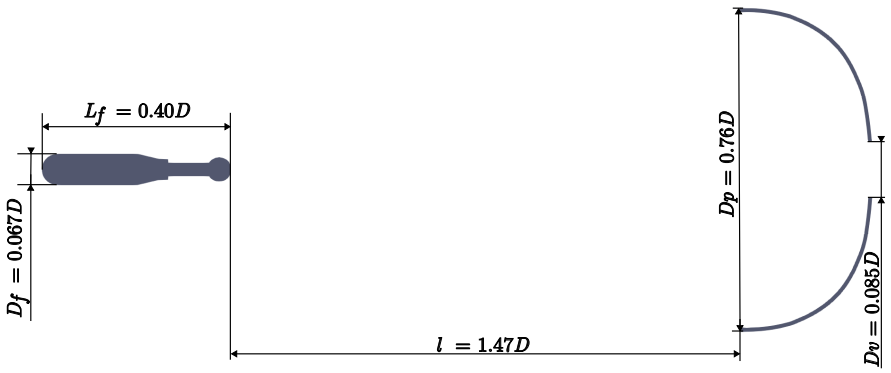


Figure 3.3: Main dimensions of the capsule and canopy assembly.

The physical domain is a cylinder with a diameter of $d = 20D$ and a height of $h = 14D$. The axes of the bodies are collinear with the cylinder axis. The reason for selecting a cylindrical domain instead of the typical prismatic one is discussed in Section 3.3. Accordingly, a cylindrical coordinate system (x, r, θ) was adopted, with its origin located at the nose of the forebody and the positive x-axis pointing downstream towards the canopy.

3.2 Physical Properties

The flow was modeled as incompressible at a Reynolds number of $Re_D = 10^5$, with nominal atmospheric air properties adopted from [6] and summarized in Table 3.1.

p_{air}	T_{air}	ρ_{air}	μ_{air}
100.3 kPa	296 K	1.191 kg/m^3	$1.850 \cdot 10^{-5}$ Pa $\cdot$ s

Table 3.1: Air properties at nominal simulation conditions.

3.3 Mesh

A critical aspect of the meshing process was ensuring high grid quality throughout the domain. Indeed, although the geometry is axisymmetric and conceptually simple, some of its features caused major difficulties in creating an optimal mesh. An initial attempt was made using the OpenFOAM's native meshing utilities to directly generate a 3D mesh from the model. However, obtaining an adequate boundary layer presented several difficulties, particularly in critical regions such as the canopy vent, yielding results that were unfit for this study. To address these issues, an alternative strategy was implemented. By taking advantage of the model's axisymmetric geometry, the domain was first discretized as a 2D grid (Figure 3.4) and then rotationally extruded around its central axis using the open-source mesh generator Gmsh [7] (Figures 3.5a and 3.5b). This choice ensures high quality

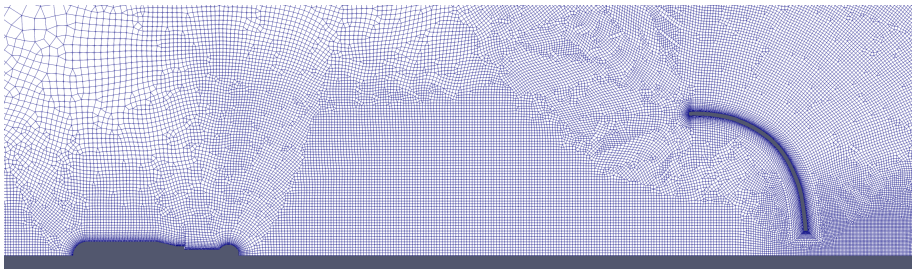


Figure 3.4: 2D mesh before the rotational extrusion.



(a) Full 3D domain

(b) Cross-section in the x-y plane at $\theta = 0°$

Figure 3.5: 3D mesh generated by the rotational extrusion.

across most of the domain, with 94.7% of the cells being hexahedra. However, the revolution of the 2D mesh introduces a central axis, which forces adjacent elements to become prisms (5.3%). Consequently, the element quality near the axis is lower, accompanied by an over-refinement in the circumferential (θ) direction towards the center.

In terms of circumferential discretization, a total of 40 divisions was chosen. Figure 3.6 presents a detailed close-up of the rx-plane at $\theta = 0$, focusing on the capsule and canopy geometries. The resulting mesh is an unstructured grid composed of 3 858 840 cells. Regarding the boundary layer region, the initial strategy was to target a value of $y^+ \gg 30$ with the aim of reducing the total cell count, considering that the primary region of interest is the wake behind the canopy and, therefore, an accurate resolution of the near-wall behavior is not fundamental. However, due to the thin geometry of both bodies, any attempt to impose a initial cell height large enough to satisfy $y^+ \gg 30$ resulted in an excessive cell skewness within the boundary layer. Consequently, a boundary layer mesh targeting $y^+ < 5$ was implemented instead. This approach allows resolving the viscous sublayer, representing the best balance between mesh quality, final cell count, and

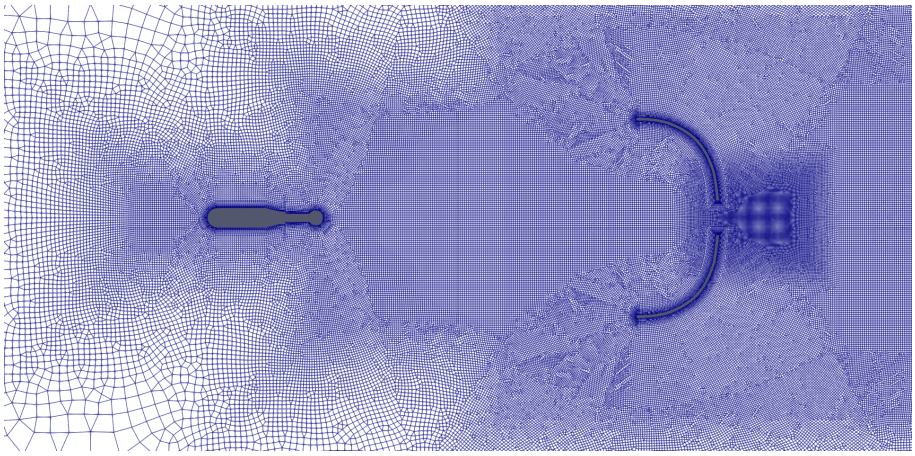
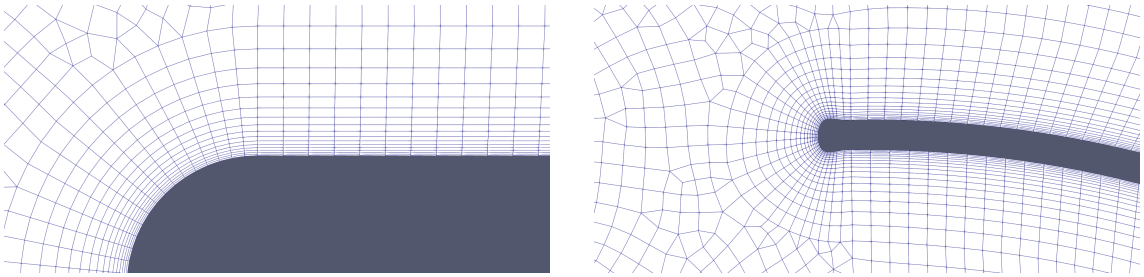


Figure 3.6: Close-up view of the x-r plane at $\theta = 0°$ highlighting the mesh structure around the capsule and canopy geometries.

accuracy of the solution. To achieve this, a total of 17 layers with a progression of 1.2 was chosen for both the capsule and the canopy. Close-up views of the boundary layers around the capsule and canopy are shown in Figure 3.7a and Figure 3.7b, respectively.



(a) Capsule boundary layer.

(b) Canopy boundary layer.

Figure 3.7: Close-up view of the capsule and canopy boundary layer mesh before the rotational extrusion.

The mesh statistics are summarized in Table 3.2. As noted previously, the grid consists almost entirely of hexahedral cells, with the exception of the prismatic elements around the central axis. The maximum non-orthogonality is 46.79°, which is well within acceptable limits, while the average non-orthogonality remains very low at 5.33°. Furthermore, the maximum skewness is 1.12, and the maximum aspect ratio reaches 33.21.

Parameter	Value
Mesh Composition	
Total Cells	3 858 840
Hexahedra (94.7%)	3 652 960
Prisms (5.3%)	205 880
Mesh Quality Metrics	
Max Aspect Ratio	33.21
Max Non-Orthogonality	46.79°
Average Non-Orthogonality	5.33°
Max Skewness	1.12

Table 3.2: Summary of mesh statistics and quality metrics.

3.4 Initial Conditions

The initial and boundary conditions were non-dimensionalized based on the Reynolds number $Re_D = 10^5$, by setting the free-stream velocity to $U_\infty = 1$ m/s, with the corresponding velocity vector $\mathbf{U}_\infty = (U_\infty, 0, 0)$, and the kinematic viscosity to $\nu_\infty = 1 \cdot 10^{-5}$ m^2/s.

In addition, since prescribing the turbulence intensity I_∞ is not mandatory in LES simulations, the benchmark study adopted $I_\infty = 0$. However, this value could not be applied in the present RANS framework due to the formulation of the initial turbulence variables. In particular, the initial turbulent kinetic energy is defined as:

$$k_\infty = \frac{3}{2}\left(U_\infty I_\infty\right)^2 \tag{3.1}$$

while the initial specific dissipation rate is given by:

$$\omega_\infty = \frac{\sqrt{k_\infty}}{c_{\mu,0}^{1/4} \cdot 0.07 \cdot D} \tag{3.2}$$

where $c_{\mu,0} = 0.09$. Using these newly defined variables, the initial kinematic turbulent viscosity $\nu_{t,\infty}$ is evaluated as:

$$\nu_{t,\infty} = \frac{k_\infty}{\omega_\infty} \tag{3.3}$$

Since ω_∞ is in the denominator and $k_\infty = \omega_\infty = 0$ when $I_\infty = 0$, a conservative value of $I_\infty = 1 \cdot 10^{-7}$ was imposed to prevent a 0/0 indeterminate form for $\nu_{t,\infty}$ and consequently avoid:

$$\nu_{t,\infty} = \frac{k_\infty}{\omega_\infty} = \frac{0}{0}$$

Based on these definitions, the set of initial conditions used in the simulation is listed in Table 3.3.

U_∞	p_∞	I_∞	k_∞	ω_∞	$\nu_{t,\infty}$
1 m/s	0 Pa	$1 \cdot 10^{-7}$ [-]	$1.5 \cdot 10^{-14}$ m^2/s^2	$3.19 \cdot 10^{-6}$ s^{-1}	$4.69 \cdot 10^{-9}$ m^2/s

Table 3.3: Simulation initial conditions.

3.5 Boundary Conditions

The cylindrical computational domain consists of three main boundaries: an inlet face oriented towards the incoming flow, a downstream outlet face and an outer lateral boundary enclosing the system, called atmosphere. Each boundary requires the specification of boundary conditions for all key physical quantities of the simulation. The governing variables for this study are summarized in Table 3.4

Symbol	Description	Unit
U	Velocity	m/s
p	Pressure	Pa
c_μ	Dynamic coefficient	–
ω	Specific dissipation rate	s^{-1}
k	Turbulent kinetic energy	m^2/s^2

Table 3.4: Simulation governing variables.

The boundary conditions assigned to each domain surface are specified as follows [8]:

3.5.1 Inlet

Velocity For velocity, a fixed-value Dirichlet boundary condition was adopted, imposing a uniform profile equal to the undisturbed free-stream flow:

$$\mathbf{U}|_{\text{inlet}} = \mathbf{U}_\infty = (U_x, U_r, U_\theta) = (U_\infty, 0, 0)$$

Pressure For pressure, a zero-gradient boundary condition was prescribed. This corresponds to a homogeneous Neumann condition, enforcing a zero normal derivative at the surface:

$$\left.\frac{\partial p}{\partial n}\right|_{\text{inlet}} = 0$$

This condition ensures a zero pressure gradient between the inlet boundary and the adjacent interior cells, allowing the pressure field to adjust naturally to the prescribed velocity.

Turbulent Kinetic Energy For the turbulent kinetic energy k, a fixed-value Dirichlet boundary condition is applied at the inlet, imposing a constant value based on the free-stream turbulence intensity and on the free-stream velocity, which can be calculated as:

$$k|_{\text{inlet}} = \frac{3}{2}(U_\infty I_\infty)^2 = k_\infty$$

Specific Dissipation Rate For the specific dissipation rate, a fixed-value Dirichlet boundary condition has been chosen, enforcing a uniform ω profile equal to the undisturbed free-stream flow value:

$$\omega|_{\text{inlet}} = \omega_\infty$$

Turbulent Kinematic Viscosity The turbulent kinematic viscosity ν_t is calculated by the dynamic RANS model using Equation (2.31), with an initial estimate derived from the standard $k-\omega$ formulation as:

$$\nu_t|_{\text{inlet}} = \frac{k|_{\text{inlet}}}{\omega|_{\text{inlet}}} = \frac{k_\infty}{\omega_\infty} = \nu_{t,\infty}$$

Dynamic Coefficient The dynamic coefficient c_μ is calculated by the dynamic RANS model using Equation (2.39), with an prescribed initial standard value of $c_\mu|_{\text{inlet}} = 0.09$.

3.5.2 Outlet

Velocity At the outlet, a boundary condition with backflow prevention (`inletOutlet`) was used to ensure numerical stability in the presence of recirculating flow from outside the domain. This formulation dynamically applies a Neumann zero-gradient condition ($\partial\mathbf{U}/\partial n = \mathbf{0}$) for exiting fluid, while switching to a fixed velocity equal to $\mathbf{U}_\infty$ if a localized backflow occurs into the domain, as shown below:

$$\begin{cases} \left.\dfrac{\partial \mathbf{U}}{\partial n}\right|_{\text{outlet}} = \mathbf{0} & \text{if } \mathbf{U}\cdot\mathbf{n} \geq 0 \quad \text{(outflow)} \\ \mathbf{U}|_{\text{outlet}} = \mathbf{U}_\infty & \text{if } \mathbf{U}\cdot\mathbf{n} < 0 \quad \text{(backflow)} \end{cases}$$

Pressure A fixed-value Dirichlet boundary condition has been used for the pressure, enforcing a uniform pressure profile matching the undisturbed free-stream flow value:

$$p|_{\text{outlet}} = p_\infty$$

Turbulent Kinetic Energy For the turbulent kinetic energy k, a boundary condition with backflow prevention (`inletOutlet`) was prescribed:

$$\begin{cases} \left.\dfrac{\partial k}{\partial n}\right|_{\text{outlet}} = 0 & \text{if } \mathbf{U}\cdot\mathbf{n} \geq 0 \quad \text{(outflow)} \\ k|_{\text{outlet}} = k_\infty & \text{if } \mathbf{U}\cdot\mathbf{n} < 0 \quad \text{(backflow)} \end{cases}$$

Specific Dissipation Rate As done for k, a boundary condition with backflow prevention (`inletOutlet`) was assigned to the specific dissipation rate ω:

$$\begin{cases} \left.\dfrac{\partial \omega}{\partial n}\right|_{\text{outlet}} = 0 & \text{if } \mathbf{U}\cdot\mathbf{n} \geq 0 \quad \text{(outflow)} \\ \omega|_{\text{outlet}} = \omega_\infty & \text{if } \mathbf{U}\cdot\mathbf{n} < 0 \quad \text{(backflow)} \end{cases}$$

Turbulent Kinematic Viscosity The turbulent kinematic viscosity ν_t is computed via the dynamic RANS model using Equation (2.31), with an initial guess defined according to the standard $k-\omega$ formulation as:

$$\nu_t|_{\text{outlet}} = \frac{k|_{\text{outlet}}}{\omega|_{\text{outlet}}} = \frac{k_\infty}{\omega_\infty} = \nu_{t,\infty}$$

Dynamic Coefficient The dynamic coefficient c_μ is obtained by the dynamic RANS model using Equation (2.39), with a chosen initial value of $c_\mu|_{\text{outlet}} = 0$.

3.5.3 Atmosphere

Velocity For the velocity, a boundary condition with backflow prevention (`freeStream`) was used to correctly model the unconfined open-air environment. Similar to `inletOutlet`,

it allows outgoing flow to leave the domain freely via a zero-gradient condition, while enforcing $\mathbf{U}_\infty$ for any incoming backflow, as expressed below:

$$\begin{cases} \left.\dfrac{\partial \mathbf{U}}{\partial n}\right|_{\text{atmosphere}} = \mathbf{0} & \text{if } \mathbf{U}\cdot\mathbf{n} \geq 0 \quad \text{(outflow)} \\ \mathbf{U}|_{\text{atmosphere}} = \mathbf{U}_\infty & \text{if } \mathbf{U}\cdot\mathbf{n} < 0 \quad \text{(backflow)} \end{cases}$$

Pressure For the pressure, a boundary condition with backflow prevention (`freeStreamPressure`) is applied, which acts as the pressure counterpart of `freeStream`, and can be written as:

$$\begin{cases} \left.\dfrac{\partial p}{\partial n}\right|_{\text{atmosphere}} = 0 & \text{if } \mathbf{U}\cdot\mathbf{n} \geq 0 \quad \text{(outflow)} \\ p|_{\text{atmosphere}} = p_\infty & \text{if } \mathbf{U}\cdot\mathbf{n} < 0 \quad \text{(backflow)} \end{cases}$$

Turbulent Kinetic Energy A boundary condition with backflow prevention (`freeStream`) is adopted for the turbulent kinetic energy:

$$\begin{cases} \left.\dfrac{\partial k}{\partial n}\right|_{\text{atmosphere}} = 0 & \text{if } \mathbf{U}\cdot\mathbf{n} \geq 0 \quad \text{(outflow)} \\ k|_{\text{atmosphere}} = k_\infty & \text{if } \mathbf{U}\cdot\mathbf{n} < 0 \quad \text{(backflow)} \end{cases}$$

Specific Dissipation Rate For the specific dissipation rate, a boundary condition with backflow prevention (`freeStream`) is employed:

$$\begin{cases} \left.\dfrac{\partial \omega}{\partial n}\right|_{\text{atmosphere}} = 0 & \text{if } \mathbf{U}\cdot\mathbf{n} \geq 0 \quad \text{(outflow)} \\ \omega|_{\text{atmosphere}} = \omega_\infty & \text{if } \mathbf{U}\cdot\mathbf{n} < 0 \quad \text{(backflow)} \end{cases}$$

Turbulent Kinematic Viscosity The turbulent kinematic viscosity ν_t is evaluated from the dynamic RANS model using Equation (2.31), with the initial value estimated according to the standard $k-\omega$ formulation as:

$$\nu_t|_{\text{atmosphere}} = \frac{k|_{\text{atmosphere}}}{\omega|_{\text{atmosphere}}} = \frac{k_\infty}{\omega_\infty} = \nu_{t,\infty}$$

Dynamic Coefficient The dynamic coefficient c_μ is calculated by the dynamic RANS model using Equation (2.39), with a standard value of $c_\mu|_{\text{atmosphere}} = 0.09$ imposed as the starting value.

3.5.4 Capsule and Canopy

Velocity For the velocity, a standard no-slip condition was used, fixing the velocity vector to zero to account for viscous fluid-surface friction at the wall interface of the canopy and the capsule. It can be expressed as:

$$\mathbf{U}|_{\text{capsule/canopy}} = (U_x, U_r, U_\theta) = (0, 0, 0)$$

Pressure For pressure, a zero-gradient Neumann boundary condition was imposed, in accordance with standard assumptions at solid boundaries:

$$\left.\frac{\partial p}{\partial n}\right|_{\text{capsule/canopy}} = 0$$

Turbulent Kinetic Energy For the turbulent kinetic energy k, a Dirichlet boundary condition with a value of zero was applied (`kLowReWallFunction`) as follows:

$$k|_{\text{capsule/canopy}} = 0$$

Specific Dissipation Rate The specific dissipation rate ω was set using a standard wall function (`omegaWallFunction`), which calculates the values from an analytical formulation to prevent ω from asymptotically approaching infinity in the near-wall region. More precisely, it is evaluated as:

$$\omega|_{\text{capsule/canopy}} = \sqrt{\omega_{\text{vis}}^2 + \omega_{\text{log}}^2}$$

where:

$$\omega_{\text{vis}} = \frac{6\,\nu}{\beta_1\, y_1^2}, \quad \omega_{\text{log}} = \frac{k^{1/2}}{c_\mu^{1/4}\,\kappa\, y_1}$$

In this expression, $\beta_1 = 0.075$, $\kappa = 0.41$, and y_1 is the distance from the wall-adjacent cell center to the boundary. For meshes with $y^+ < 5$, as in the present work, ω_{vis} dominates the boundary value, making the dependence of $\omega|_{\text{capsule/canopy}}$ on the dynamic coefficient c_μ negligible.

Turbulent Kinematic Viscosity A zero-value Dirichlet boundary condition was specified for the turbulent kinematic viscosity ν_t through the `nutLowReWallFunction` function as follows:

$$\nu_t|_{\text{capsule/canopy}} = 0$$

Dynamic Coefficient The dynamic coefficient c_μ is fixed to a value of 0 to help the stability of the simulation, as expressed by:

$$c_\mu|_{\text{capsule/canopy}} = 0$$

3.6 Computational Setup

3.6.1 Numerical Schemes

This simulation was performed using OpenFOAM, an open-source CFD software that employs the finite volume method to discretize and solve the governing equations. Consequently, before addressing further the numerical discretization schemes, it is essential to first outline the fundamental principles of the finite volume method. To achieve this, it is possible to introduce the generic scalar transport equation [8–11], which can be expressed as:

$$\underbrace{\frac{\partial(\rho\phi)}{\partial t}}_{\text{Transient term}} + \underbrace{\nabla\cdot(\rho\mathbf{u}\phi)}_{\text{Convective term}} - \underbrace{\nabla\cdot(\Gamma^\phi\nabla\phi)}_{\text{Diffusive term}} = \underbrace{Q^\phi}_{\text{Source term}} \tag{3.4}$$

where ρ is the fluid density, ϕ represents the generic scalar property being transported, $\mathbf{u}$ is the velocity vector field, Γ^ϕ is the diffusion coefficient and Q^ϕ is the volumetric source term. This equation is a simplified version of the Navier-Stokes equations, that includes the fundamental terms which are relevant for the numerical discretization; specifically, the time derivative term, the diffusion term and the convective term, are mathematically

equivalent between the two formulations. By considering a generic cell C, Equation (3.4) can be integrated over its volume as follows:

$$\int_{V_C} \frac{\partial(\rho\phi)}{\partial t}\, dV + \int_{V_C} \nabla \cdot (\rho \mathbf{u}\phi)\, dV = \int_{V_C} \nabla \cdot (\Gamma^\phi \nabla\phi)\, dV + \int_{V_C} Q^\phi\, dV \tag{3.5}$$

from which, by applying the divergence theorem, it is possible to obtain:

$$\int_{V_C} \frac{\partial(\rho\phi)}{\partial t}\, dV + \oint_{\partial V_C} (\rho \mathbf{u}\phi) \cdot d\mathbf{S} = \oint_{\partial V_C} (\Gamma^\phi \nabla\phi) \cdot d\mathbf{S} + \int_{V_C} Q^\phi\, dV \tag{3.6}$$

where $\oint_{\partial V_C}$ denotes the surface integral over the boundary ∂V_C of the volume V_C and $d\mathbf{S} = \mathbf{n}dS$ is the infinitesimal outward pointing surface area vector. From the equation above, it is possible to derive the discretized form by making the following assumptions:

- ϕ is constant in the volume of each cell and equal to the value at the cell center ϕ_C;
- ϕ is constant on each face and equal to the value at the face center ϕ_f.

Applying these assumptions leads to the discretized equation:

$$\frac{\partial(\rho_C \phi_C V_C)}{\partial t} + \sum_f (\rho_f \mathbf{u}_f \phi_f) \cdot \mathbf{S}_f - \sum_f (\Gamma_f^\phi \nabla\phi_f) \cdot \mathbf{S}_f = Q_C^\phi V_C \tag{3.7}$$

which provides the basic framework that will be used to explain the discretization schemes in the next sections.

3.6.1.1 Time Integration Scheme

The time integration scheme is necessary to discretize the transient term, here expressed as:

$$\frac{\partial(\rho_C \phi_C V_C)}{\partial t}$$

The chosen scheme is `CrankNicolson 0.7`. This method performs a blending between two classic discretization methods: Crank-Nicolson and Implicit Euler. In both models, the time derivative is discretized using the values at the time instants n and $n+1$ as:

$$\frac{\partial(\rho_C \phi_C V_C)}{\partial t} \approx \frac{(\rho_C \phi_C V_C)^{n+1} - (\rho_C \phi_C V_C)^n}{\Delta t}$$

However, despite this similarity, they differ in how they handle the spatial discretization of the remaining terms. Specifically, the Implicit Euler scheme evaluates these terms at time step $n+1$:

$$\frac{(\rho_C \phi_C V_C)^{n+1} - (\rho_C \phi_C V_C)^n}{\Delta t} = f^{n+1} \tag{3.8}$$

where f accounts for all fluxes and source terms already discretized in space. This formulation provides a first-order accurate time integration scheme with high numerical stability.

The Crank-Nicolson scheme, on the other hand, uses the same approximation for the temporal derivative, but instead of evaluating the right-hand side only at $n+1$, it takes advantage of the average between the time steps n and $n+1$ as follows:

$$\frac{(\rho_C \phi_C V_C)^{n+1} - (\rho_C \phi_C V_C)^n}{\Delta t} = \frac{f^{n+1} + f^n}{2} \tag{3.9}$$

The inclusion of the f^n contribution ensures a second-order accuracy in time, due to the fact that the temporal evolution of the variable is approximated using informations from both time levels. However, compared to Implicit Euler, Crank-Nicolson is less dissipative and more prone to numerical oscillations and potential instabilities.

To find a compromise between the dissipative nature of Implicit Euler and the higher accuracy of pure Crank-Nicolson despite its potential numerical instability, it is possible to adopt a blended approach in OpenFOAM as follows:

$$\frac{(\rho_C \phi_C V_C)^{n+1} - (\rho_C \phi_C V_C)^n}{\Delta t} = \underbrace{\psi \frac{f^{n+1} + f^n}{2}}_{\text{Crank–Nicolson}} + \underbrace{(1-\psi) f^{n+1}}_{\text{Implicit Euler}} \tag{3.10}$$

where ψ is a blending factor ranging from 0 to 1 ($0 \leq \psi \leq 1$).

A value of $\psi = 0.7$ has been chosen to maintain the high temporal accuracy of Crank-Nicolson as much as possible while increasing numerical stability, resulting in a blend of 70% Crank-Nicolson and 30% Implicit Euler.

3.6.1.2 Gradient Discretization Scheme

The discretized gradient at the cell center C, denoted as $(\nabla\phi)_C$, is evaluated differently depending on the quantity under consideration. In particular, the default discretization scheme was set to `Gauss linear`, which is based on cell-centered Green-Gauss gradient evaluation and it is defined as:

$$(\nabla\phi)_C = \frac{1}{V_C} \sum_f \phi_{f,\text{grad}} \mathbf{S}_f, \qquad \text{with } \mathbf{S}_f = S_f \mathbf{n}_f \tag{3.11}$$

where $\mathbf{S}_f$ is the surface area vector, computed as the product of the face area S_f and its outward unit normal vector $\mathbf{n}_f$, for each face bounding the cell. The "linear" part of the scheme, instead, defines how ϕ at the cell face is obtained. In particular, given a cell C and a neighboring cell F, with the respective values of ϕ at their cell centers denoted as ϕ_C and ϕ_F, the quantity on the shared face $\phi_{f,\text{grad}}$ is calculated via linear interpolation as:

$$\phi_{f,\text{grad}} = g_C \phi_C + (1 - g_C)\phi_F \qquad \text{with} \qquad g_C = \frac{\|\mathbf{r}_F - \mathbf{r}_f\|}{\|\mathbf{r}_F - \mathbf{r}_C\|} \tag{3.12}$$

where g_C is the geometric weighting factor, which is defined as the ratio between the distance from the cell center F to the cell face f and the total distance between the two cell centers. The `linear` scheme was selected to provide a second-order spatial accuracy in order to minimize the numerical diffusion across the domain.

For k and ω, the `cellLimited Gauss linear 1` scheme was used. This limiter bounds the gradient values at the cell center to ensure that the face values ϕ_f calculated with the divergence discretization schemes, discussed in Section 3.6.1.3, do not exceed the minimum and maximum values of the neighboring cells. A limiting coefficient ranging from 0 to 1 is specified right after the `linear` scheme name, where 1 applies full boundedness and 0 applies no limiting.

In this work, a coefficient value of 1 was adopted because k and ω must remain strictly positive throughout the entire simulation. Without gradient limiting, unconstrained spatial variations could introduce numerical overshoots and undershoots, leading to unphysical negative turbulence quantities and severe solver instability. Consequently, this setting was essential to guarantee numerical convergence.

For the pressure gradient $(\nabla p)_C$, on the other hand, the Least Squares Method (`leastSquares`) was chosen, which calculates the gradient at the cell center as:

$$(\nabla\phi)_{\mathrm{C}} = \sum_{\mathrm{f}} w_{\mathrm{id}}^2 \, \mathbf{G}^{-1} \cdot \mathbf{\Delta d} \, (\phi_{\mathrm{F}} - \phi_{\mathrm{C}}) \tag{3.13}$$

where $\mathbf{\Delta d}$ is the distance vector between the cell centres, given by:

$$\mathbf{\Delta d} = \mathbf{r}_F - \mathbf{r}_C \quad \text{and} \quad |\mathbf{\Delta d}| = \|\mathbf{r}_F - \mathbf{r}_C\| \tag{3.14}$$

Furthermore, w_{id} is a weighting coefficient defined as $w_{\mathrm{id}} = 1/|\mathbf{\Delta d}|$, while $\mathbf{G}$ is a tensor formulated as:

$$\mathbf{G} = \sum_{\mathrm{f}} w_{\mathrm{id}}^2 \, \mathbf{\Delta d} \otimes \mathbf{\Delta d} \tag{3.15}$$

This method, compared to the Green-Gauss gradient evaluation scheme, offers greater flexibility regarding the computation of the gradient for several reasons. First of all, the order of accuracy is not rigidly fixed to second order like the formulation above, but can theoretically be increased by retaining higher-order terms during the formulation of the method. Secondly, this approach is not restricted to using only the immediate face-neighbour cells for the stencil, allowing for a broader choice of possible points. However, this flexibility comes at the expense of an increased computational cost.

In this work, the least squares method was adopted exclusively for the pressure gradient reconstruction, because an accurate estimation of this term was particularly crucial due to its direct contribution to the momentum equation. Applying the scheme to all variables was avoided, as the additional computational increase required to evaluate the weighting factors was not justified by the negligible accuracy gain for the remaining transported quantities.

3.6.1.3 Divergence Discretization Scheme

The divergence discretization scheme is applied to determine the convective term:

$$\sum_f (\rho_f \mathbf{u}_f \phi_f) \cdot \mathbf{S}_f$$

The role of this scheme is to obtain the interpolated value of ϕ at the cell face, namely ϕ_f.

For the velocity field, a vector-specialized version of the linear upwind scheme was employed (`Gauss linearUpwindV grad(U)`), in which ϕ_f is obtained as follows:

$$\phi_f = \begin{cases} \phi_C + (\mathbf{r}_f - \mathbf{r}_C) \cdot (\nabla\phi)_C, & \text{se } \mathbf{u}_f \cdot \mathbf{S}_f \geq 0 \\ \phi_F + (\mathbf{r}_f - \mathbf{r}_F) \cdot (\nabla\phi)_F, & \text{se } \mathbf{u}_f \cdot \mathbf{S}_f < 0 \end{cases} \tag{3.16}$$

where $(\mathbf{r}_f - \mathbf{r}_C)$ and $(\mathbf{r}_f - \mathbf{r}_F)$ are the distance vectors between the cell face f and the cell centers C and F, respectively. The equation above represents a second-order, unbounded scheme that leverages the cell-centred gradient values and the $\mathbf{u}_f \cdot \mathbf{S}_f$ direction to improve upon the accuracy of the classic upwind scheme. The V-scheme version was selected because it is designed to enhance stability for vector fields.

For k and ω, a bounded version of the method has been chosen (respectively, `bounded Gauss linearUpwind grad(k)` and `bounded Gauss linearUpwind grad(omega)`) to foster the convergence of the solution.

This scheme variant addresses an issue related to the treatment of the material time derivative in the finite volume method, which for a transported scalar ϕ can be expressed as:

$$\frac{D\phi}{Dt} = \frac{\partial\phi}{\partial t} + \mathbf{U}\cdot\nabla\phi \tag{3.17}$$

Then, applying the product rule to the convective term yields:

$$\frac{D\phi}{Dt} = \frac{\partial\phi}{\partial t} + \mathbf{U}\cdot\nabla\phi = \frac{\partial\phi}{\partial t} + \nabla\cdot(\mathbf{U}\phi) - (\nabla\cdot\mathbf{U})\phi \tag{3.18}$$

Since an incompressible flow is being solved, $\nabla\cdot\mathbf{U} = 0$ should be satisfied, which would eliminate the last term. However, before reaching convergence, $\nabla\cdot\mathbf{U} \neq 0$; consequently, the last term does not vanish, making the incompressible assumption for the material derivative inaccurate during the iterative process. By contrast, in the bounded variant of the method, this term is retained to facilitate convergence. However, this does not affect the final solution, since once the solution reaches convergence, $\nabla\cdot\mathbf{U} = 0$ and the exact material derivative for incompressible flow is recovered. As a result, retaining this term enhances the numerical stability when solving the k and ω transport equations during the iterative process, without affecting the final solution in any way.

Additionally, to complete the numerical setup, a discretization scheme was specified for the deviatoric part of the divergence of the effective viscous stress tensor, written in OpenFOAM syntax as `div((nuEff*dev2(T(grad(U)))))` and mathematically as $\nabla\cdot\left[\nu_{\text{eff}}\,\text{dev}\,2\left((\nabla\mathbf{U})^T\right)\right]$. To illustrate where this term originates, it is possible to write the RANS momentum equation with a linear eddy-viscosity closure as:

$$\frac{\partial\mathbf{U}}{\partial t} + \nabla\cdot(\mathbf{U}\otimes\mathbf{U}) = -\nabla p + \nabla\cdot(\nu_{\text{eff}}\nabla\mathbf{U}) + \nabla\cdot\left[\nu_{\text{eff}}\,\text{dev}\,2\left((\nabla\mathbf{U})^T\right)\right] \tag{3.19}$$

where $\nu_{\text{eff}} = \nu + \nu_t$ is the effective kinematic viscosity, calculated as the sum of the molecular kinematic viscosity ν and the turbulent kinematic viscosity ν_t, and the last term on the right-hand side is the one addressed here.

This contribution was discretized using the `Gauss linear` scheme, to ensure second-order accuracy while minimizing discretization errors. This method evaluates the face values via linear interpolation between neighbouring cells, as previously shown in Equation (3.12).

3.6.1.4 Interpolation Scheme

The interpolation scheme specifies how values at the cell faces are evaluated from cell centers for variables that are not directly computed by other discretization schemes. In particular, it is used to interpolate the velocity at the cell faces for the calculation of the fluxes where it is required. For this purpose, the linear scheme was selected, which is described in Equation (3.12).

3.6.1.5 Surface Normal Gradient Scheme

The surface normal gradient scheme (`snGradSchemes`) is used for the discretization of the diffusive term:

$$\sum_f \Gamma^{\phi}_f (\nabla\phi)_f \cdot \mathbf{S}_f$$

Specifically, it calculates the face-normal component of the gradient at the cell face. In this work, the `corrected` scheme was chosen.

To understand the working principle of this formulation, it is first necessary to define the uncorrected orthogonal contribution to the gradient calculation, which can be expressed as:

$$(\nabla\phi)_f \cdot \mathbf{n}_f = C_\Delta(\phi_F - \phi_C) \quad \text{with} \quad C_\Delta = \frac{1}{|\mathbf{\Delta d}|} \tag{3.20}$$

This equation provides a second-order accurate formulation for the surface-normal gradient at the cell face $(\nabla\phi)_f \cdot \mathbf{n}_f$, under the assumption that the vector connecting adjacent cell centres is orthogonal to their common face. However, the main limitation of this expression is that it is mathematically valid only for fully orthogonal meshes, where the vector connecting neighbouring cell centres is perpendicular to the shared face. Since perfect orthogonality is practically impossible to achieve in realistic meshes, where some degree of non-orthogonality is always present, an alternative approach is therefore required.

To overcome this issue, a new explicit term $(\nabla\phi)_f \cdot \mathbf{n}_f^{\text{corr}}$ is introduced, which can be calculated using a modified coefficient C_Δ^{corr}. This parameter is evaluated by taking into account θ, the angle between the normal vector $\mathbf{n}_f$ and $\mathbf{\Delta d}$, that is no longer assumed to be equal to 0, leading to the expression:

$$C_\Delta^{\text{corr}} = \frac{1}{\mathbf{n}_f \cdot \mathbf{\Delta d}} = \frac{1}{|\mathbf{\Delta d}| \cos\theta} \tag{3.21}$$

Using this new parameter, the corrected version of the equation for calculating $(\nabla\phi)_f \cdot \mathbf{n}_f$ becomes:

$$(\nabla\phi)_f \cdot \mathbf{n}_f = \underbrace{C_\Delta^{\text{corr}}(\phi_F - \phi_C)}_{\text{orthogonal, implicit}} + \underbrace{\psi[(\mathbf{n}_f - C_\Delta^{\text{corr}}\mathbf{\Delta d}) \cdot (\nabla\phi)_f]}_{\text{correction, explicit}} \tag{3.22}$$

where ψ is a coefficient ($0 \leq \psi \leq 1$) that regulates the contribution of the correction term: a higher value leads to higher accuracy, but it can cause convergence problems when the non-orthogonality angle θ exceeds 75°; in such cases, ψ should be reduced accordingly.

In this work, considering that the mesh did not present non-orthogonality issues, the corrected scheme with the full correction contribution ($\psi = 1$) was adopted to achieve the highest accuracy as possible.

3.6.1.6 Laplacian Discretization Scheme

The Laplacian discretization scheme (`laplacianSchemes`) is also used for the evaluation of the diffusive flux term:

$$\sum_f \left[\Gamma_f^\phi (\nabla\phi)_f\right] \cdot \mathbf{S}_f$$

The aim of this scheme is to calculate the face value of the scalar diffusion coefficient, Γ_f^ϕ. The `Gauss linear corrected` scheme was chosen, where "Gauss" denotes the Gaussian volume integration, the "linear" part corresponds to the face interpolation introduced in Equation (3.12), while the term "corrected" corresponds to the method used to calculate $(\nabla\phi)_f \cdot \mathbf{n}_f$, which was explained in Section 3.6.1.5.

Thanks to this scheme, the total diffusive flux term inside the summation can be evaluated as:

$$\left[\Gamma_f^\phi (\nabla\phi)_f\right] \cdot \mathbf{S}_f = \Gamma_f^\phi |\mathbf{S}_f| \left[(\nabla\phi)_f \cdot \mathbf{n}_f\right]$$

3.6.2 Solvers and Solution Algorithms

3.6.2.1 Solution Algorithm: PIMPLE

In order to solve a fluid dynamics problem in OpenFOAM, it is necessary to select an appropriate solver. The PIMPLE algorithm [8–11] was chosen, to handle the unsteady behavior of the flow. This hybrid algorithm combines two other fundamental methods, SIMPLE and PISO, and is designed specifically to handle transient flows with Courant numbers (Co) greater than 1. This aspect was particularly relevant in this simulation, given that the target maximum Courant number was set to $Co_{\text{max, target}} = 1.5$.

In order to explain how the PIMPLE algorithm works, it is necessary to start from the Navier-Stokes equations, previously introduced in Equation (2.1), which can be written in vectorial notation as:

$$\begin{cases} \nabla \cdot \mathbf{u} = 0 \\ \dfrac{\partial \mathbf{u}}{\partial t} + \nabla \cdot (\mathbf{u} \otimes \mathbf{u}) - \nu \nabla^2 \mathbf{u} = -\nabla p \end{cases} \tag{3.23}$$

where, on the right-hand side, the pressure term is divided by the fluid density. This formulation is introduced to illustrate the working principle of the algorithm, but it can be extended to any equation of interest.

The incompressible momentum equation, discretized by the finite volume method, can be written in compact form as:

$$M[\mathbf{u}] = -\nabla p \tag{3.24}$$

where all the discretized terms that are multiplied by $\mathbf{u}$ are collected in the matrix M. In particular, the coefficients associated with the cell centre are placed on the diagonal of the matrix, while those associated with neighbouring cells appear in the off-diagonal entries. The next step consists of splitting $M[\mathbf{u}]$ into two parts: a diagonal part A and an off-diagonal part $\mathbf{H}$, as follows:

$$M[\mathbf{u}] = A\mathbf{u} - \mathbf{H} \tag{3.25}$$

Consequently, the discretized momentum equation can be expressed as:

$$A\mathbf{u} - \mathbf{H} = -\nabla p \tag{3.26}$$

Rearranging this expression to isolate $\mathbf{u}$ leads to the velocity correction equation:

$$\mathbf{u} = \frac{\mathbf{H}}{A} - \frac{1}{A}\nabla p \tag{3.27}$$

From this expression, the volumetric flux corrector equation is obtained by taking the scalar product between the face velocity and the surface normal vector as follows:

$$\phi = \mathbf{u}_f \cdot \mathbf{S}_f = \left(\frac{\mathbf{H}}{A}\right)_f \cdot \mathbf{S}_f - \left(\frac{1}{A}\right)_f \mathbf{S}_f \cdot (\nabla p)_f \cdot \mathbf{n}_f \tag{3.28}$$

Ultimately, by imposing $\nabla \cdot \phi = 0$, it is possible to obtain the pressure equation:

$$\nabla \cdot \left[\left(\frac{1}{A}\right)_f \nabla p\right] = \nabla \cdot \left(\frac{\mathbf{H}}{A}\right)_f \tag{3.29}$$

These equations provide the foundation for explaining the PIMPLE algorithm. A flowchart illustrating the procedure is presented in Fig. 3.8. The algorithm is based on two main

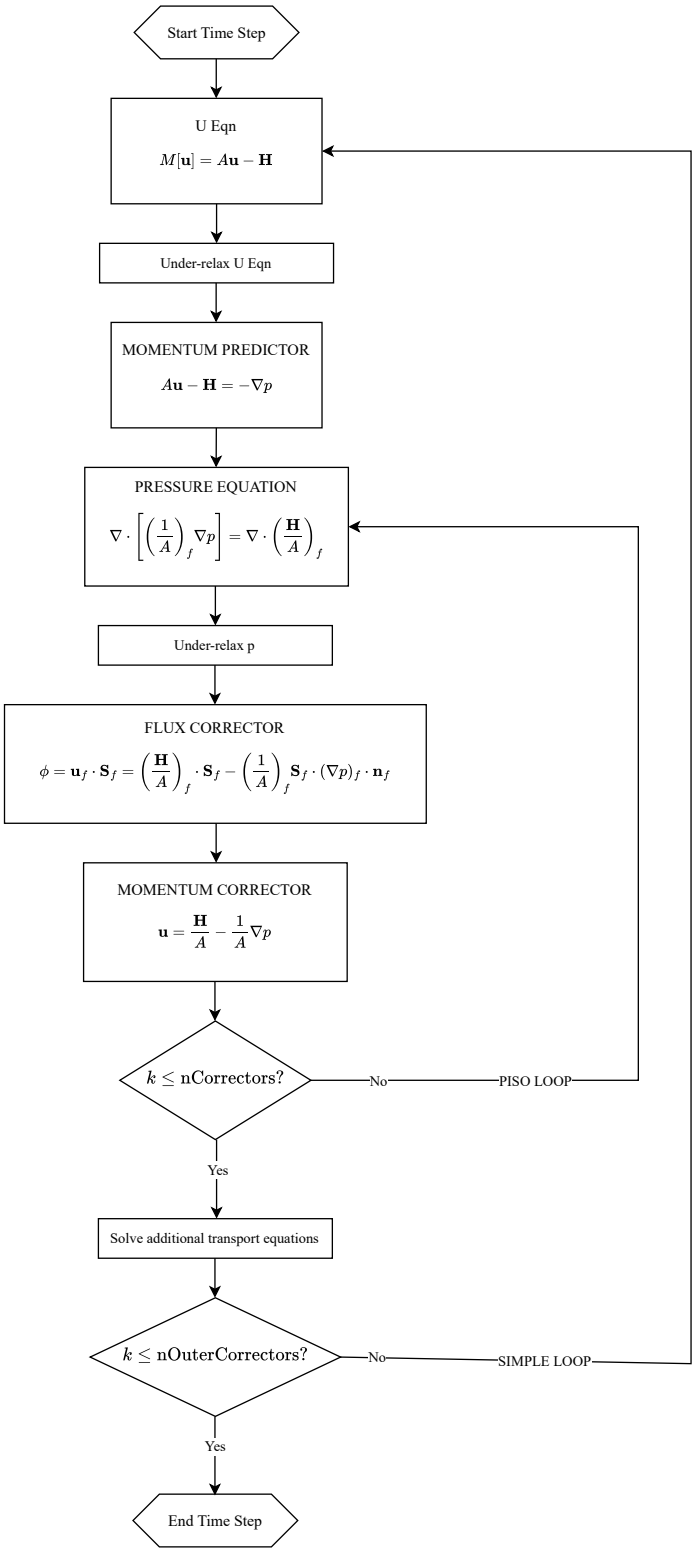


Figure 3.8: PIMPLE algorithm flowchart.

loops: an outer SIMPLE loop and an inner PISO loop. At the beginning of a new time step, the momentum predictor stage solves the momentum equation using the pressure field from the previous iteration and obtains a first tentative value of the velocity. Next, in the pressure equation stage, this predicted velocity field is used to calculate the pressure field that makes the solution conservative. Finally, in the momentum corrector stage, this new pressure field is used to obtain the corrected velocity field that satisfies the mass conservation.

With this framework in mind, it is possible to define the PISO and SIMPLE loops. The PISO loop starts from the momentum corrector stage and loops back to the pressure equation stage. The SIMPLE loop, instead, starts from the momentum corrector stage and returns to the beginning at the momentum equation stage (`U Eqn`). The main idea is that the SIMPLE loop alone is computationally slower because it returns to the momentum equation stage at every iteration, while the PISO loop is faster because it reiterates only from the pressure equation stage. However, PISO alone is unstable for $Co > 1$. Therefore, when it is necessary to perform simulations with a target Courant number greater than one, the PIMPLE algorithm is typically employed. It acts as a hybrid blend between PISO and SIMPLE, which combines computational efficiency with numerical stability. To ensure an optimal balance between execution speed and stability, two outer SIMPLE cycles (`nOuterCorrectors`) and two inner PISO cycles (`nCorrectors`) were selected for this simulation.

3.6.2.2 Relaxation Factors

Under-relaxation factors [8–11] are widely employed to improve numerical convergence in complex flow scenarios. For a general quantity Q, the relaxed value is defined as:

$$Q^{n+1} = Q^n + \alpha \left(\tilde{Q}^{n+1} - Q^n \right) \tag{3.30}$$

where Q^n is the solution calculated from the previous iteration, $\tilde{Q}^{n+1}$ is the unrelaxed estimate and Q^{n+1} is the actual value used for the step $(n+1)$, with $0 < \alpha \leq 1$. Rather than using the new result directly, an intermediate lower value is adopted to reduce large variations between the iterations. The behavior depends on α: for $\alpha = 0$, the old state is retained ($Q^{n+1} = Q^n$), whereas for $\alpha = 1$, the newly calculated result is used without relaxation ($Q^{n+1} = \tilde{Q}^{n+1}$). For α between these extremes, the solution balances the two limiting cases: closer α is to 1, closer the updated result is to the newly computed solution, leading to faster convergence but less numerical stability. On the other hand, the closer α is to 0, the further the update is from the new computed solution, thereby mitigating the risk of numerical instability at the cost of higher computational time.

For the current simulation, the under-relaxation factors listed in Table 3.5 were adopted:

Category	Physical Quantity	Relaxation Factor (α)
fields	p	0.4
equations	$\mathbf{u}$	0.8
equations	k	0.7
equations	ω	0.7

Table 3.5: Relaxation factors for fields and equations.

3.6.2.3 Solvers

For $\mathbf{u}$, k, and ω, the `smoothSolver` with a `GaussSeidel` smoother was chosen. The core idea behind the Gauss-Seidel [8–11] method is the following. To illustrate the approach, a general system of linear equations is introduced:

$$A\mathbf{\Phi} = \mathbf{b} \tag{3.31}$$

where A is the coefficient matrix, $\mathbf{b}$ is the vector of known terms and $\mathbf{\Phi}$ is the vector of unknown variables. The matrix A can be decomposed into three parts as follows:

$$A = D + L + U \tag{3.32}$$

where D is the diagonal matrix, L is the strictly lower triangular matrix, and U is the strictly upper triangular matrix of A. Substituting this decomposition into Equation (3.31) yields:

$$(D + L + U)\mathbf{\Phi} = \mathbf{b} \tag{3.33}$$

To solve the system, the Gauss-Seidel method evaluates the unknown vector at the new iteration $\mathbf{\Phi}^{(k+1)}$ for the terms multiplied by D and L, while employing the previous values $\mathbf{\Phi}^{(k)}$ for those multiplied by U as follows:

$$(D + L)\mathbf{\Phi}^{(k+1)} = \mathbf{b} - U\mathbf{\Phi}^{(k)} \tag{3.34}$$

The vector form of the Gauss-Seidel method is obtained, by isolating $\mathbf{\Phi}^{(k+1)}$ as:

$$\mathbf{\Phi}^{(k+1)} = -(D + L)^{-1}U\mathbf{\Phi}^{(k)} + (D + L)^{-1}\mathbf{b} \tag{3.35}$$

The method can also be expressed in index notation as:

$$\Phi_i^{(k+1)} = \frac{1}{a_{ii}}\left(b_i - \sum_{j=1}^{i-1} a_{ij}\Phi_j^{(k+1)} - \sum_{j=i+1}^{N} a_{ij}\Phi_j^{(k)}\right) \quad i = 1, 2, 3, \ldots, N \tag{3.36}$$

Since Gauss-Seidel is an iterative method, a stopping criterion is required to determine when it is possible to terminate the computation. For this purpose, the residual vector at iteration k is defined as:

$$\mathbf{r}^{(k)} = \mathbf{b} - \mathbf{A}\Phi^{(k)} \tag{3.37}$$

This vector represents the residual error between the exact solution and the computed one, which can be expressed as the difference between $\mathbf{b}$ and $A\mathbf{\Phi}^{(k)}$.The exact solution corresponds to a null residual ($\mathbf{r} = \mathbf{0}$), which cannot be achieved in practice using an iterative method. It is therefore necessary to define a tolerance that is small enough for the specific case. In the present work, a residual tolerance of $\epsilon = 10^{-8}$ was selected:

$$|\mathbf{r}^{(k)}| \leq 10^{-8} \tag{3.38}$$

This specific threshold was set to guarantee high precision. As for the solver, the Gauss-Seidel method was selected because it is highly effective for solving transport equations.

For the pressure equation, on the other hand, the Geometric-Algebraic Multigrid (GAMG) solver was chosen, with Gauss-Seidel as a smoother. Unlike the previous solver, this formulation relies on a different numerical approach. The main motivation behind the method is that the computational cost of a standard iterative solver, such as Gauss-Seidel or Jacobi, increases significantly with the size of the algebraic system, which represents

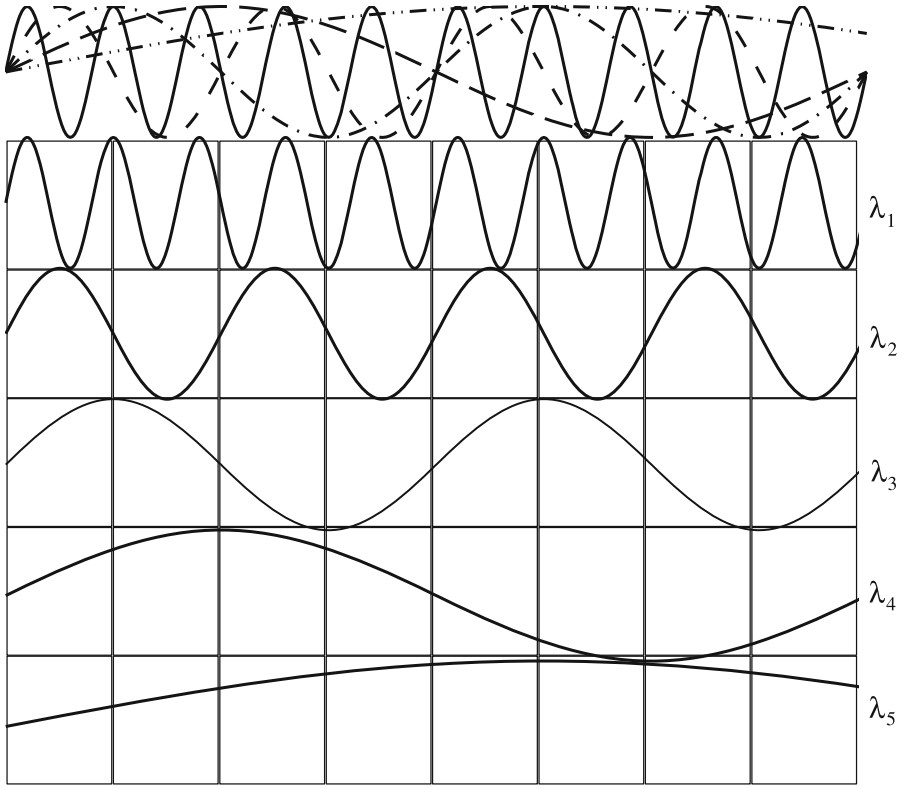


Figure 3.9: Progression of error modes in a one-dimensional grid [9].

a major limitation. Specifically, these schemes are very effective at eliminating high-frequency errors but have more difficulty in removing low-frequency components, when a fine grid is used. Figure 3.9 illustrates a signal decomposed into its distinct error modes, ranging from a high frequency λ_1 to a low frequency λ_5. These modes are shown together in the top panel and plotted individually in separate panels below, on the same computational grid. As can be seen, the high-frequency components are highly oscillatory, with rapid variations occurring across the computational cells, making them easily captured by the grid scale. As the wavelength increases, the signal becomes smoother relative to the grid, resulting in minimal variation between neighboring cells. The problem with iterative methods like Gauss-Seidel arises because their underlying mechanism relies on differences between adjacent cell values; these are extremely small for low-frequency errors on fine meshes, leading to a very slow error reduction, even if the remaining error is still significant. This effect worsens as the mesh is further refined, explaining why the convergence rate drops when the system size is increased.

Multigrid methods address this issue with a simple yet effective idea. The scheme begins with some classical pre-smoothing steps with the chosen smoother, in this case Gauss-Seidel, on the original grid, which is necessary before coarsening to reduce the interpolation errors. It then switches to a coarser grid where it performs additional iterations. Thanks to this change, the smoother sees a high-frequency error instead, making it easier to remove. Finally, the method returns to the finer grid and performs a few post-smoothing steps to damp the remaining error alongside any high-frequency artifacts introduced by the coarsening process. It is worth noting that the mesh and its geometry remain unchanged throughout the process, since the coarsening process is purely algebraic. In the present work, GAMG has been selected for the pressure since the equation is elliptic and this choice accelerates the convergence. Furthermore, a residual tolerance of 10^{-7} was

prescribed, as expressed by:

$$|\mathbf{r}^{(k)}| \leq 10^{-7} \tag{3.39}$$

Chapter 4

Results

The simulation results are structured across the following sections. Specifically, the investigation combines a qualitative characterization of the flow fields around both bodies with a targeted quantitative benchmark against reference LES data for the main flow variables around the canopy. The detailed numerical comparison is intentionally focused on the canopy, as it is the aerodynamic component of primary interest. Given the inherently unsteady nature of bluff-body wakes, the subsequent analysis evaluates both averaged statistics and instantaneous flow structures to capture this continuous evolution. Here, the averaging procedure comprises two steps: a time average to filter out temporal fluctuations and an azimuthal (θ) average to exploit the physical axisymmetry of the configuration. This dual-averaging approach allows the flow field and extracted statistics to be displayed on a single reference x-r plane at $\theta = 0°$ without loss of generality. Furthermore, unless explicitly stated otherwise, all flow variables and fields reported in this chapter are in dimensionless form.

To present these results systematically, the analysis is organized as follows. Section 4.1 investigates the main flow variables, namely the velocity u and pressure coefficient c_p distributions. Section 4.2 evaluates the aerodynamic loads on the canopy, while Section 4.3 examines the surrounding flow topology and the primary flow mechanisms developing around it. Finally, Section 4.4 analyzes the behavior of the dynamic RANS turbulence closure parameters.

4.1 Velocity and Pressure Coefficient Distributions

One of the fundamental criteria for evaluating the physical accuracy of a numerical model lies in the examination of the velocity and pressure fields, which constitute the primitive variables solved by the Navier-Stokes equations. To enable a direct comparison with reference LES data, velocity is normalized by its freestream value ($U_\infty = 1$ m/s), while the pressure is expressed through the pressure coefficient c_p using the freestream dynamic pressure per unit mass ($q_\infty = \frac{1}{2}U_\infty^2 = 0.5$ m^2/s^2), in accordance with OpenFOAM's incompressible formulation where the solver natively computes kinematic pressure (p/ρ).

4.1.1 Velocity

The analysis starts with the instantaneous velocity magnitude field around the capsule, shown in Figure 4.1. As can be observed, the flow stagnates upon impinging the hemispherical nose, before remaining attached along the entire cylindrical section up to the abrupt change in slope along the midsection. At this location, the flow separates and forms a first

recirculation bubble within the cavity bounded by the sloped shoulder and the spherical tail section. Subsequently, the flow briefly reattaches along this curved surface before separating permanently to form an unsteady wake, generating a second recirculation bubble behind the object.

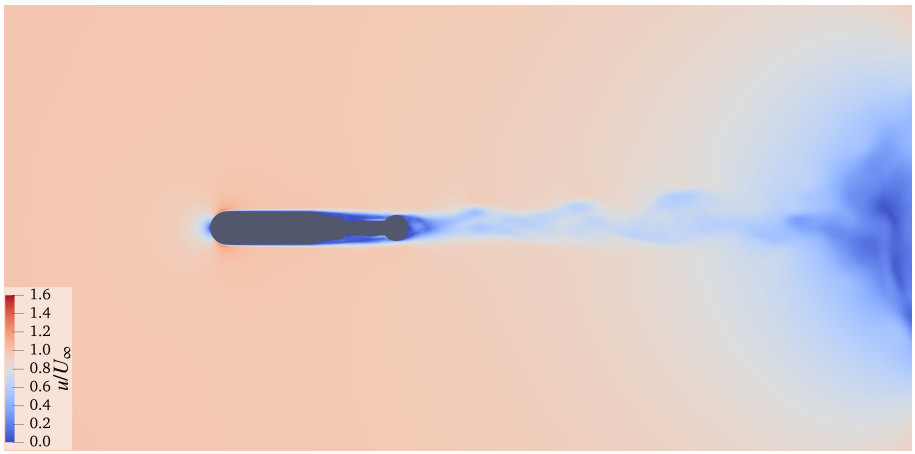


Figure 4.1: Instantaneous normalized velocity magnitude (u/U_∞) field around the capsule in the x-r plane at $\theta = 0°$.

The resulting flow topology is further illustrated in Figure 4.2, where the instantaneous velocity magnitude field is visualized using Line Integral Convolution (LIC). As can be observed, both aforementioned recirculation regions are clearly highlighted, along with the temporary reattachment on the rear spherical surface.

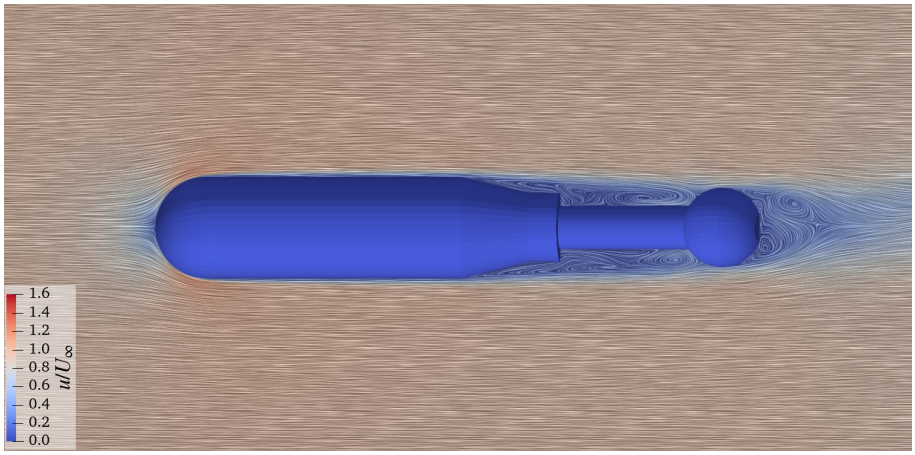


Figure 4.2: Instantaneous normalized velocity magnitude (u/U_∞) field around the capsule visualized using LIC in the x-r plane at $\theta = 0°$.

Downstream of the capsule lies the canopy, which, as noted earlier, represents the most critical body in the simulation and is therefore the primary focus of the following detailed analysis. Indeed, the flow structures associated with the canopy are significantly more intense than those surrounding the forebody, exhibiting continuous and severe unsteadiness throughout the simulation, as described in more detail in Section 4.3. Specifically, three main flow regions can be identified around the canopy: the cavity, the wake, and the vent jet. These regions, illustrated in Figure 4.3, establish the spatial framework that will be used for the entire analysis presented in this chapter.

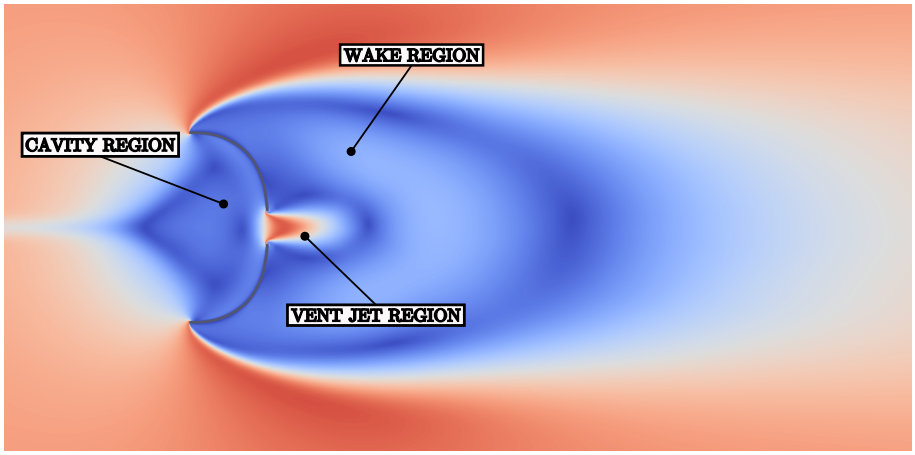


Figure 4.3: Cavity, wake, and vent jet regions around the canopy, superimposed on the mean normalized velocity magnitude (U/U_∞) field.

In the canopy cavity, the incoming air is abruptly decelerated by the interior surface and forced into a swirling motion, forming a first recirculation bubble. Within this region, the flow unsteadiness is further intensified by the incoming oscillatory wake generated by the capsule. Here, the flow remains detached from the surface, continuously recirculating within the cavity until it is eventually expelled through the vent or over the canopy skirt

In the canopy wake region, however, the flow is not completely separated; instead, it briefly attaches to the canopy skirt over a time-varying distance before separating to form the canopy wake, which contains a second recirculation bubble in its near-wake region. This early separation generates a wake wider than the canopy diameter itself, governed by two main phenomena, namely vortex shedding and bubble pumping, which are addressed in detail in Section 4.3.

The instability within this region is further amplified by the high-speed jet emerging from the vent. In this area, the flow trapped inside the cavity briefly reattaches to the inner canopy surface before separating at the sharp exit edge. Consequently, a portion of the flow originally decelerated inside the cavity escapes through the vent as a high-velocity jet, which sharply contrasts with the low-speed recirculating flow in the near wake. This velocity mismatch, coupled with global wake dynamics such as bubble pumping, leads to a strong interaction between the vent jet and the surrounding flow field, forcing the jet to continually alter its topology through rapid elongation, contraction, and radial deflection over time.

All these flow phenomena are further highlighted by the LIC visualization of the instantaneous velocity magnitude field shown in Figure 4.5, where the vortical structures within the canopy cavity, along the wake shear layer, and in the vent jet region are clearly observable.

Turning now to the LES results, the instantaneous velocity magnitude obtained from the simulation is shown in Figure 4.6. A striking difference that can be immediately observed is the level of resolved detail that emerges when compared to the dynamic RANS solution, as LES is able to capture a much wider spectrum of turbulent scales thanks to the significantly finer computational grid. In particular, in the plane where the fields of this chapter are plotted (x-$r, \theta = 0$), the dynamic RANS grid contains 413 120 cells, whereas the LES mesh contains 2 094 081 cells. Hence, this single plane in the LES grid accounts for nearly half of the total cell count of the full 3D RANS domain.

In light of the differences in the computational grids, directly evaluating the instan-

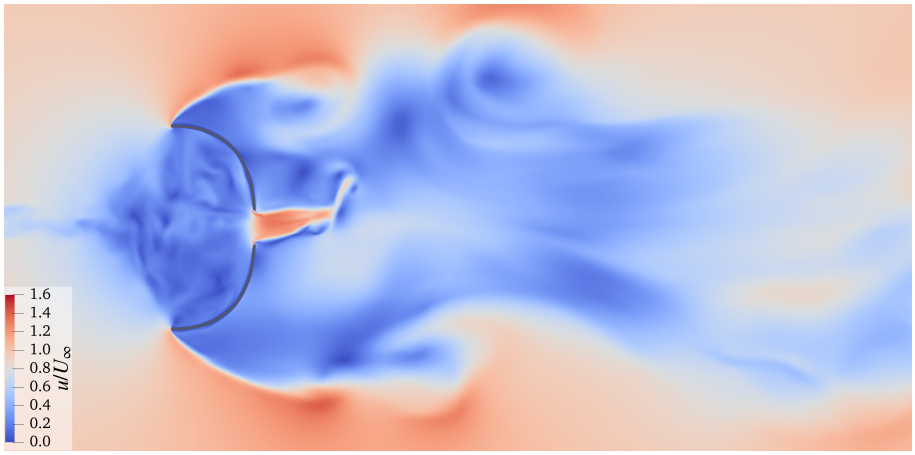


Figure 4.4: Instantaneous normalized velocity magnitude (u/U_∞) field around the canopy in the x-r plane at $\theta = 0°$.

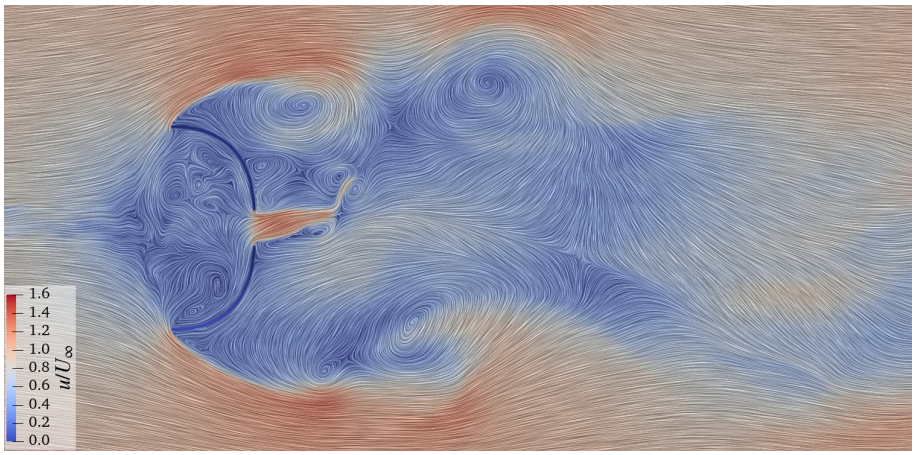


Figure 4.5: Instantaneous normalized velocity magnitude (u/U_∞) field around the canopy visualized using LIC in the x-r plane at $\theta = 0°$.

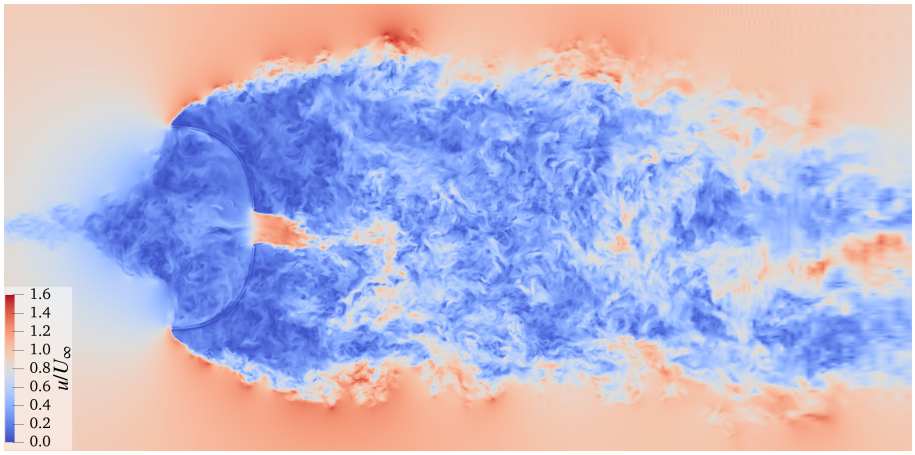


Figure 4.6: Instantaneous normalized velocity magnitude (u/U_∞) field around the canopy from the LES simulation in the x-r plane at $\theta = 0°$.

taneous fields would not be appropriate. Instead, a more insightful assessment can be achieved by examining the mean fields of the two in-plane velocity components, namely U_x and U_r, at various axial positions. Specifically, $x/D = 1.20$ was selected to evaluate the front region of the canopy, whereas $x/D = 2.00$, $x/D = 2.25$, and $x/D = 2.50$ were chosen for the wake region. These specific locations are adopted for all subsequent flow field comparisons throughout this chapter. In Figure 4.7, these x/D positions are overlaid on the mean velocity magnitude field U of the dynamic RANS solution.

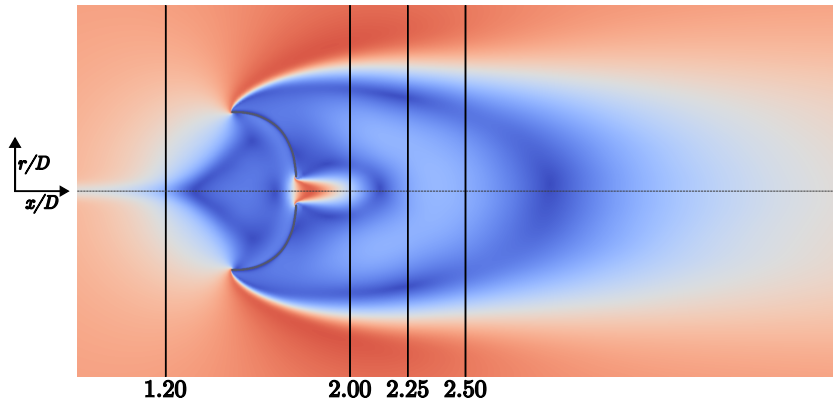
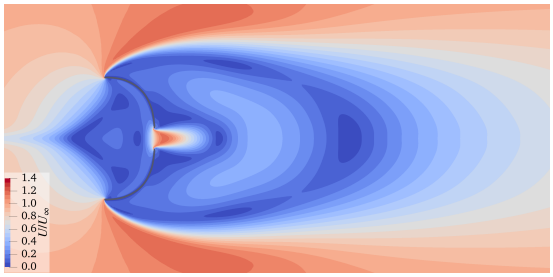


Figure 4.7: Locations of the selected extraction lines at $x/D = 1.20, 2.00, 2.25$, and 2.50, superimposed on the mean normalized velocity magnitude (U/U_∞) field.

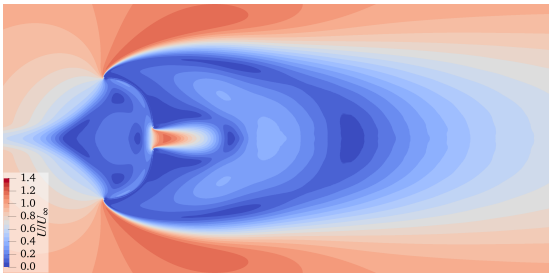
Figure 4.8 compares the mean velocity fields obtained from the dynamic RANS and LES models, in terms of velocity magnitude (U), axial component (U_x), and radial component (U_r). Overall, the velocity fields predicted by the two models exhibit remarkable agreement. A notable difference, however, lies in the spatial extent of the mean flow features: the vent jet, as well as the low-velocity region within the canopy cavity and the wake, appears slightly more expanded axially in the LES solution. This behavior can be attributed to the higher grid density in the LES model, which enhances the resolution of turbulent mixing along the shear layers, thereby better capturing its interaction with the surrounding flows. Nevertheless, despite localized discrepancies across the domain, the dynamic RANS model reproduces all examined velocity distributions with high fidelity.

To better appreciate these results from a quantitative standpoint, Figure 4.9 compares the axial velocity profiles (U_x) across the axial sections defined in Figure 4.7, plotted along the normalized radial coordinate r/D at a fixed azimuth $\theta = 0°$. Overall, the velocity distributions exhibit excellent alignment, with minor discrepancies localized near the centerline ($r/D \approx 0$). Specifically, at $x/D = 2.00$ and $x/D = 2.25$, the dynamic RANS model predicts slightly lower velocity values around $r/D \approx 0$, whereas an overestimation occurs at $x/D = 1.20$. These localized differences diminish rapidly and disappear beyond $r/D \approx 0.30$, where the curves collapse onto each other.

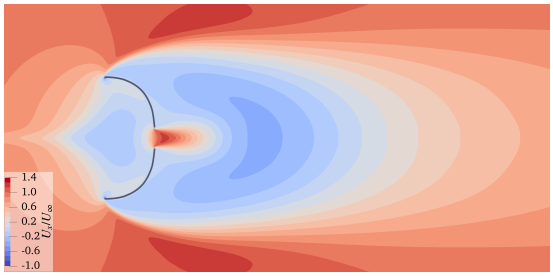
Figure 4.10, on the other hand, presents the comparison of the U_r component. In these plots as well, a very similar trend between the curves can be observed. In particular, starting from the centerline ($r/D = 0$), the dynamic RANS solution yields marginally lower magnitudes at $x/D = 1.20$, $x/D = 2.25$ and $x/D = 2.50$, contrasted by a modest overestimation at $x/D = 2.00$. These localized discrepancies gradually fade and fully disappear around $r/D \approx 0.70$, thereby extending further radially than observed for the U_x component. The primary differences emerge at $x/D = 2.00$ and $x/D = 2.25$, corresponding to locations inside the vent jet and immediately downstream of it, respectively. These



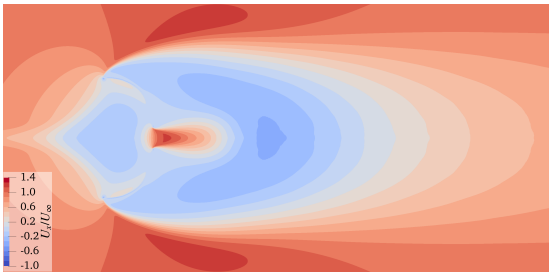
(a) RANS: Mean velocity magnitude (U/U_∞)



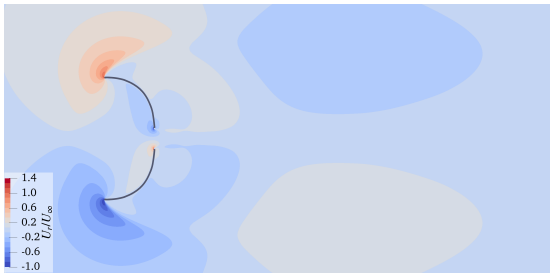
(b) LES: Mean velocity magnitude (U/U_∞)



(c) RANS: Mean axial velocity (U_x/U_∞)



(d) LES: Mean axial velocity (U_x/U_∞)



(e) RANS: Mean radial velocity (U_r/U_∞)



(f) LES: Mean radial velocity (U_r/U_∞)

Figure 4.8: Comparison of the mean normalized velocity fields between the dynamic RANS (left) and LES (right) models around the canopy: velocity magnitude U/U_∞ (top), axial velocity U_x/U_∞ (middle), and radial velocity U_r/U_∞ (bottom).

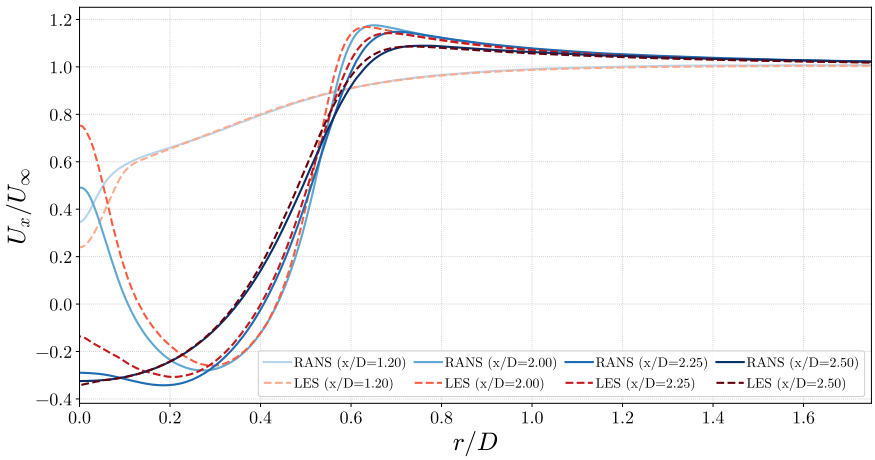


Figure 4.9: Comparison of the mean normalized axial velocity (U_x/U_∞) profiles between the dynamic RANS and the LES models along the radial coordinate r/D at $x/D = 1.20, 2.00, 2.25$, and 2.50.

distributions exhibit a more pronounced deviation between the solutions, despite maintaining the same overall profile shape. This divergence is likely attributable to the sharp radial velocity gradients in this region caused by the jet motion, which generate fine-scale turbulent fluctuations that the RANS grid is too coarse to fully resolve. An additional contribution stems from the downstream elongation of the jet in the LES solution, such that extracting distributions at identical nominal x/D positions effectively compares the jet at different stages of its axial decay, ultimately yielding localized mismatches in profile shape.

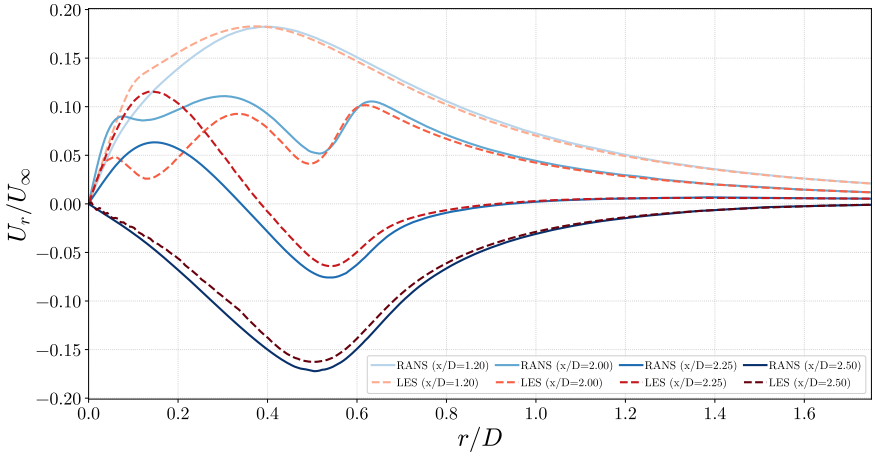


Figure 4.10: Comparison of the mean normalized radial velocity (U_r/U_∞) profiles between the dynamic RANS and the LES models along the radial coordinate r/D at $x/D = 1.20, 2.00, 2.25$, and 2.50.

To further investigate the discrepancies between the two models, second-order statistics are evaluated through the root-mean-square (RMS) of velocity fluctuations, namely the axial ($u'_{x,\mathrm{rms}}$), radial ($u'_{r,\mathrm{rms}}$), and azimuthal ($u'_{\theta,\mathrm{rms}}$) components, as shown in Figure 4.11. As expected, due to variations in mesh resolution and resolved scales, these mismatches are

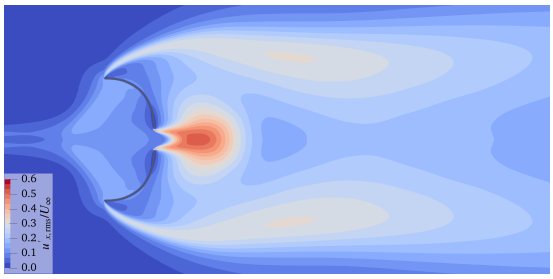
more pronounced here than in the first-order statistics. In particular, the axial component ($u'_{x,\mathrm{rms}}$), presented in Figures 4.11a and 4.11b, indicates that the dynamic RANS model yields higher values immediately downstream of the jet, whereas the LES solution exhibits slightly more intense fluctuations at different locations within the flow field. Despite these localized discrepancies, the two fields exhibit strong overall similarity.

With respect to the remaining two components, the observed variations are moderately more pronounced. Regarding the radial component ($u'_{r,\mathrm{rms}}$), presented in Figures 4.11e and 4.11f, the dynamic RANS solution exhibits higher damping across nearly the entire canopy wake and cavity. Specifically, three main regions are identified. The first is located along the side of the canopy wake, immediately downstream of the skirt separation, where a distinct discontinuity in fluctuations is observed between the boundary layer and the rest of the shear layer. The second is located in the turbulent jet, where the dynamic RANS model underestimates the fluctuation values upstream. Finally, a third region is located at the rear portion of the recirculation bubble. These discrepancies were expected, considering that these fields represent the scales directly resolved by the numerical model. Consequently, the mesh is too coarse to resolve the initial scales of the wake shear layer, as well as many of the smaller turbulent structures present in the inner wake. These identified zones are of primary importance, as these localized reductions will also manifest in some subsequent fields. The same regions are visible for the azimuthal velocity component ($u'_{\theta,\mathrm{rms}}$). In addition, it is possible to observe two distinct peaks of high fluctuation at the outer edge of the vent jet attached to the rear part of the canopy, which are entirely absent in the LES solution.

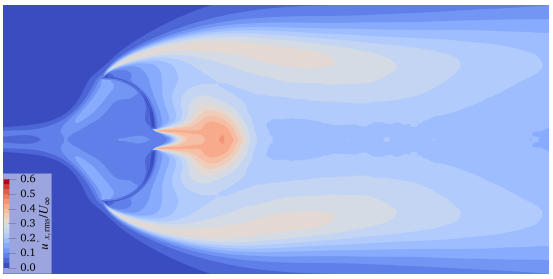
To complement the qualitative insights obtained from the two-dimensional flow fields, a quantitative comparison of the velocity fluctuation profiles is conducted. Figure 4.12 shows the distributions of the root-mean-square axial velocity fluctuations ($u'_{x,\mathrm{rms}}$) at various axial locations (x/D). This quantitative analysis confirms the flow behavior previously observed in the contour plots. In general, as noted for the mean flow field, the dynamic RANS model accurately captures the overall profile topology, closely matching the reference data. At $x/D = 1.20$, corresponding to the canopy cavity region, the fluctuation intensity remains extremely low, and the dynamic RANS and LES curves virtually collapse onto each other. Moving downstream to $x/D = 2.00$, an initial overprediction of the fluctuations by the dynamic RANS model is visible; however, beyond $r/D \approx 0.2$, the curve drops back down, returning to the expected trend of lower fluctuation values. At $x/D = 2.25$ and $x/D = 2.50$, the dynamic RANS model underestimates fluctuation levels across the inner radial region. Moving further outward toward $r/D \approx 0.6$, however, all the profiles reconverge with the LES baseline, exhibiting only minor localized overestimations at specific radial positions.

A similar pattern, characterized by a slight underestimation of fluctuations at small radial distances (r/D) followed by a minor overestimation further outward along the radius, can be observed in Figure 4.13, where the radial profiles of the root-mean-square radial velocity fluctuations ($u'_{r,\mathrm{rms}}$) are displayed. The sole exception to this behavior occurs at the $x/D = 2.50$ station, which exhibits a slight initial overestimation near the centerline ($r/D \approx 0$). Nevertheless, despite these local differences, the curves remain in close agreement, and the dynamic RANS model successfully reproduces the overall trend.

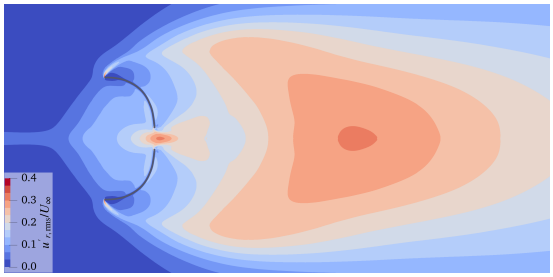
In contrast to the alternating trend observed for the previous components, a systematic underestimation can be seen by examining examining the azimuthal root-mean-square velocity fluctuation profiles ($u'_{\theta,\mathrm{rms}}/U_\infty$) shown in Figure 4.14, with only a slight overestimation near $r/D \approx 0$ for $x/D = 2.50$. In particular, it is possible to observe that,



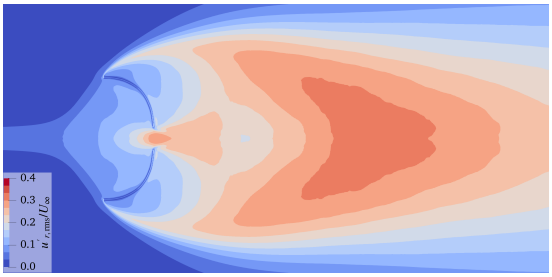
(a) RANS: RMS of the axial velocity fluctuations ($u'_{x,\mathrm{rms}}/U_\infty$)



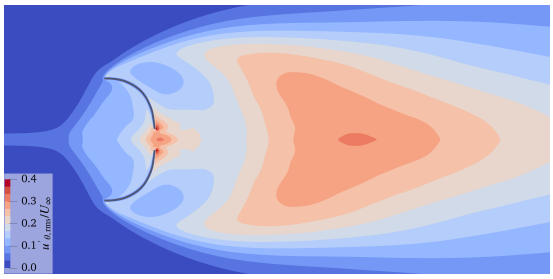
(b) LES: RMS of the axial velocity fluctuations ($u'_{x,\mathrm{rms}}/U_\infty$)



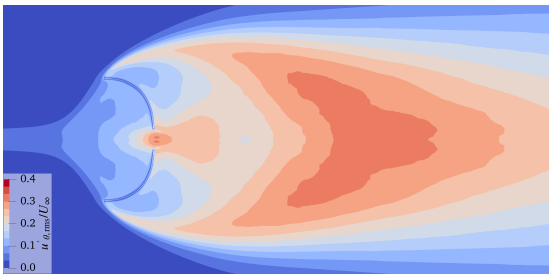
(c) RANS: RMS of the radial velocity fluctuations ($u'_{r,\mathrm{rms}}/U_\infty$)



(d) LES: RMS of the radial velocity fluctuations ($u'_{r,\mathrm{rms}}/U_\infty$)



(e) RANS: RMS of the azimuthal velocity fluctuations ($u'_{\theta,\mathrm{rms}}/U_\infty$)



(f) LES: RMS of the azimuthal velocity fluctuations ($u'_{\theta,\mathrm{rms}}/U_\infty$)

Figure 4.11: Comparison of the normalized root-mean-square (RMS) velocity fluctuations fields between the dynamic RANS (left) and LES (right) models around the canopy: axial component $u'_{x,\mathrm{rms}}/U_\infty$ (top), radial component $u'_{r,\mathrm{rms}}/U_\infty$ (center), and azimuthal component $u'_{\theta,\mathrm{rms}}/U_\infty$ (bottom).

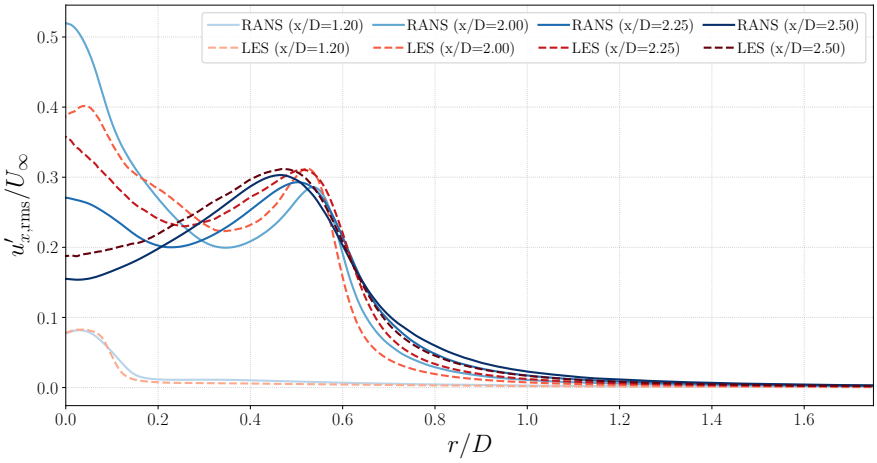


Figure 4.12: Comparison of the normalized axial root-mean-square velocity fluctuations ($u'_{x,\mathrm{rms}}/U_\infty$) profiles between the dynamic RANS and LES models along the radial coordinate r/D at $x/D = 1.20, 2.00, 2.25$, and 2.50.

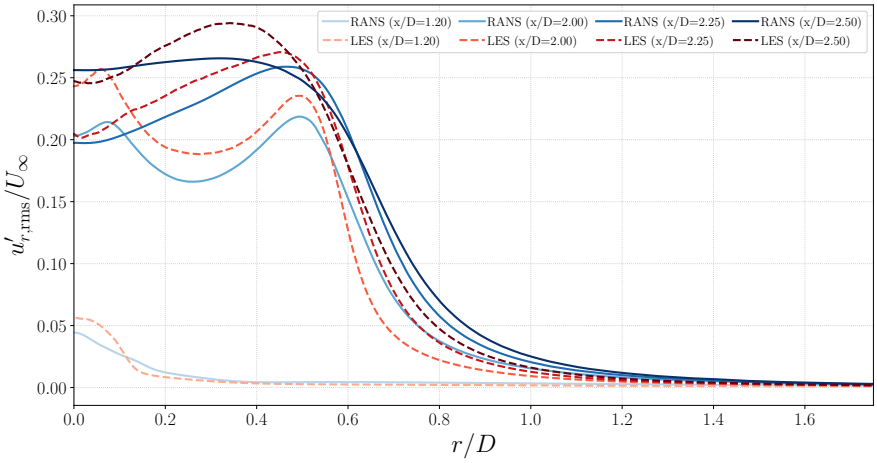


Figure 4.13: Comparison of the normalized radial root-mean-square velocity fluctuations ($u'_{r,\mathrm{rms}}/U_\infty$) profiles between the dynamic RANS and LES models along the radial coordinate r/D at $x/D = 1.20, 2.00, 2.25$, and 2.50.

despite the coarser discretization in the azimuthal direction, the differences between the two curves remain limited, demonstrating that the reduced resolution does not drastically alter the overall results. The only axial location exhibiting a more noticeable mismatch is $x/D = 2.00$, corresponding to the vent jet region. Nevertheless, the profile is still well captured, and the deviation remains relatively modest.

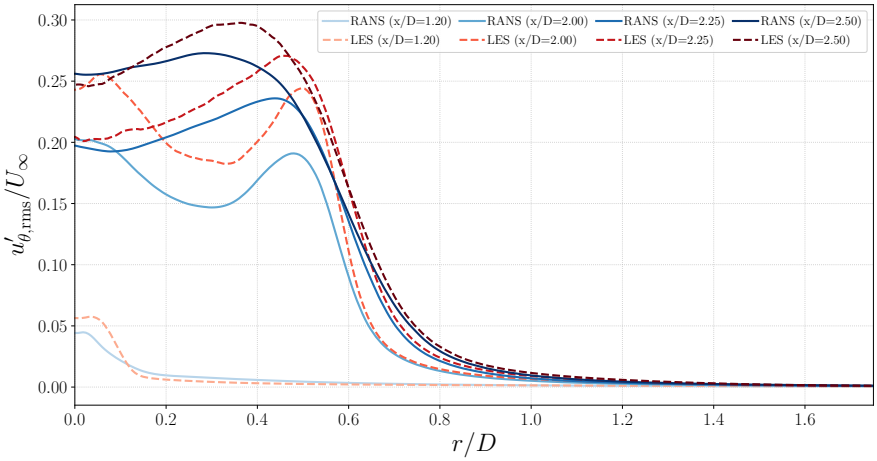


Figure 4.14: Comparison of the normalized azimuthal root-mean-square velocity fluctuations ($u'_{\theta,\mathrm{rms}}/U_\infty$) profiles between the dynamic RANS and LES models along the radial coordinate r/D at $x/D = 1.20, 2.00, 2.25$, and 2.50.

4.1.2 Pressure Coefficient

The analysis continues with the study of the pressure coefficient field around the capsule. Specifically, Figure 4.15 displays the mean pressure coefficient (C_p). As can be observed, C_p reaches its maximum value at the stagnation point ($C_p \approx 1$), where the velocity was previously shown to be zero, and progressively decreases up to the point of maximum curvature. It then increases along the subsequent straight section, recovering toward the freestream value ($C_p \approx 0$). Another local acceleration region occurs near the rounded trailing edge, where the flow briefly reattaches. Following final separation, the pressure drops to a negative value within the recirculation region. Moving further downstream into the wake, it stabilizes slightly below the freestream pressure ($C_p \lesssim 0$), until it becomes influenced by the pressure field generated by the flow within the canopy cavity.

Considering now the instantaneous pressure coefficient field around the canopy shown in Figure 4.16, the flow exhibits significantly larger pressure fluctuations compared to the capsule region, confirming the parachute as the primary feature of interest in the simulation. First, a high-pressure region ($c_p > 1$) develops within the canopy cavity, originating slightly upstream of the structure and extending inside it. Conversely, a region of negative c_p forms behind the canopy, driven by the boundary layer detachment along the parachute skirt and expanding across the near wake. Further downstream, c_p gradually recovers toward the freestream value ($c_p \approx 0$) along the streamwise direction. Another key feature is the presence of low-pressure cores within the wake vortices: originating as small-scale eddies at the canopy skirt, these vortices grow as they are convected downstream, developing into large-scale coherent structures characterized by increasingly negative core pressure until they are eventually dissipated.

Figure 4.17, instead, presents the instantaneous c_p field obtained from the LES simu-

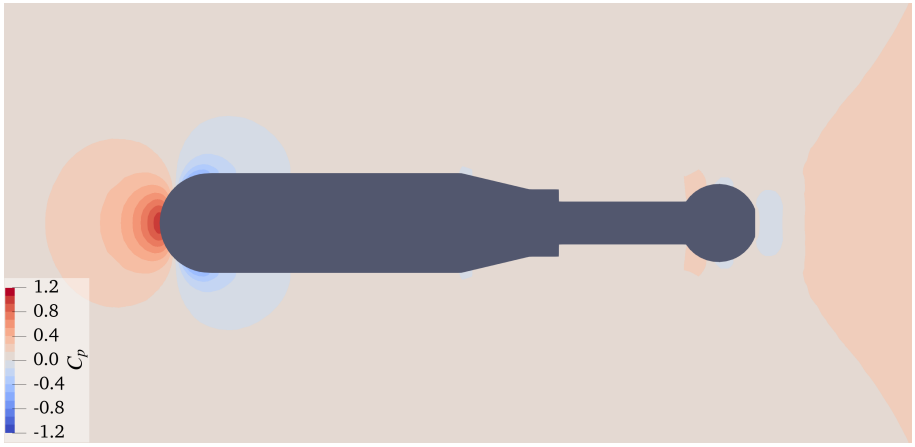


Figure 4.15: Mean pressure coefficient (C_p) field around the capsule in the x-r plane at $\theta = 0°$.

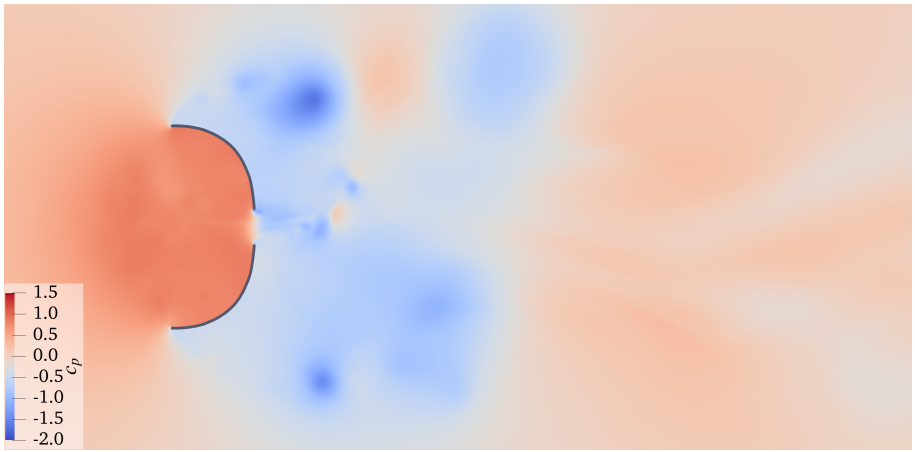


Figure 4.16: Istantaneous pressure coefficient (c_p) field around the canopy in the x-r plane at $\theta = 0°$.

lation. As can be observed, thanks to its higher spatial resolution, LES provides a clearer representation of vortex generation at the canopy skirt, capturing smaller-scale vortices that remain unresolved in the dynamic RANS due to mesh coarseness. Furthermore, it resolves localized pressure fluctuations within the wake and canopy cavity region, which are again driven by turbulent structures smaller than the grid cut-off of the dynamic RANS simulation.

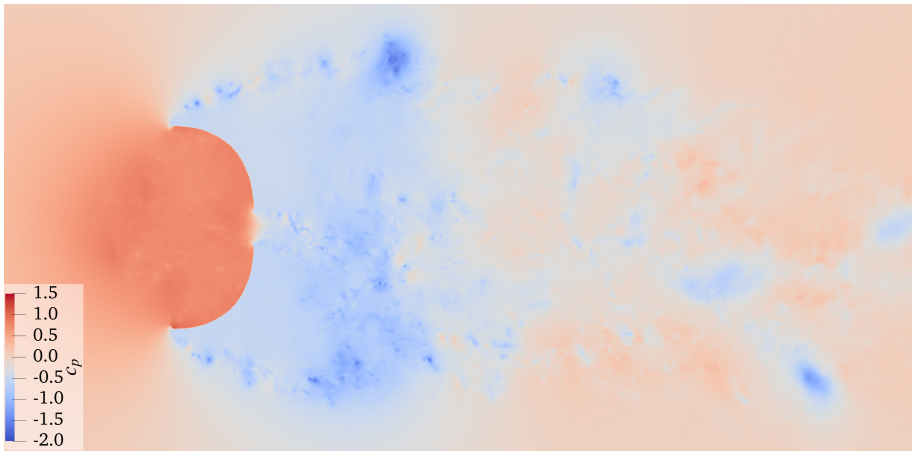
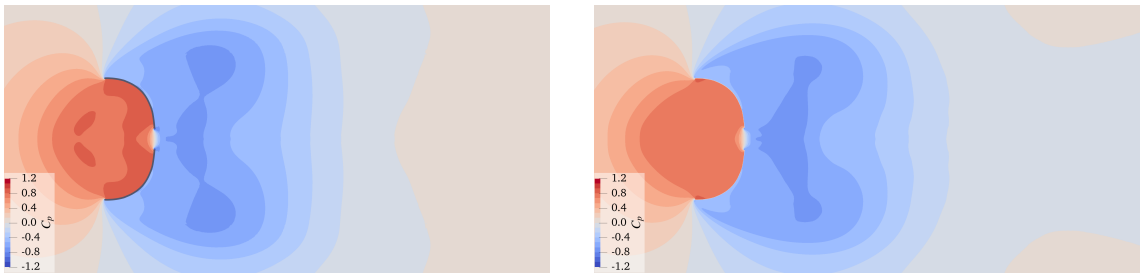


Figure 4.17: Istantaneous pressure coefficient (c_p) field around the canopy from the LES simulation in the x-r plane at $\theta = 0°$.

Similarly to the velocity analysis presented in the previous section, comparing the mean pressure coefficient (C_p) distributions provides key insights into the differences between the two numerical approaches. The C_p contours are shown in Figure 4.18. As can be observed, the pressure patterns show excellent agreement across the entire domain, with the dynamic RANS model exhibiting only a localized, slightly higher C_p magnitude inside the canopy cavity near the body. Furthermore, these fields highlight that the primary function of a parachute is to decelerate the suspended load, which is achieved by generating a strong pressure difference between the high-pressure region inside the cavity and the low-pressure wake behind it, thereby maximizing aerodynamic drag. The close agreement between the two models confirms that both approaches effectively capture this primary drag-generating mechanism.



(a) RANS: Mean pressure coefficient (C_p)

(b) LES: Mean pressure coefficient (C_p)

Figure 4.18: Comparison of the mean pressure coefficient (C_p) fields around the canopy between the dynamic RANS (left) and LES (right) models.

This alignment is further highlighted quantitatively in the profile comparisons presented in Figure 4.19. As can be appreciated from these distributions, the match between the two models follows the same trend previously noted for the mean velocity components,

but is even closer. Indeed, the curves virtually overlap, exhibiting only minor discrepancies especially near the axis ($r/D \approx 0$): specifically, a marginally lower value at $x/D = 1.20$ and $x/D = 2.25$, whereas at $x/D = 2.00$ and $x/D = 2.50$ the profile slightly overpredicts the solution near the centerline before marginally underpredicting further outward. Nevertheless, these differences remain negligible.

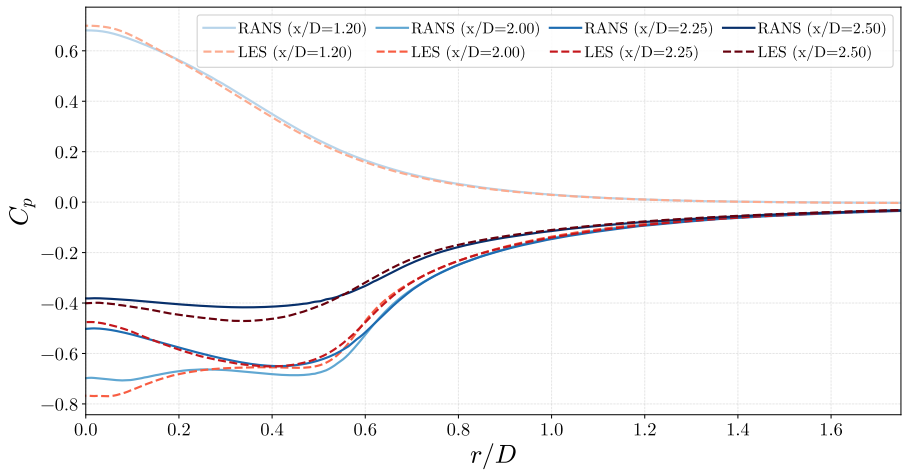


Figure 4.19: Comparison of the mean pressure coefficient (C_p) profiles between the dynamic RANS and the LES models along the radial coordinate r/D at $x/D = 1.20, 2.00, 2.25$, and 2.50.

Finally, an analysis is conducted on the root-mean-square of the pressure fluctuation coefficient ($c'_{p,\mathrm{rms}}$). As shown in Figure 4.20, the highest $c'_{p,\mathrm{rms}}$ values are concentrated in regions characterized by intense turbulence generation. Specifically, peak fluctuations develop along the shear layers originating from flow separation at the canopy skirt, as well as within the vent jet region. Here, a high value is induced by the collision of the jet with the low-velocity recirculation bubble, coinciding with the peak previously observed in $u'_{x,\mathrm{rms}}$. Furthermore, the $c'_{p,\mathrm{rms}}$ distribution exhibits a distinct gap along the shear layer near the canopy skirt before high values develop downstream in the wake, mirroring the behavior previously observed in the velocity fluctuations field.

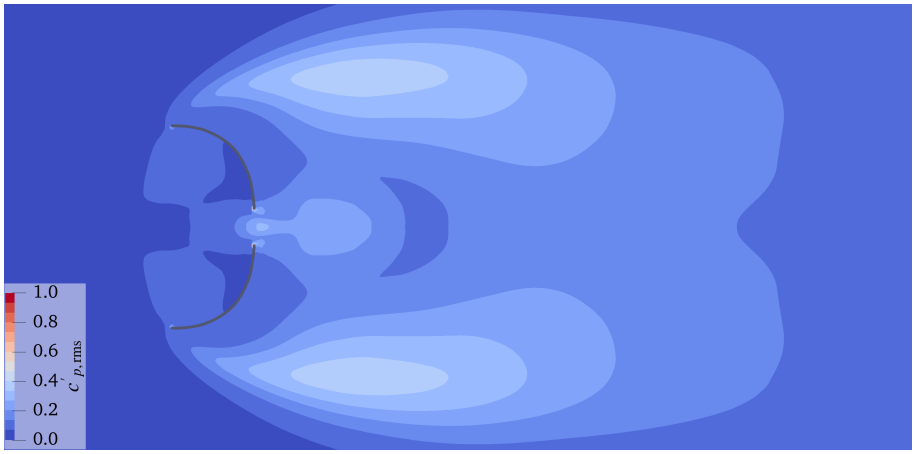


Figure 4.20: Root-mean-square of the pressure coefficient fluctuations ($c'_{p,\mathrm{rms}}$) field around the canopy in the x-r plane at $\theta = 0°$.

4.2 Aerodynamic Forces and Coefficients

The aerodynamic forces acting on the structure are fundamental parameters in industrial CFD applications and require accurate evaluation. Specifically, the fluid-solid interaction gives rise to net forces from which the main dimensionless coefficients are derived, as detailed in the following sections. In this study, only the forces associated with the canopy are considered numerically, as they are significantly higher in magnitude than those on the capsule, constituting the governing contribution.

To achieve the highest possible accuracy in computing the time-averaged coefficients, instantaneous values were sampled at every time step $\Delta t = 3 \times 10^{-4}\,\mathrm{s}$ throughout the simulation, covering a total normalized time window of $t/t_0 \approx 401$.

Furthermore, in contrast to the cylindrical reference frame adopted in the previous theoretical formulations, the local aerodynamic force components in this section are defined within a Cartesian reference frame (x, y, z). This choice is consistent with the internal computational framework of the OpenFOAM solver, which has resolved the instantaneous force vector along the principal grid axes. In this right-handed Cartesian system, the x-axis is aligned with the longitudinal symmetry axis of the canopy (coinciding with the main flow direction), while the y- and z-axes define the transverse cross-sectional plane, yielding the force vector $\mathbf{F} = (F_x, F_y, F_z)$.

Additionally, throughout this section, a specific notation is adopted to denote time-averaged quantities. While uppercase variables were used in the preceding chapters to represent time-averaged values, here time-averaged forces are explicitly indicated by an overbar (e.g., $\bar{F}$) to maintain clarity throughout the discussion.

4.2.1 Drag Coefficient

As previously mentioned, the focus of the simulation is a configuration composed of a capsule and a canopy. Unlike conventional aircraft or high-performance vehicles, whose primary functions are to generate lift and downforce respectively, this system operates under a different principle. The main objective is not to generate a force perpendicular to the direction of motion, but to decelerate the capsule during the descent phase by maximizing the force opposing the flow, namely aerodynamic drag. Within this framework, verifying the simulation accuracy in predicting this aerodynamic load is vital, given that this force serves as the primary baseline during the engineering design phase.

As detailed in the previous sections, the reference frame is aligned with the freestream velocity, with the positive x-axis oriented along the flow direction and opposite to the descent trajectory. Consequently, the canopy drag force $F_{D,\mathrm{canopy}}$ is defined as:

$$F_{D,\mathrm{canopy}} = F_{x,\mathrm{canopy}} \tag{4.1}$$

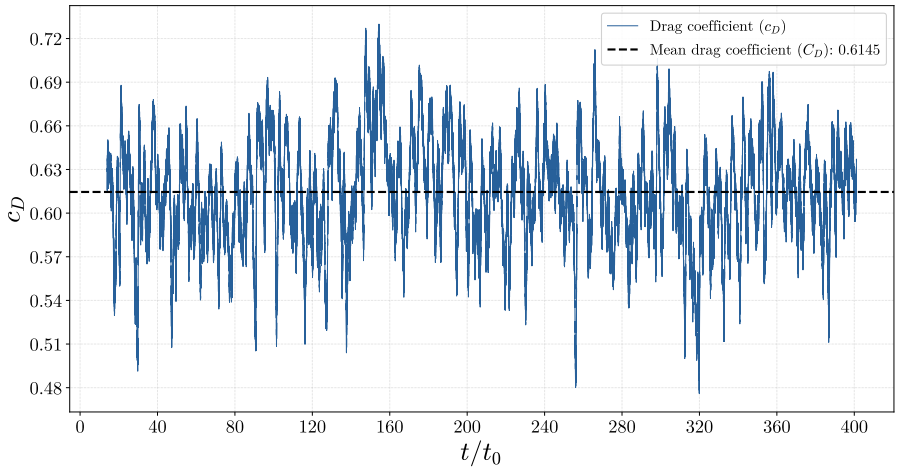
From this quantity, it is convenient to introduce a dimensionless parameter, namely the drag coefficient $c_{D,\mathrm{canopy}}$, which normalizes the aerodynamic force with respect to geometric dimensions and flow properties, thus enabling evaluations independent of the specific operating conditions. In particular, the instantaneous and time-averaged drag coefficients are defined as:

$$c_{D,\mathrm{canopy}} = \frac{F_{D,\mathrm{canopy}}}{\frac{1}{2}\rho_\infty U_\infty^2 S_{\mathrm{canopy}}} \quad \text{and} \quad C_{D,\mathrm{canopy}} = \frac{\overline{F}_{D,\mathrm{canopy}}}{\frac{1}{2}\rho_\infty U_\infty^2 S_{\mathrm{canopy}}} \tag{4.2}$$

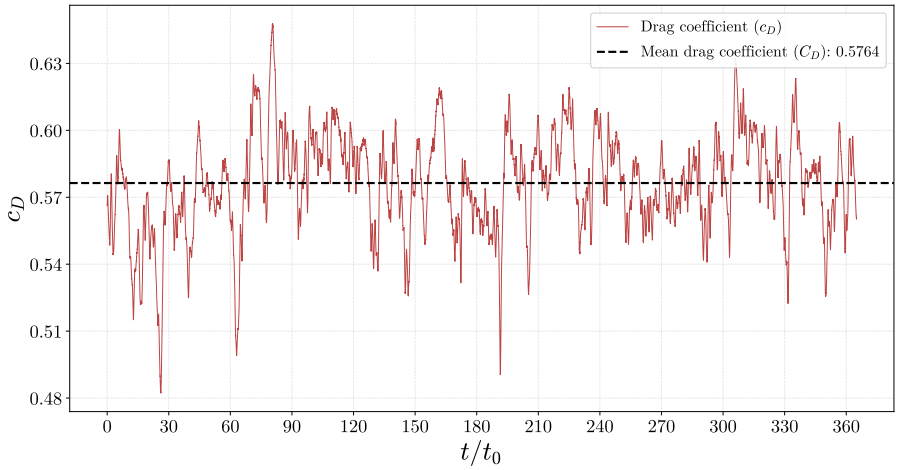
where S_{canopy} is the nominal surface area of the canopy normal to the flow direction, which can be calculated using the nominal diameter D as:

$$S_{\mathrm{canopy}} = \frac{\pi D^2}{4} \tag{4.3}$$

Figure 4.21 illustrates the time histories of the drag coefficients obtained from the dynamic RANS model and the LES benchmark, alongside their respective mean values $C_{D,\text{canopy}}$.



(a) RANS



(b) LES

Figure 4.21: Time history of the instantaneous drag coefficient of the canopy ($c_{D,\text{canopy}}$) along with its time-averaged value ($C_{D,\text{canopy}}$), computed from dynamic RANS (top) and LES (bottom) simulations.

To evaluate the aerodynamic performance in detail, it is useful to define a set of key statistical parameters, which are summarized in Table 4.1. As observed, the dynamic RANS model predicts a mean drag coefficient ($C_{D,\text{canopy}}$) very close to the benchmark value, exhibiting a relative error of only +6.62%. Regarding the root-mean-square of the fluctuations value ($c'_{D,\text{rms}}$), which quantifies the standard deviation of the drag force oscillations on the canopy, the model displays a relative error of +61.35%. It is important to emphasize that this percentage overestimation is largely magnified by the small magnitude of the reference fluctuation. Indeed, the absolute error is only 0.0136, which is remarkably contained, especially considering that conventional RANS approaches are inherently unable to capture such fluctuating parameters accurately. Another noteworthy result concerns the peak drag coefficient ($c_{D,\text{max}}$), which represents the maximum instantaneous drag value recorded during the simulation. This parameter is slightly overestimated by

the dynamic RANS model with a relative error of only +12.68%. Finally, for the peak factor (K_p), defined as the ratio of maximum to mean drag used to quantify load impulsiveness, the dynamic RANS model overestimates the benchmark by merely +5.68%. In conclusion, all key parameters demonstrate strong agreement between the two simulations, confirming that the dynamic RANS model effectively reproduces the LES benchmark with low error, even for unsteady quantities.

Parameter	Dynamic RANS	LES (Benchmark)	Δ (Abs. Error)	$e_{\%}$ (Rel. Error)
C_D	0.6145	0.5764	0.0382	+6.62%
$c'_{D,\mathrm{rms}}$	0.0359	0.0222	0.0136	+61.35%
$c_{D,\max}$	0.7299	0.6478	0.0822	+12.68%
K_p	1.1878	1.1239	0.0639	+5.68%

Table 4.1: Comparison of the canopy drag coefficient aerodynamic parameters between the dynamic RANS model and the LES benchmark.

4.2.2 Transverse Coefficient

The remaining components of the $\mathbf{F}_{\mathrm{canopy}}$ vector to be evaluated are $F_{y,\mathrm{canopy}}$ and $F_{z,\mathrm{canopy}}$. Considering that a parachute is analyzed, it is of no physical relevance to define a lift force and calculate its corresponding coefficient, but rather it is preferable to evaluate the transverse canopy force $F_{T,\mathrm{canopy}}$, defined as:

$$F_{T,\mathrm{canopy}} = \sqrt{F_{y,\mathrm{canopy}}^2 + F_{z,\mathrm{canopy}}^2} \tag{4.4}$$

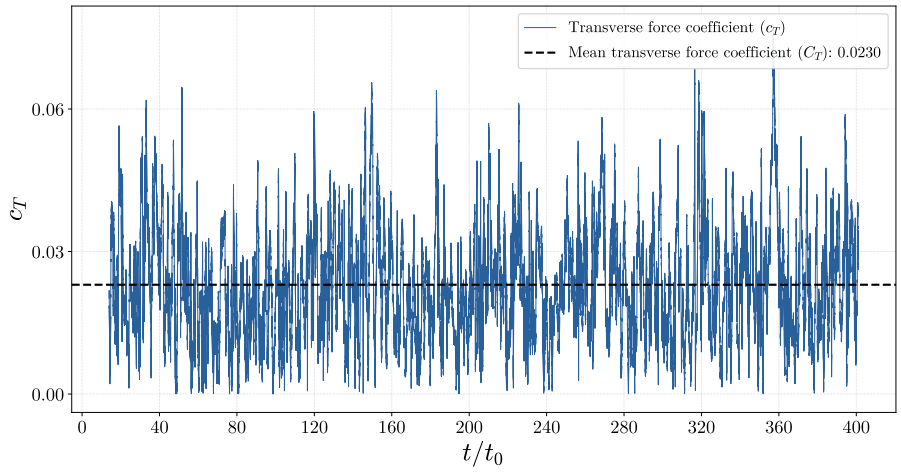
Analogously to the drag force F_D, it is possible to introduce a non-dimensional instantaneous transverse coefficient $c_{T,\mathrm{canopy}}$ and its mean value $C_{T,\mathrm{canopy}}$ as:

$$c_{T,\mathrm{canopy}} = \frac{F_{T,\mathrm{canopy}}}{\frac{1}{2}\rho_\infty U_\infty^2 S_{\mathrm{canopy}}} \quad \text{and} \quad C_{T,\mathrm{canopy}} = \frac{\overline{F}_{T,\mathrm{canopy}}}{\frac{1}{2}\rho_\infty U_\infty^2 S_{\mathrm{canopy}}} \tag{4.5}$$

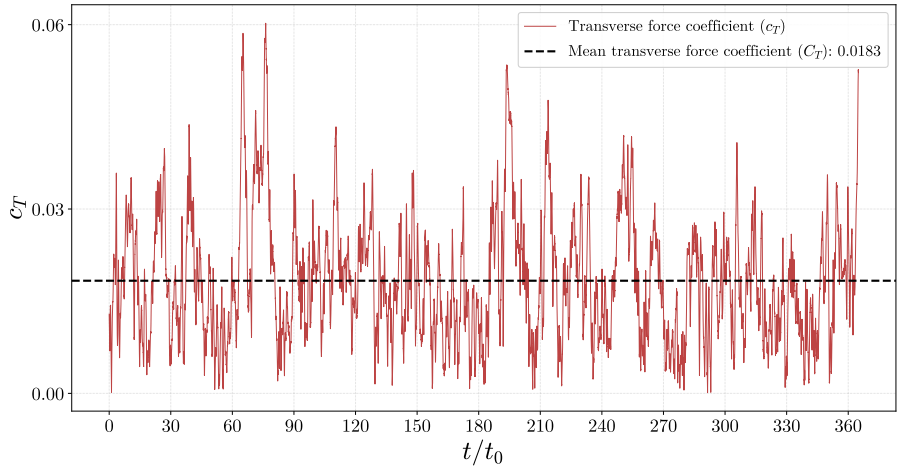
Figure 4.22 illustrates the time history of the transverse force coefficient $c_{T,\mathrm{canopy}}$, along with its corresponding mean values, for both the dynamic RANS and LES simulations.

Following the analysis carried out for the drag coefficient, a quantitative assessment yields a more informative interpretation of the results. Table 4.2 summarizes the statistical metrics, where it can be immediately noted that the magnitude of these parameters is significantly lower than the one seen for the drag coefficient; nevertheless, examining these metrics provides valuable insights into how the lateral force components are captured, subsequently allowing to obtain informations on the overall physics. In particular, for the mean transverse force coefficient ($C_{T,\mathrm{canopy}}$), the absolute error (Δ) remains extremely small at 0.0047. Although the relative error appears higher than that observed for the drag coefficient (+25.50%), it is important to consider that the reference values are of very limited magnitude, meaning that minor absolute variations translate into disproportionately high percentages. The same behavior is observed for the root-mean-square of the fluctuations ($c'_{T,\mathrm{rms}}$), with a low absolute error of 0.0020 and a relative error of +19.47%, as well as for the maximum coefficient ($c_{T,\max}$), which exhibits an absolute error of 0.0175 and a relative error of +29.13%.

This interpretation is further supported by analyzing the peak factor (K_p), which represents the largest non-dimensional parameter in the table and demonstrates a remarkably low relative error of +2.89%. Nevertheless, since the longitudinal force component F_x,



(a) RANS



(b) LES

Figure 4.22: Time history of the instantaneous transverse coefficient of the canopy ($c_{T,\text{canopy}}$) along with its time-averaged value ($C_{T,\text{canopy}}$), computed from dynamic RANS (top) and LES (bottom) simulations.

associated with drag, remains the primary contributor to the overall aerodynamic force vector, a higher relative uncertainty in the smaller transverse components is considered acceptable.

Parameter	Dynamic RANS	LES (Benchmark)	Δ (Abs. Error)	$e_{\%}$ (Rel. Error)
C_T	0.0230	0.0183	0.0047	+25.50%
$c'_{T,\mathrm{rms}}$	0.0120	0.0100	0.0020	+19.47%
$c_{T,\max}$	0.0778	0.0602	0.0175	+29.13%
K_p	3.3812	3.2862	0.0950	+2.89%

Table 4.2: Comparison of the canopy transverse force coefficient aerodynamic parameters between the dynamic RANS model and the LES benchmark.

4.2.3 Skin Friction Coefficient

Another parameter of interest for understanding the aerodynamic behavior around the bodies is the skin friction coefficient c_f. Specifically, the magnitude of its mean value, denoted as $|C_f|$, is calculated by non-dimensionalizing the mean wall shear stress magnitude $|\bar{\tau}_w|$ as:

$$|C_f| = \frac{|\bar{\tau}_w|}{\frac{1}{2}\rho_\infty U_\infty^2} \tag{4.6}$$

In the present study, this coefficient is not primarily of interest from a quantitative point of view, unlike the other parameters. This is because, as previously described, the flow on the canopy remains attached over only a very small region of its surface, and the capsule is not the main focus of the simulation. Nevertheless, it is included in this section to provide a comprehensive understanding of the system's aerodynamics from a different perspective.

In particular, the spatial distribution of the C_f magnitude on the capsule is shown in Figure 4.23. Presenting this trend exclusively for the capsule is especially informative because, as previously noted, its geometry experiences complex flow separation and reattachment. As can be observed, $|C_f|$ starts at zero at the stagnation point and reaches its peak at the location of maximum velocity, near the shoulder of the capsule nose. Moving downstream, the flow decelerates, causing $|C_f|$ to drop close to zero before rising again along the straight section. The coefficient then falls to zero at the first recirculation bubble, increases briefly during local reattachment along the rounded contour, and finally drops back to zero at the final separation point.

Looking instead at the 3D visualization of the mean skin friction coefficient C_f on the canopy in Figure 4.24, it confirms what was noted in the previous sections: the flow is largely detached almost everywhere. The only areas where the flow remains briefly attached are the skirt and the corner where the cavity meets the vent, with non-zero values.

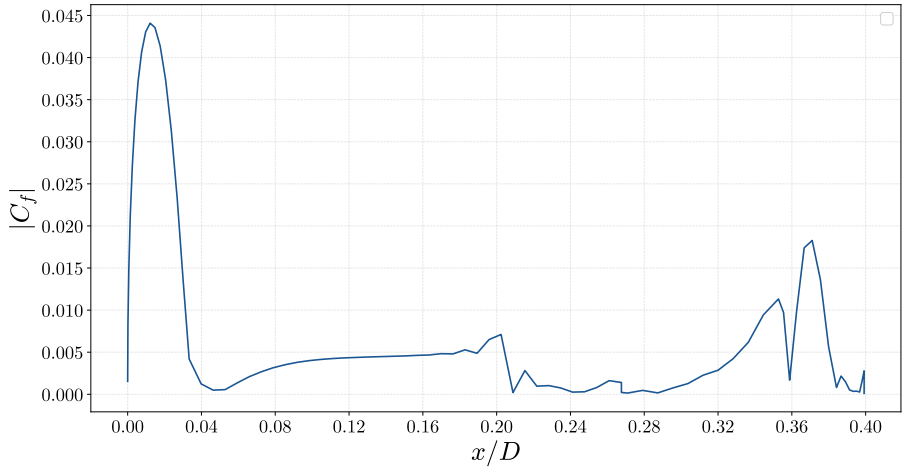


Figure 4.23: Mean skin friction coefficient magnitude ($|C_f|$) profile around the capsule in the x-r plane at $\theta = 0°$.

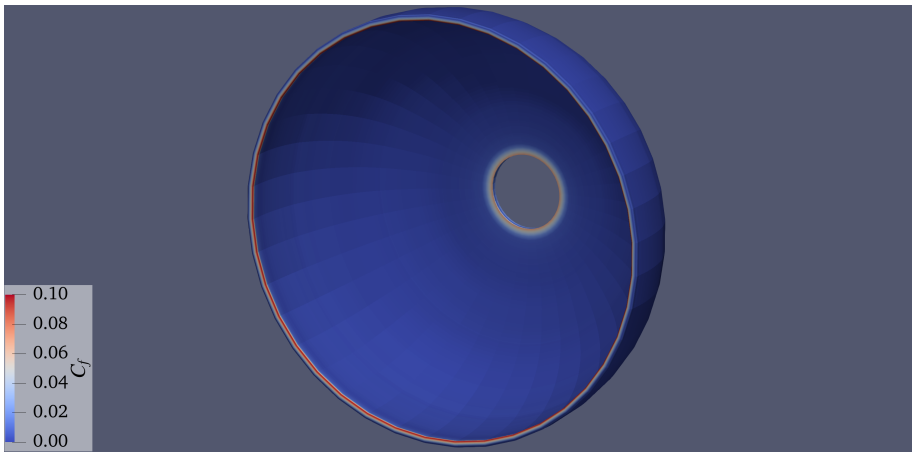


Figure 4.24: Three-dimensional distribution of the mean skin friction coefficient magnitude (C_f) on the canopy surface.

4.3 Canopy Aerodynamics and Frequency Spectrum Analysis

Based on the preceding discussion, a detailed analysis of the aerodynamics around the canopy can now be performed. Figure 4.25 displays the LIC visualization of the mean normalized velocity field around the canopy. The flow field is characterized by the presence of three main toroidal vortices: one located within the canopy cavity, one developing around the vent jet, and the largest one formed in the canopy wake. The cavity vortex clearly illustrates the recirculation bubble confined to this region, which retains the fluid while allowing a small portion to escape through the canopy skirt and the vent. The high C_p value in this area is caused by the violent impingement of the incoming flow against the canopy cavity, which abruptly decelerates the fluid and converts its dynamic pressure into stagnation pressure. Due to the pressure gradient between the ambient flow upstream ($C_p \approx 0$) and the high C_p at the inner wall, the fluid recirculates, creating a vortex that traps this high-pressure air inside the cavity and sustains these elevated pressure levels. The wake vortex, on the other hand, originates from the flow separation at the canopy skirt. Here, the fluid detaches immediately, creating a flow field characterized by a strong shear layer between the high-velocity outer flow and the recirculating low-energy fluid in the base region. In addition, as detailed in Section 4.1.2, a low-pressure base region develops behind the canopy, as the structure obstructs the oncoming stream and prevents a direct flow pass-through. This low-pressure core drives the formation of the large toroidal vortex that recirculates in the negative C_p region. Finally, the jet formed at the vent is driven by the large pressure differential across the canopy shell, which forces part of the internal fluid trapped in the cavity region outward. This high-velocity flow interacts immediately with the low-velocity fluid in the near wake, creating an intense shear layer that accelerates the adjacent slow-moving fluid. As this fluid moves downstream, it eventually exits the driving core of the jet and encounters resistance from the surrounding ambient fluid. Lacking further momentum input, it decelerates, deflects, and rolls up into a localized recirculation vortex. It should be noted that while these vortices are depicted here in a time-averaged, static representation, they continuously evolve and deform in the instantaneous field, as illustrated previously in Figure 4.5.

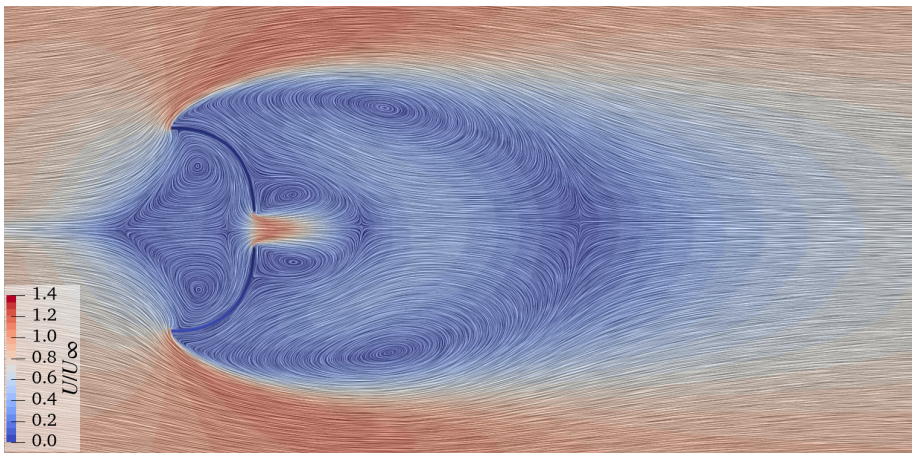


Figure 4.25: Mean normalized velocity magnitude (U/U_∞) field around the canopy visualized using LIC in the x-r plane at $\theta = 0°$.

To characterize the frequency content of the unsteady aerodynamic phenomena, a spectral analysis is performed by evaluating the Power Spectral Density (PSD) of the drag

coefficient signal (c_d) with respect to the non-dimensional Strouhal number, St, defined as:

$$St = \frac{fD}{U_\infty} \tag{4.7}$$

where f is the frequency.

The Power Spectral Density was computed using Welch's method with a Hanning window. To preserve the energy content under a logarithmic scale, the spectrum is presented in Figure 4.26 in pre-multiplied form ($St \cdot \mathrm{PSD}$) as a function of the Strouhal number (St). As can be seen, the cutoff occurs just past $St = 60$ for the LES dataset, whereas that of the dynamic RANS model extends further, terminating prior to $St = 2 \cdot 10^3$.

The plot exhibits two distinct behaviors, separated by a threshold at $St \approx 10$. Up to this value, the overall shape of the two spectra is very similar, although the dynamic RANS solution exhibits slightly higher energy values across various sub-ranges.

By contrast, in the range between $St \approx 10$ and the LES cutoff ($St = 60$), the LES spectrum decays smoothly, whereas the dynamic RANS solution exhibits minor oscillations. Furthermore, beyond $St = 60$, where the LES dataset ends, these fluctuations are amplified significantly in the dynamic RANS spectrum, forming a prominent wave before dropping off, thereby demonstrating an overproduction of energy at high frequencies.

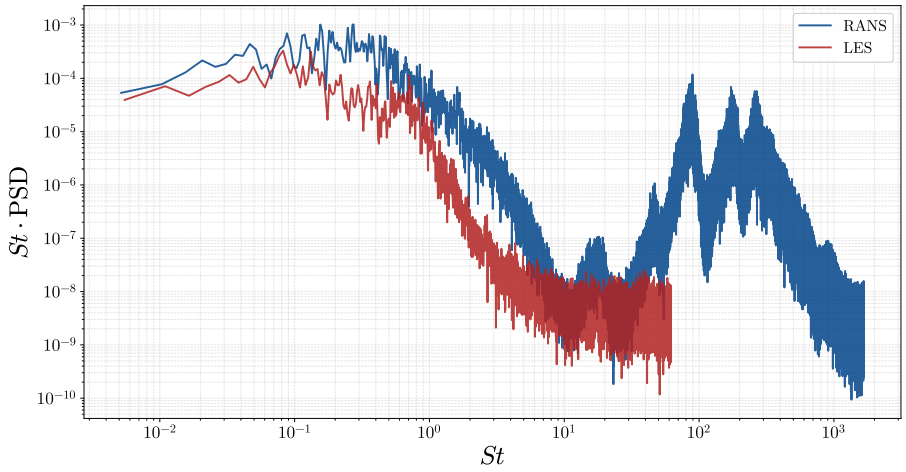


Figure 4.26: Comparison of the pre-multiplied power spectral densities ($St \cdot \mathrm{PSD}$) of the canopy drag coefficient ($c_{d,\mathrm{canopy}}$) as a function of the Strouhal number (St) in log-log scale between the dynamic RANS model and the LES benchmark.

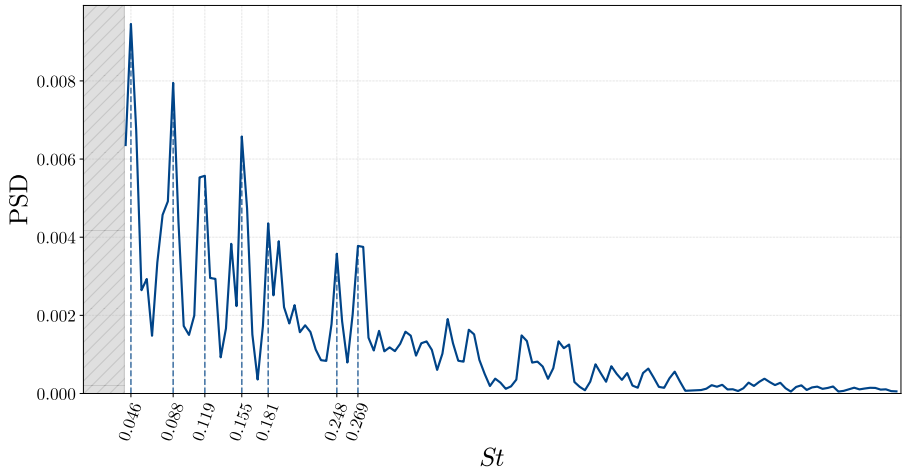
To gain physical insight into the dominant frequencies of the phenomenon, the PSD is plotted in Figure 4.27 with respect to the Strouhal number across a specific frequency band ($0.04 \leq St \leq 0.8$). Before proceeding with the analysis, it is worth emphasizing that the two signals were sampled differently, with the dynamic RANS dataset comprising a larger number of samples and featuring a higher cut-off frequency. The lower limit, $St = 0.04$, was selected to exclude frequencies too low to be statistically resolved within the simulation time window; this threshold is indicated by the grey area on the left side of the plot. Conversely, the upper limit ($St = 0.8$) was chosen to focus the plot on the most relevant spectral peaks. The dynamic RANS solution exhibits seven peaks, located at $St = 0.046$, $St = 0.088$, $St = 0.119$, $St = 0.155$, $St = 0.181$, $St = 0.248$ and $St = 0.269$. In contrast, the LES solution displays only four peaks, at $St = 0.049$, $St = 0.082$, $St = 0.115$, and $St = 0.132$. The first three peaks show very close agreement between the two solutions and are hereafter denoted as St_1, St_2, and St_3, respectively. The fourth peak ($St = 0.155$

for dynamic RANS and $St = 0.132$ for LES), however, reveals a larger discrepancy between the two spectra, with the dynamic RANS value differing by approximately +17% relative to the LES benchmark. Beyond these, the dynamic RANS solution exhibits a split peak near $St = 0.181$, which has been labeled as a single one in the plot for visual clarity, followed by two closely spaced peaks at $St = 0.248$ and $St = 0.269$. The occurrence of these spectral features might suggest that the corresponding physical phenomena are not centered around single fixed frequencies, but rather undergo mode switching. Nevertheless, given their complete absence in the LES results, they are most likely modeling artifacts rather than physical features of the flow.

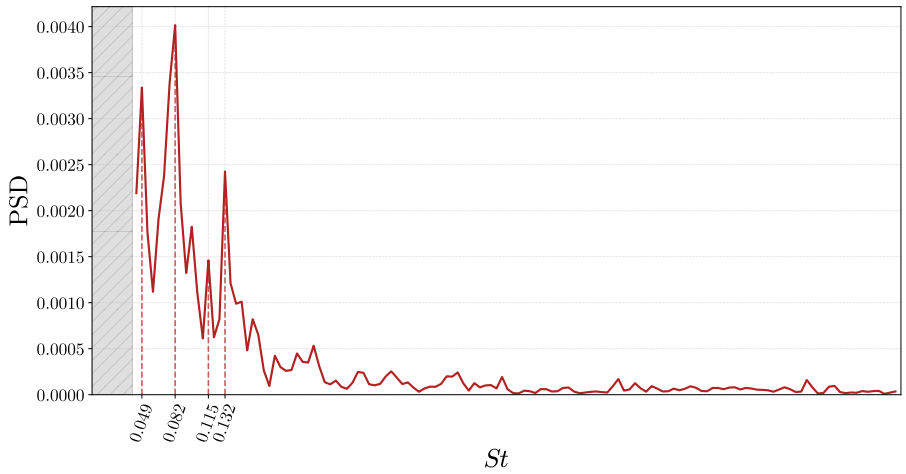
In conclusion, this analysis demonstrates that the dynamic RANS model accurately resolves the first three spectral peaks (St_1, St_2, St_3), capturing the physical wake phenomena that are described in more detail below. However, it exhibits marginally higher overall PSD values throughout the spectrum, confirming the trend previously noted in Figure 4.26. Furthermore, at higher frequencies, the model displays some limitations, mispredicting the position of the fourth peak at $St = 0.155$ and generating spurious spikes.

Focusing now on the three dominant spectral peaks identified earlier, the analysis begins with St_3, which corresponds to a fundamental and well-documented phenomenon in bluff body aerodynamics: vortex shedding. This mechanism is driven by the interaction between the high-velocity flow detaching from the canopy skirt and the low-velocity fluid within the recirculation bubble. As previously discussed, this velocity gradient generates a strong shear layer along the wake boundary, which triggers a Kelvin-Helmholtz instability. Consequently, the shear layer rolls up into coherent 3D structures called toroidal vortex rings, which grow progressively as they are convected downstream, entraining fluid from the surrounding region and expanding the wake footprint. It should be emphasized that the generation and behavior of these vortices are intrinsically coupled with the dynamics of the shear layer and, by extension, with the recirculation bubble, as detailed later in this section. Hence, this detachment process manifests at a characteristic shedding frequency corresponding to St_3. This phenomenon is clearly illustrated in Figure 4.28, which displays an instantaneous snapshot of the vorticity magnitude field. The upper threshold of the color scale has been adjusted to enhance the visual identification of the wake structures ($|\boldsymbol{\omega}| \in [0, 200]$ s^{-1}). Specifically, the figure highlights four primary vortices detaching from the canopy skirt, preceded by a continuous high-vorticity shear layer where small-scale vortex structures are not resolved due to the coarse local grid spacing.

A second phenomenon, strictly related to vortex shedding, is bubble pumping, associated with the first frequency St_1. This mechanism plays a fundamental role in the wake analysis and is characterized by a low-frequency, progressive deformation of the recirculation bubble behind the canopy. This behavior can be appreciated in Figure 4.29, where the low-velocity region of the wake expands considerably in the streamwise direction from Figure 4.29a to 4.29d, before collapsing downstream in Figure 4.29e to restart the cycle. Focusing on the vent jet provides further insight: the jet undergoes periodic elongation and contraction at the frequency of the pumping mode, coupled with vertical oscillations driven by wake turbulence. This generates strong temporal velocity fluctuations in both the streamwise (x) and radial (r) directions; these intense dynamics account for the discrepancies observed in the vent jet region for the radial components when compared against the LES benchmark in Section 4.1, as the mesh is likely not fine enough to fully capture them. Nevertheless, the qualitative flow evolution illustrated in the visual sequence, combined with the Strouhal number St_1 matching the LES value, demonstrates that the dynamic RANS model successfully resolves the core features of this complex physical phenomenon.



(a) RANS



(b) LES

Figure 4.27: Comparison of the power spectral densities (PSD) of the canopy drag coefficient ($c_{d,\text{canopy}}$) as a function of the Strouhal number (St) between the dynamic RANS model (top) and the LES benchmark (bottom).

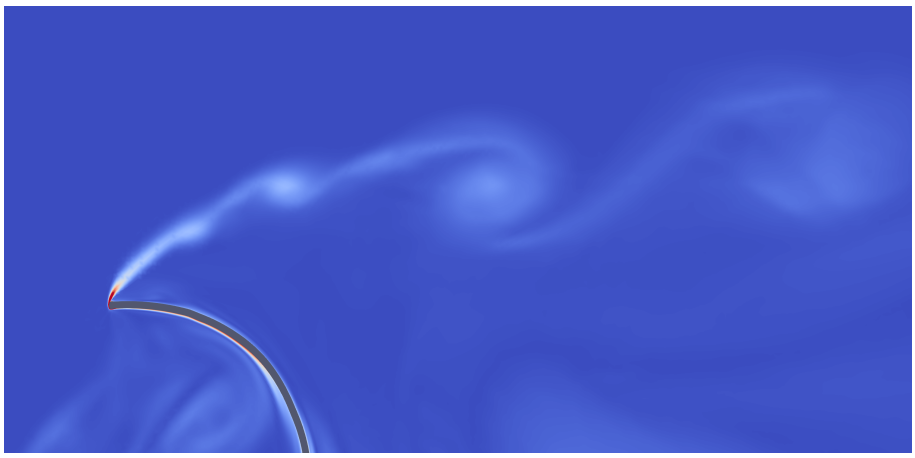
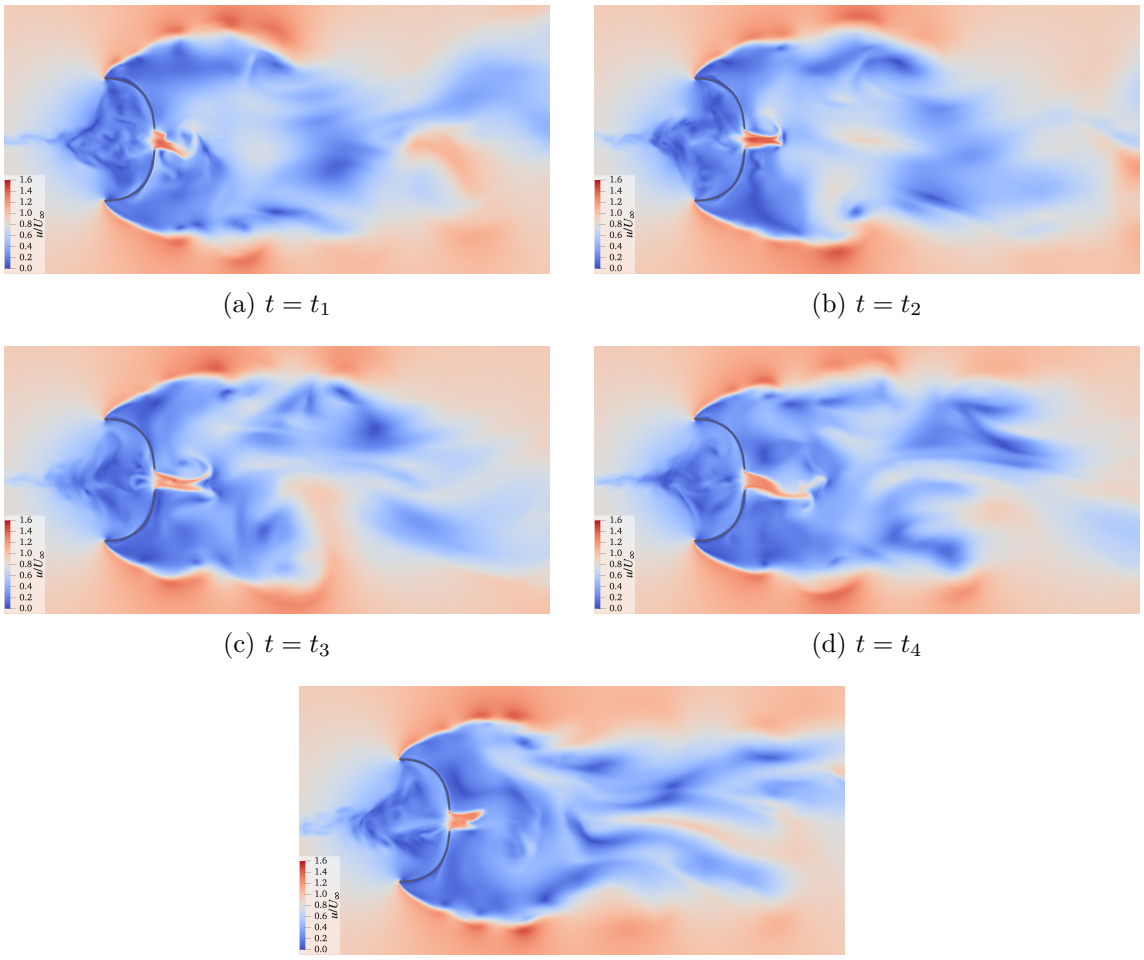


Figure 4.28: Instantaneous vorticity magnitude ($|\boldsymbol{\omega}| \in [0, 200]$ s^{-1}) field around the canopy in the x-r plane at $\theta = 0°$, highlighting vortex detachment at the skirt.



(a) $t = t_1$

(b) $t = t_2$

(c) $t = t_3$

(d) $t = t_4$

(e) $t = t_5$

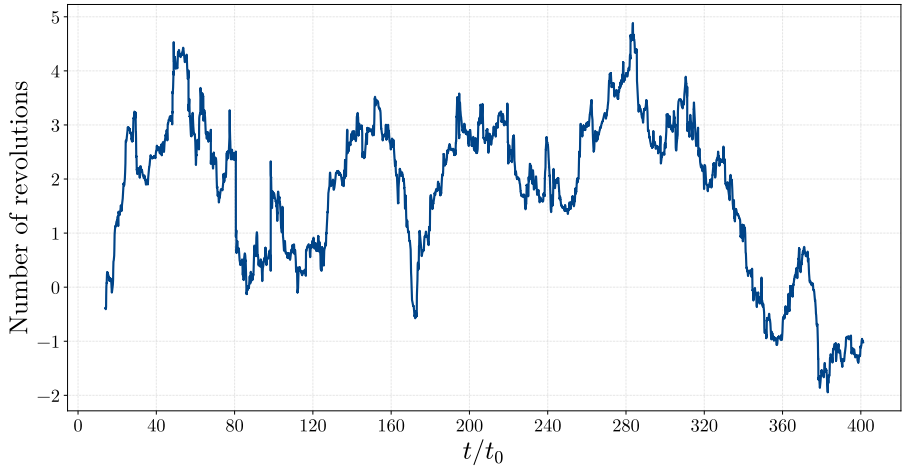
Figure 4.29: Instantaneous normalized velocity magnitude (u/U_∞) field around the canopy in the x-r plane at $\theta = 0°$ across five consecutive time instances, illustrating the bubble pumping dynamics.

This mechanism is orchestrated by a complex dynamic interaction between the vortex shedding and the near-wake recirculation bubble. Specifically, as previously introduced, the vortices generated by the flow separation at the canopy skirt enhance the entrainment of fluid into the recirculation zone. This process continuously traps fluid within the near wake, causing the recirculation bubble to expand and thereby enlarging the low-pressure region behind the canopy. However, this growth cannot proceed indefinitely: upon reaching a critical volume, the recirculation bubble becomes unstable and expels a significant portion of the accumulated mass downstream. The wake structure then returns to its initial configuration, allowing the cycle to repeat. This sudden mass discharge also propels downstream the coherent structures previously generated by the vortex shedding, where they are eventually dissipated and replaced by new structures in the subsequent cycle.

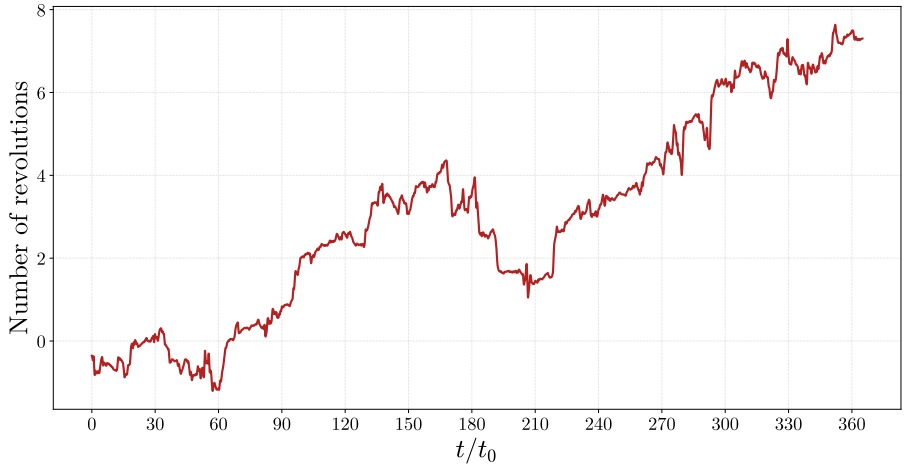
Another interesting aspect concerns the relationship between the first two characteristic frequencies. Specifically, the dynamic RANS model yields $\mathrm{St}_{1,\mathrm{RANS}} = 0.046$ and $\mathrm{St}_{2,\mathrm{RANS}} = 0.088$, whereas the LES benchmark produces $\mathrm{St}_{1,\mathrm{LES}} = 0.049$ and $\mathrm{St}_{2,\mathrm{LES}} = 0.082$. In both numerical approaches, the secondary frequency is nearly double the primary pumping mode, yielding a ratio of 1.91 for the dynamic RANS formulation and 1.67 for the LES counterpart. Consequently, this second frequency could represent the second harmonic associated with the bubble pumping dynamics.

A final fluid-dynamic phenomenon worth analyzing, which is not captured by the frequency study of the drag spectrum, is the helical motion of the wake. Specifically, in axisymmetric bodies like parachutes, the wake is not stationary in the azimuthal direction, but rotates with a certain frequency. This rotation can be visualized by analyzing how the angle θ of the transverse force coefficient vector varies over time. To properly track this motion, the phase angle was calculated as $\theta(t) = \arctan(c_z(t)/c_y(t))$. Accordingly, the plot of $\theta(t)$ over time in Figure 4.30 is presented in an unwrapped configuration, so that successive revolutions are represented continuously without creating discontinuities at the 2π–0 transitions. In addition, the θ data have been filtered using a Savitzky-Golay algorithm with a second-order local polynomial and a smoothing window of 101 points to remove high-frequency oscillations and display a clearer trend, showing the cumulative number of revolutions over time. The physically expected behavior is captured by the LES benchmark in Figure 4.30b, where the profile exhibits a quasi-linear increase, indicating that the wake structure rotates persistently in the same direction. In contrast, the dynamic RANS solution, shown in Figure 4.30a, does not display a continuous increase; instead, it completes approximately 4.5 revolutions in one direction, only to reverse and return toward the initial state, repeating this process with minor variations. This behavior is noteworthy because it demonstrates that the vortex structure behind the canopy is not actually rotating steadily, but reverses its direction of rotation after a few revolutions. The exact cause of this anomaly is difficult to attribute with certainty. If it were solely due to azimuthal resolution, a slight oscillation of a few degrees without completing a full cycle would be expected, rather than a direction reversal after several complete revolutions. The primary cause is likely related to a synergistic interplay between the coarse azimuthal mesh resolution and the dynamic RANS model, which fails to resolve the small turbulent scales around the canopy skirt and overestimates their energy, thereby hindering the helical motion. More precisely, the underlying mechanism behind this behavior could be caused by the high-frequency oscillations observed for the dynamic RANS model in Figure 4.26 after $St \approx 60$, which could prevent the correct physical representation.

Finally, Figure 4.31 shows the Q-criterion isosurfaces ($Q = 15\ \mathrm{s}^{-2}$), colored by the instantaneous velocity magnitude field. As can be appreciated, the model is capable of resolving a wide range of turbulent scales associated with the phenomenon, from the



(a) RANS



(b) LES

Figure 4.30: Comparison of the unwrapped θ profiles in number of revolutions versus normalized time between the dynamic RANS (top) and the LES benchmark (bottom).

smallest ones in the capsule wake and canopy cavity to the larger coherent structures in the main canopy wake. Additionally, the previously discussed toroidal vortices are visible at the canopy skirt before being advected downstream by the bubble pumping mechanism.

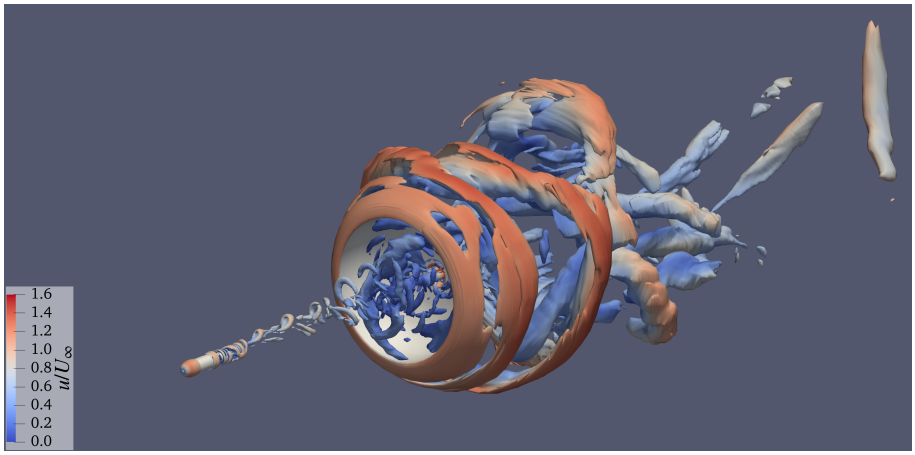


Figure 4.31: Instantaneous vortex structures identified by Q-criterion isosurfaces ($Q = 15\ \mathrm{s}^{-2}$), colored by the instantaneous velocity magnitude field.

4.4 Turbulence Model Variables

This section evaluates the modeled turbulence quantities to assess how they are computed by the numerical scheme across the flow field. The analysis focuses specifically on the canopy subdomains, as the turbulence levels near the capsule remain negligible.

4.4.1 Turbulent Kinetic Energy

As introduced in Chapter 2, the dynamic RANS model employed in the simulations is based on the k–ω turbulence formulation. Consequently, a key variable of interest is the turbulent kinetic energy (k) around the canopy, which provides crucial insights into regions of elevated turbulence production. The production term of k was previously defined in Equation (2.36) as:

$$P_k = 2\nu_\tau \langle S_{ij} \rangle_\tau \langle S_{ij} \rangle_\tau = \frac{1}{2}\nu_\tau \left(\frac{\partial \langle U_i \rangle_\tau}{\partial x_j} + \frac{\partial \langle U_j \rangle_\tau}{\partial x_i} \right) \left(\frac{\partial \langle U_i \rangle_\tau}{\partial x_j} + \frac{\partial \langle U_j \rangle_\tau}{\partial x_i} \right) \tag{4.8}$$

According to the governing equations, the production of turbulent kinetic energy scales directly with the product of the eddy viscosity ν_t and the mean velocity gradients. Higher levels of turbulence production are therefore expected in regions characterized by intense shear. This behavior is illustrated in Figure 4.32, which presents the instantaneous distribution of the turbulent kinetic energy k around the canopy. The peak values of k are strictly localized along the shear layers detaching from the canopy skirt and those surrounding the vent jet. Furthermore, while the entire recirculating wake region maintains non-zero values of k, the field drops to negligible levels inside the stagnant canopy cavity.

Given the highly unsteady nature of the flow, the spatial distribution of instantaneous turbulent kinetic energy fluctuates dynamically. To characterize the overall behavior, it

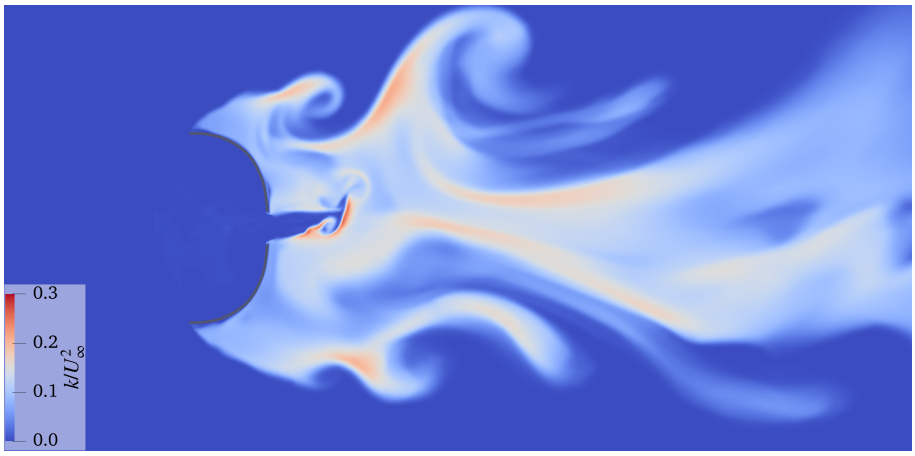


Figure 4.32: Instantaneous normalized turbulent kinetic energy (k/U_∞^2) field around the canopy in the x-r plane at $\theta = 0°$.

is more insightful to examine the averaged field K, shown in Figure 4.33. Due to the continuous oscillation of the shear layer position, an extensive region downstream of the vent jet exhibits high mean values of $K \approx 0.09$. Nevertheless, peak values remain localized along the boundaries of the near wake, where vortex shedding originates, and immediately downstream of the vent exit, where the high-velocity jet interacts with the low-velocity recirculation bubble to generate steep velocity gradients.

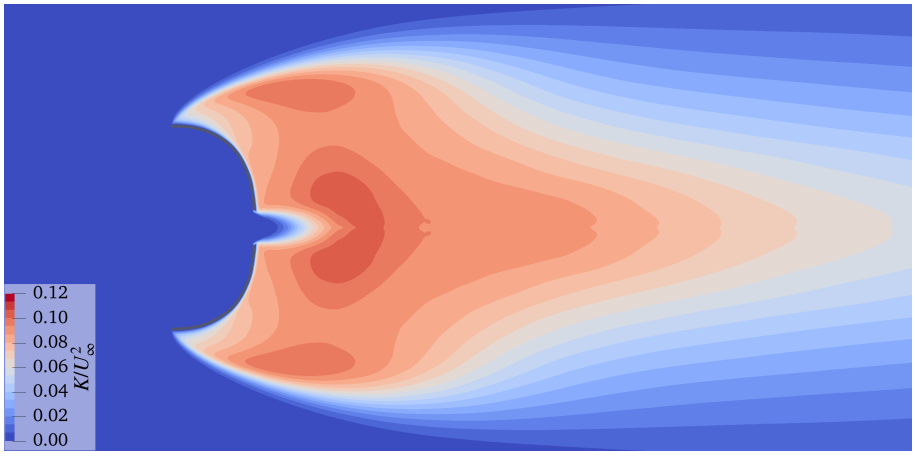


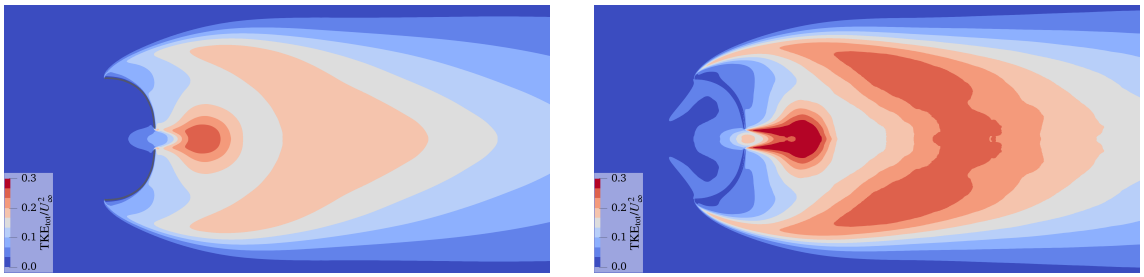
Figure 4.33: Mean normalized turbulent kinetic energy (K/U_∞^2) field around the canopy in the x-r plane at $\theta = 0°$.

By looking at the kinetic energy field alone, it is difficult to evaluate how well dynamic RANS models the unresolved part of the flow. To assess this properly through a comparison with LES results, it is preferable to use the mean total turbulent kinetic energy $\mathrm{TKE_{tot}}$, which is defined as the sum of the mean modeled turbulent kinetic energy K and the resolved component derived from the trace of the Reynolds stress tensor. For the dynamic RANS model, it is calculated as:

$$\mathrm{TKE_{tot}} = K + \frac{1}{2}\left(\langle u_x' \rangle_\tau^2 + \langle u_r' \rangle_\tau^2 + \langle u_\theta' \rangle_\tau^2\right) \tag{4.9}$$

Figure 4.34 shows the distribution of $\mathrm{TKE_{tot}}$. Overall, the dynamic RANS model effectively captures the primary regions of the mean total turbulent kinetic energy pro-

duction. However, the values of TKE_{tot} are noticeably underestimated relative to the LES benchmark both inside the canopy cavity and along the rear section of the recirculation bubble. The most pronounced discrepancies appear in the high-TKE_{tot} region upstream of the vent jet, where LES predicts higher peak values, and within the initial shear layers detaching from the canopy skirt and vent exit. Specifically along these detaching shear layers, the dynamic RANS model exhibits excessive dissipation, creating a localized deficit or "hole" in TKE_{tot} prior to downstream wake development. These differences stem directly from the interplay between grid resolution and modeled turbulence. Near the skirt, where the coarse mesh limits the direct resolution of initial shear-layer instabilities, the dynamic formulation fails to sufficiently elevate eddy viscosity. Consequently, the modeled contribution cannot compensate for the deficit in resolved fluctuations, resulting in a localized drop in mean total turbulent kinetic energy that persists until downstream turbulence fully develops.



(a) RANS: Mean total turbulent kinetic energy (TKE_{tot}/U_∞^2)

(b) LES: Mean total turbulent kinetic energy (TKE_{tot}/U_∞^2)

Figure 4.34: Comparison of the mean normalized total turbulent kinetic energy (TKE_{tot}/U_∞^2) fields around the canopy between dynamic RANS (left) and LES (right) in the x-r plane at $\theta = 0°$.

Figure 4.35 presents a quantitative comparison of TKE_{tot} profiles extracted at the axial stations previously analyzed. These curves reveal more pronounced discrepancies than the mean velocity fields, directly confirming the spatial trends identified in the 2D contours. Although the dynamic RANS model reproduces the overall profile topology, it systematically underestimates TKE_{tot} relative to LES across almost all locations. At $x/D = 1.20$ inside the canopy cavity, as well as at $x/D = 2.25$, the model yields lower values. At $x/D = 2.00$, in the high-energy region past the vent exit, it dampens the central peak at $r/D \approx 0$, overestimates energy across the mid-radial region, and falls below LES toward the outer wake boundaries, mirroring the pattern observed for velocity fluctuations. The largest discrepancy occurs at $x/D = 2.50$, where the underestimation is most pronounced, resulting in a marked offset across the wake width.

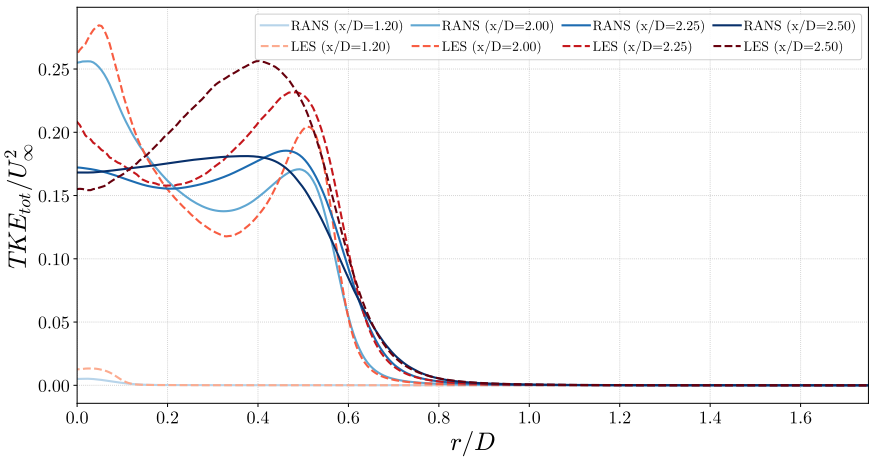


Figure 4.35: Comparison of the mean normalized total turbulent kinetic energy ($\mathrm{TKE_{tot}}/U_\infty^2$) profiles between the dynamic RANS and the LES models along the radial coordinate r/D at $x/D = 1.20, 2.00, 2.25$, and 2.50.

4.4.2 Dynamic Coefficient and Eddy Viscosity

Another key quantity for the dynamic RANS model is the dynamic coefficient c_μ, which is evaluated dynamically as detailed in Section 2.2. This coefficient determines the local turbulent viscosity throughout the domain, controlling how the eddy viscosity adjusts to local grid refinement. Figure 4.36 displays the instantaneous distribution of c_μ. The field exhibits strong spatial variations rather than a uniform value, adapting dynamically to local flow structures and mesh resolution. High values concentrate along the shear layer near the canopy skirt, inside the canopy cavity, and along the vent jet.

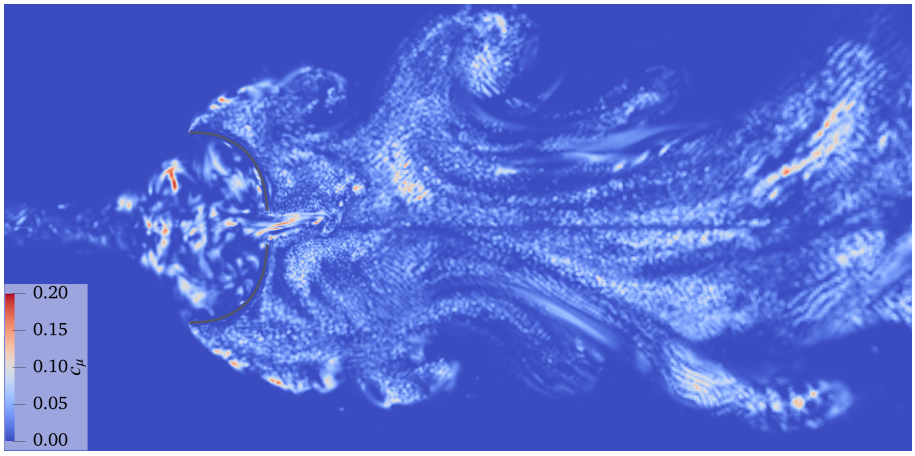


Figure 4.36: Istantaneous dynamic coefficient (c_μ) field around the canopy in the x-r plane at $\theta = 0°$.

To better understand the model behavior, it is useful to examine the spatial distribution of the mean dynamic coefficient C_μ, shown in Figure 4.37. As can be observed, the mean value remains below the standard constant benchmark of 0.09, varying predominantly between 0.02 and 0.06 across the domain as it dynamically adapts to the local grid resolution, with a localized peak of approximately 0.12 on the outer edge of the vent. Furthermore, the model correctly yields elevated values within the shear layer downstream

of the canopy skirt and in the early developing jet, where the local mesh resolution is too coarse to resolve the small-scale turbulent structures.

Additionally, the distribution reveals a localized numerical discontinuity in C_μ near the symmetry axis. This artifact may be primarily attributed to the mesh topology near the centerline, where structured hexahedral cells transition into smaller prismatic elements, introducing a local drop in mesh quality and structural continuity. As a result, the dynamic model predicts a sharp, intermittent reduction in C_μ along the axis, lowering its magnitude relative to adjacent elements.

Nevertheless, as shown in the preceding sections, this localized axial perturbation does not compromise the global flow solution. The limited effect of this C_μ drop is inherently tied to the dynamic model formulation: since the axial prismatic elements are smaller than the surrounding hexahedra, the reduction in modeled eddy viscosity is partially offset by an increase in resolved velocity fluctuations, thereby mitigating the local numerical artifact. Consequently, this minor axial discontinuity was accepted as a favorable trade-off to preserve high grid quality throughout the remainder of the domain.

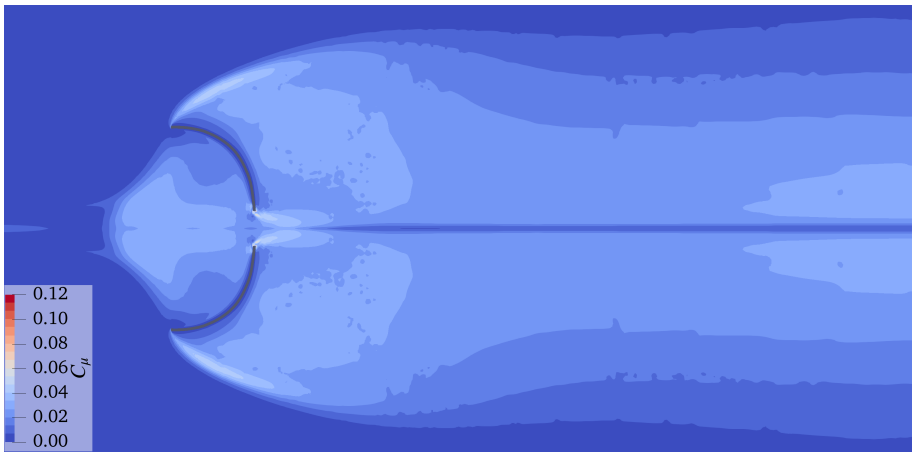


Figure 4.37: Mean dynamic coefficient (C_μ) field around the canopy in the x-r plane at $\theta = 0°$.

These characteristics directly translate into the mean eddy viscosity field (ν_t), shown in Figure 4.37. Specifically, the artifact along the symmetry axis remains evident, and the overall spatial distribution of ν_t mirrors the trends observed for C_μ, with elevated values consistently concentrated within the shear layer.

Additionally, a distinct drop in $\bar{\nu}_t$ appears in the canopy skirt shear layer immediately downstream of separation, consistent with the deficits previously observed in both the velocity fluctuation and $\mathrm{TKE}_{\mathrm{tot}}$ fields. This reflects a local underprediction of eddy viscosity, which fails to reach sufficiently high values to compensate for the unresolved turbulent scales in this region.

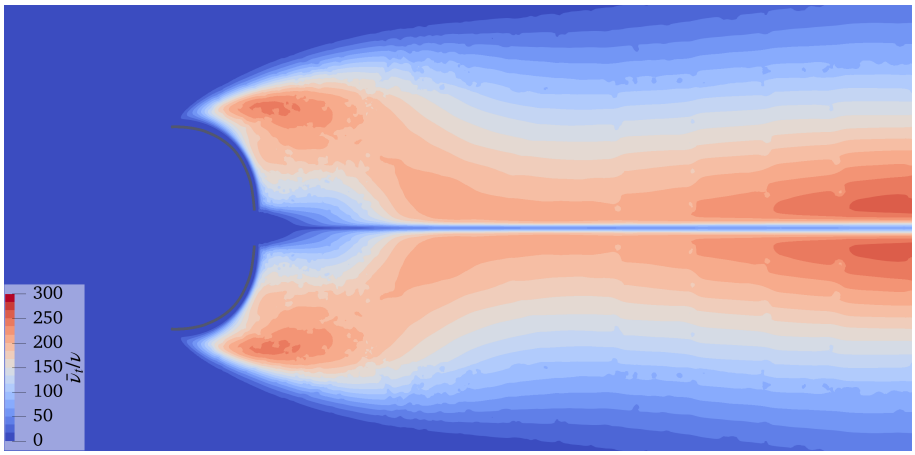


Figure 4.38: Mean eddy viscosity ($\bar{\nu}_t/\nu$) field around the canopy in the x-r plane at $\theta = 0°$.

Chapter 5

Conclusions

The simulation results are highly encouraging. As outlined in preceding chapters, the dynamic RANS model provides a computationally efficient framework for capturing complex bluff body aerodynamics, such as those characteristic of parachute systems, by resolving dominant coherent structures without demanding the significantly higher mesh resolution required by LES. Despite these substantial grid differences, the dynamic RANS formulation successfully predicted the primary aerodynamic quantities and physical mechanisms, yielding close agreement with the LES benchmark.

In particular, the model captured first-order statistics with high accuracy, yielding strong correspondence for both mean axial velocity and pressure coefficient distributions relative to the LES benchmark. Although the radial velocity component exhibited a larger discrepancy near the vent jet region, the overall prediction remained highly reliable.

Regarding second-order statistics, such as velocity fluctuations ($u'_{x,\mathrm{rms}}$, $u'_{r,\mathrm{rms}}$, and $u'_{\theta,\mathrm{rms}}$), discrepancies compared to the LES benchmark are more pronounced, exhibiting localized regions of modest under- and overprediction. Nevertheless, these differences remain well within acceptable limits, given that dynamic RANS operates on a significantly coarser mesh that cannot resolve the full turbulent spectrum. Indeed, the model captures fluctuation distributions that conventional RANS formulations fail to predict altogether. Furthermore, because second-order quantities are rarely the primary governing metrics for macroscopic aerodynamic loads or structural sizing, these minor inaccuracies do not impair the practical validity of the results. Total turbulent kinetic energy demonstrates a similar level of agreement, with noticeable offsets confined primarily to $x/D = 2.50$, near the closure of the recirculation bubble.

Focusing on the aerodynamic forces, the simulation predicted the primary metric, namely the mean drag coefficient (C_D), with a relative error of +6.62% compared to the LES benchmark. The temporal evolution and statistical behavior of both c_D and c_T exhibited strong agreement with the reference data, demonstrating the model's capability to resolve the governing aerodynamic loads. Predicting C_D with high fidelity is a critical requirement, as canopy drag is tightly coupled to the complex unsteady flow dynamics in the wake. Achieving this level of agreement at a fraction of the computational cost required by LES highlights the strong engineering utility of the dynamic RANS approach.

Ultimately, the simulation captured all dominant unsteady mechanisms, namely the vortex shedding, the bubble pumping, and the helicoidal wake motion. For the helicoidal dynamics, the model exhibited intermittent reversals in rotational direction rather than continuous rotation, switching sense after several cycles. This behavior is primarily attributable to grid coarsening and does not impair the overall validity of the approach for primary aerodynamic sizing. Regarding the spectral response, the dynamic RANS solu-

tion accurately predicts the frequencies of the first three dominant peaks, but generally overestimates spectral amplitudes overall, with particularly pronounced oscillations for $St \gtrsim 60$. If an exact determination of peak magnitudes is required, further grid refinement is necessary.

In conclusion, the dynamic RANS model proved capable of resolving complex unsteady phenomena with a limited number of mesh cells, representing a promising outcome for future CFD applications. Traditionally, industrial aerodynamic studies required a strict trade-off between the fast but less accurate standard RANS models and the high fidelity of LES, which demands high computational resources. This dynamic approach offers an effective middle ground, allowing engineers to adapt mesh refinement simply to the required level of detail, while still obtaining results in close agreement with high-resolution benchmark simulations.

For future work, executing the same simulation on this mesh using a standard k-ω model would provide a direct benchmark against conventional RANS formulations. Additionally, evaluating a grid with finer azimuthal discretization represents a logical next step. Although azimuthal refinement was deliberately constrained in this study to limit overall cell count, increasing it in subsequent investigations would help elucidate the mechanisms governing the helicoidal vortex dynamics. Specifically, it would determine whether the observed rotational intermittency stems primarily from spatial filtering induced by grid coarseness or from the intrinsic formulation of the dynamic model itself.

Bibliography

[1] A. Cimarelli, N. Marras, B. Niceno, and Y. Tessier Urrecha. Unifying formalism and closures for coarse-grained approaches to turbulence, 2025.

[2] Luca Placco, Giulio Soldati, Matteo Bernardini, and Francesco Picano. On flight instabilities of capsule-rigid parachute system during supersonic planetary descent. *Aerospace Science and Technology*, 160:110026, 2025.

[3] Stephen B. Pope. *Turbulent Flows*. Cambridge University Press, Cambridge, 2000.

[4] Florian Ries. *Numerical Modeling and Prediction of Irreversibilities in Sub- and Supercritical Turbulent Near-Wall Flows*. PhD thesis, Technische Universität Darmstadt, 2018.

[5] Yves Tessier Urrecha, Giorgio Manzi, Filippo Cancellotti, and Andrea Cimarelli. Development of a class of dynamic RANS closures for coarse-grained approaches to turbulence, 2026. Preprint.

[6] L. Placco, C. Philippe, F. Panerai, F. Picano, and L. Villafañe. Three-dimensional flow dynamics behind a rigid parachute in subsonic regime. Preprint.

[7] Christophe Geuzaine and Jean-François Remacle. Gmsh: A 3-D finite element mesh generator with built-in pre- and post-processing facilities. *International Journal for Numerical Methods in Engineering*, 79:1309–1331, 2009.

[8] OpenFOAM Foundation. OpenFOAM-10 source code repository. `https://github.com/OpenFOAM/OpenFOAM-10`, 2022. Accessed: 2026.

[9] F. Moukalled, L. Mangani, and M. Darwish. *The Finite Volume Method in Computational Fluid Dynamics: An Advanced Introduction with OpenFOAM and MATLAB*. Springer, 2016.

[10] Christopher Greenshields and Henry Weller. *Notes on Computational Fluid Dynamics: General Principles*. CFD Direct Ltd, Reading, UK, 2022.

[11] OpenCFD Ltd. Openfoam documentation overview. `https://www.openfoam.com/documentation/overview`, 2026. Accessed: 2026.

,

Acknowledgments

I would like to express my sincere gratitude to my supervisor, Prof. Andrea Cimarelli, for giving me the opportunity to work on this research topic and for his continuous guidance and support throughout all phases of this work.

I am deeply grateful to Yves Tessier Urrecha, who directly supported me throughout the development of this thesis, providing valuable insights and guiding me through critical technical choices.

Finally, I would like to thank Luca Placco and the research group at the University of Padua for kindly sharing the geometric model and data used in this study, as well as for their helpful collaboration.